Diss. ETH No. 14265

Mean Value Modeling of a Pressure Wave Supercharger Including Exhaust Gas Recirculation Effects

A dissertation submitted to the
SWISS FEDERAL INSTITUTE OF TECHNOLOGY
ZÜRICH

for the degree of
Doctor of Technical Sciences

presented by
Felix Weber
Dipl. Masch.-Ing. ETH
born 13. January 1970
citizen of Zürich ZH

accepted on the recommendation of
Prof. Dr. L. Guzzella, examiner
Prof. Dr. M. K. Eberle, co-examiner

2001

Meinen Eltern gewidmet

Seite Leer /
Blank leaf

Preface

This thesis is based on the research performed at the Engine Systems Laboratory of the Swiss Federal Institute of Technology (ETH) in Zurich between 1996 and 2001. It was part of the PALOS (PArt-Load Optimized System) project which was financially supported by the Swiss Federal Office of Energy (BFE), Grant No. 15752.

First of all I would like to thank my supervisor Professor Dr. Lino Guzzella for having accepted my application five years ago, for the organization of the funding, and for continuous support during the course of this work as well as Professor Dr. Meinrad K. Eberle for accepting to be my co-examiner.

Sincere thanks are extended to Dr. Alois Amstutz, Dr. Chris Onder, and Dr. Hans U. Hörler for their helpful advice and valuable discussions.

I am also grateful to the people from the Engine Systems Laboratory and the Measurement and Control Laboratory for their help and to the team from Swissauto/Wenko AG, Burgdorf, for their technical support. Special thanks go to Brigitte Rohrbach for her proofreading of the text. Deep indebtedness is acknowledged to Peter Spring whose help to finish this work was invaluable.

However, my deepest thanks and greatest appreciation are reserved for my parents and my partner, Brigitte, as without their support it would never have been possible to realize this work.

Zurich, June 2001
Felix Weber

Seite Leer /
Blank leaf

Contents

Seite Leer /
Blank leaf

Abstract

Naturally aspirated spark ignition (SI) engines with three-way catalytic exhaust gas aftertreatment systems inherently have a poor efficiency at part-load conditions since engine torque then is controlled by changing intake manifold pressure which causes pumping losses for the spark ignition engine. One attempt at improving this drawback has been to downsize the engine and to recover the engine power by supercharging. The small supercharged SI engine operates more efficiently in the range between lower and middle loads compared to a naturally aspirated SI engine due to the smaller pumping losses.

The pressure wave supercharger represents one possibility of supercharging a downsized SI engine. Since the exhaust gases and the fresh air are in direct contact in this charger, undesirable exhaust gas recirculation through the charger is possible. Sudden high exhaust gas recirculation causes a breakdown of the engine torque. In order to guarantee good driveability, exhaust gas recirculation must be avoided. Therefore, the target of the presented work is to investigate, to model, and to explain the effects of exhaust gas recirculation within a pressure wave supercharger.

The work presents a mean value system model of an SI engine supercharged with a pressure wave supercharger with gas pocket valve. The system model is able to predict with good accuracy states such as pressures, temperatures, mass flows, engine torque, and exhaust gas recirculation through the charger in steady-state and transient operating conditions. It explains why the scavenging process of the pressure wave supercharger during a load step must deteriorate. Model extrapolation demonstrates that a faster closing velocity of the gas pocket valve causes a worse scavenging.

The most important part of the overall system model is the model of the pressure wave supercharger. It calculates a simplified pressure wave process based on the relations of the linear one-dimensional gas dynamics neglecting the fast dynamics of the pressure wave process. It is validated by the identification of four physically motivated model

parameters. As a result, the nonmeasurable leakage losses of the pressure wave supercharger, the nonmeasurable mixing zone length, and its profile between exhaust gases and fresh air can be determined. The validated model of the pressure wave supercharger shows an error on the order of 5%.

The developed mean value system model of a pressure wave supercharged SI engine is a simulation tool. The tool may be used for system analysis, system optimization, and model based controller design in the future.

Zusammenfassung

Otto-Saugmotoren mit Drei-Wege-Katalysator zeigen in der Teillast einen schlechten Wirkungsgrad als Folge der quantitativen Füllungsregelung. Diese wird über eine Absenkung des Einlassdruckes realisiert, was zu Gaswechselverlusten für den Motor führt. Ein möglicher Ansatz, wie das Teillastverhalten von Otto-Saugmotoren verbessert werden kann, ist die Aufladung des Motors bei gleichzeitiger Hubvolumenreduktion (Downsizing), um gleiche Motorleistung zu garantieren. Im Vergleich zu Saugmotoren arbeitet ein aufgeladener Ottomotor gleicher Leistung bei kleineren bis mittleren Lasten effizienter, da im Vergleich zu einem Otto-Saugmotor weniger Gaswechselarbeit geleistet werden muss.

Der Druckwellenlader stellt eine Möglichkeit für die Aufladung eines Verbrennungsmotors dar. Da in diesem Ladertyp die Rauchgase und die Frischluft in direktem Kontakt stehen, ist unerwünschte Abgasrezirkulation über den Lader möglich. Eine plötzliche starke Abgasrezirkulation führt zu einem Einbruch des Motordrehmoments. Will man gute Fahrbarkeit garantieren, muss Abgasrezirkulation vermieden werden. Das Ziel der vorliegenden Arbeit ist es deshalb, den Effekt der Abgasrezirkulation über den Druckwellenlader zu untersuchen, zu modellieren und zu erklären.

Die Arbeit präsentiert ein Motormodell eines mit einem Druckwellenlader mit Gastaschen-Ventil aufgeladenen Ottomotors. Das Modell sagt Zustandsvariablen wie Drücke, Temperaturen, Massenströme, Motordrehmoment und Abgasrezirkulation über den Lader mit guter Genauigkeit voraus, und zwar für stationären und instationären Motorbetrieb. Das Motormodell erklärt, weshalb die Spülung des Druckwellenladers während eines Lastsprunges schlechter werden muss. Die Modellextrapolation zeigt, dass ein schnelleres Schliessen des Gastaschen-Ventils zu einer Verschlechterung der Spülung führt.

Der zentrale Teil des gesamten Motormodells ist das Modell des Druckwellenladers. Basierend auf den Grundlagen der eindimensionalen, linearen Gasdynamik berechnet es einen vereinfachten Druck-

wellenprozess, wobei die sehr schnelle Dynamik des Druckwellen-
prozesses vernachlässigt wird. Das Modell ist mittels Identifikation
von vier physikalisch motivierten Modellparametern validiert. Damit
können die nicht messbare Leckage des Druckwellenladers, die nicht
messbare Mischzonenlänge und deren Konzentrationsprofil zwischen
Rauchgas und Frischluft bestimmt werden. Das validierte Druckwel-
lenladermodell zeigt einen Fehler in der Grössenordnung von 5%.

Das hier entwickelte Motormodell eines druckwellenaufgeladenen
Ottomotors ist ein Simulations-Werkzeug. Dieses Werkzeug kann
in einem zukünftigen Schritt für Systemanalysen und Systemopti-
mierung wie auch für modellbasierte Reglerentwürfe eingesetzt wer-
den.

Nomenclature

Abbreviations, Acronyms

BFE	:	Swiss Federal Office of Energy
EGR	:	exhaust gas recirculation
ETH	:	Swiss Federal Institute of Technology
GPV	:	gas pocket valve
PALOS	:	part-load optimized system
PWS	:	pressure wave supercharger
SI	:	spark ignition
WOT	:	wide open throttle

Defined Expressions

air side	:	the side of the cell where the ambient air flows into the PWS
channel	:	cross-sectional area where the fluid flows into and out of the PWS
gas side	:	the side of the cell where the exhaust gases flow into and out of the PWS
PWS Engine Model	:	dynamic simulation tool of the system "PWS SI engine"
PWS Model	:	static model of the pressure wave supercharger
"PWS SI engine"	:	entire system of the pressure wave supercharger and the SI engine
receiver	:	manifold, tube

Symbols

Symbol	Description	Unit
A	area	m^2
a	speed of sound	m/s
c	fraction	−
c_p	specific heat capacity	$J/kg/K$
D	cylinder-bore diameter	m
d	diameter	m
H	enthalpy	J
k_{stoich}	stoichiometric air-to-fuel ratio	−
l	length	m
m	mass	kg
mz	mixing zone	−
$\dot{m}$	mass flow	kg/s
n	rotational speed	rpm
n	polytropic exponent	−
n	number	−
p	pressure	Pa
pos	valve position	%
Q	heat	J
R	specific gas constant	$J/kg/K$
r	radius	m
t	time	s
T	temperature	K
u	fluid velocity	m/s
V	volume	m^3
w	wave velocity	m/s
x	EGR rate	−
x	x-coordinate	m
y	y-coordinate	m
α	angle	$^\circ$
Δ	difference	
δ	infinitesimal	
η	efficiency	−
κ	isentropic exponent	−
λ_l	volumetric efficiency	−
λ_v	air-to-fuel ratio after SI engine	−
λ_4	air-to-fuel ratio in channel 4	−

μ	dimensionless coordinate	$-$
π	pressure ratio	$-$
ρ	density	kg/m^3

Subscripts

a	air
act	actual
app	approximate
bf	back flow
c	close
c	compression
calc	calculated
cell	cell
cl	closing
chg	gas pocket channel
ch1	channel 1
ch2	channel 2
ch3	channel 3
ch4	channel 4
conv	convection
cw	cell wheel
cyl	cylinder
diff	diffusion
dis	(engine) displacement
e	exhaust gas
e	expansion wave (numbered)
eff	effective
egr	exhaust gas recirculation
em	exhaust manifold
eng	engine
ex	exact
e1	zone e1
e5	zone e5
e6	zone e6
e7	zone e7

e8	zone e8
fit	fitted
g	zone g
gs	gas side
hp	high pressure
i	inner
id	ideal
im	intake manifold
in	inside, input
le	leakage
lim	limes
lin	linear
lp	low pressure
m	mean
meas	measured
mx	mixed
mz	mixing zone
o	outer, open
out	outside, output
pws	pressure wave supercharger
r	reflected
rad	radiation
rec	receiver
red	reduced
rel	relative
s	shock wave (numbered)
s6	zone s6
s7	zone s7
stoich	stoichiometric
tanh	tangens hyperbolicus
theo	theoretical
v1	zone v1
v2	zone v2
v3	zone v3
x	zone x
y	zone y
z	zone z
1	zone 1

1s   zone 1s
2   zone 2
3   zone 3
4   zone 4

Chapter 1

Introduction

The first section of this chapter explains why supercharging a spark ignition engine can help to reduce fuel consumption and shows the motivation for this work. The second section defines the objectives of the presented work, and the third section describes how these objectives are reached. Finally, Section 1.5 summarizes the new results obtained by this work.

1.1 Supercharging an SI Engine

1.1.1 Downsizing and Supercharging for Minimal Fuel Consumption

Modern spark ignition (SI) engines are required to be equipped with a three-way catalyst in order to meet the current emission limits. Consequently, they have to be operated with stoichiometric air-to-fuel ratios. The engine torque thus may be controlled only by changing the intake manifold pressure, i.e., the throttle reduces the level of ambient pressure by energy dissipation to the level of intake manifold pressure. The engine then works at part-load conditions, which are characterized by a negative pressure difference over the engine:

$$p_{\mathrm{im}} - p_{\mathrm{em}} < 0 : \text{throttled engine operation}$$

The negative pressure difference between intake and exhaust manifolds causes pumping losses for the engine. This is the main reason why naturally aspirated SI engines have a poor efficiency at part-load conditions, see Inhelder (1996) and Heywood (1988). Among various approaches toward improving this situation several possibilities are found (see Eberle and Hörler (1988), Jenny (1991), Inhelder (1996), Lösing and Lutz (1999), and Soltic (2000)):

1. lean burn engines with direct injection of gasoline

2. high engine speed concept

3. downsizing and supercharging for high engine speed only

4. downsizing and supercharging over entire engine speed range

The concept 1 tries to reduce the fuel consumption by a lean engine operating mode which is still a subject of current research and therefore not further discussed here. In contrast, the engine concepts 2, 3, and 4 try to avoid the pumping losses of the engine by reducing the engine displacement. Compared to a regular SI engine, the downsized engine more often operates at high loads where the throttling losses hardly occur. This leads to negligible pumping losses. The engine then operates near its most economical operating point. The engine power lost by downsizing may be recovered by:

- Increasing the engine speed.

- Increasing the intake manifold pressure above ambient pressure.

The first concept is not a suitable choice for passenger cars due to the noise caused by an engine operating at high engine speeds. The second concept recovers the missing engine power by increasing the intake manifold pressure above ambient pressure. This may be realized by the adding a:

- mechanical charger

- turbocharger

- pressure wave supercharger

A charger compresses the fresh air either with the help of mechanical energy from the crankshaft of the engine (mechanical charger) or with the help of the exhaust gas enthalpy from the engine (turbocharger or pressure wave supercharger). In supercharged engine mode, the pressure difference over the engine becomes zero or even positive (see Fig. 1.1, showing a turbocharged SI engine as an example):

$$p_{im} - p_{em} \geq 0: \text{ supercharged engine operation}$$

The downsized supercharged engine operates more economically in the range between lower and medium loads compared to a naturally aspirated engine due to smaller pumping losses in this load range. Therefore, supercharging an SI engine may reduce the fuel consumption.
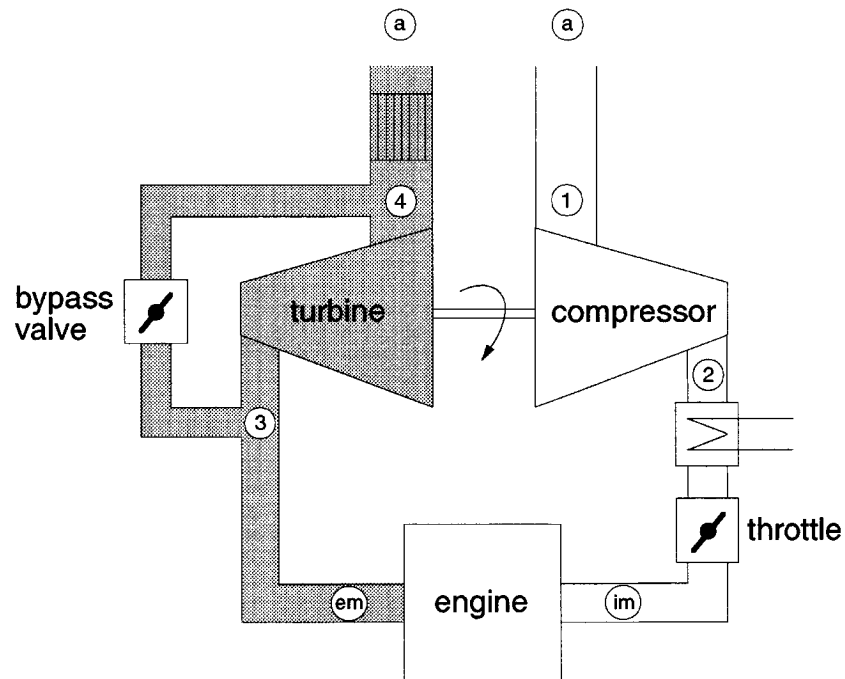
Figure 1.1: SI engine supercharged with a turbocharger with a bypass valve; a: ambient; im: intake manifold; em: exhaust manifold; 1: before compressor; 2: after compressor; 3: before turbine; 4: after turbine

1.1.2 Supercharging an SI Engine with a Pressure Wave Supercharger

In the *SAVE* project, described in Guzzella and Martin (1998), a downsized small SI engine is supercharged with a pressure wave supercharger (PWS). The main reasons for choosing a PWS as the charging device in that project are briefly explained in the following:

- **Leakage losses**: The expected exhaust gas volume flow of a small SI engine is very low. A turbocharger would have relatively high leakage losses over the turbine as a result of the very small turbine geometry. Therefore, its efficiency decreases. For a given desired boost pressure p_2, the lower turbine efficiency requires a higher exhaust gas pressure p_3 compared to the case without leakage losses over the turbine (for the nomenclature of the pressures see Fig. 1.1). This causes increased pumping losses for the engine. In contrast to a turbocharger, the expected leakage losses of a PWS for the same small engine are lower (Hörler (1969)). Thus, pumping losses in supercharged mode are negligible.

- **Incidence losses**: Typically, in an SI engine the exhaust gas volume flow varies over a wide range. The varying volume flow, together with the actual pressure and temperature before turbine and the turbine rotational speed, cause incidence losses for the turbine (Traupel (1988)). These losses lower the turbine efficiency and, for the same reasons as explained above, lead to an increased fuel consumption. Since the working efficiency of a PWS does not depend on the absolute value of the exhaust gas volume flow, its efficiency is fairly high over a wide operating range of an engine. Boost pressure p_2, intake manifold pressure p_{im}, exhaust gas pressure p_{em}, and pressure before charging device p_3 are approximately equal when the engine is supercharged with a PWS. Thus, the approximately equal values of the intake manifold pressure and the pressure before charging device lead to negligible pumping losses.

- **Mass flow characteristic**: Due to the turbine flow characteristic, the surge line of the compressor, and the relatively thicker boundary layer at the blades in the case of a turbocharger for

small SI engines (Traupel (1988)), the maximum boost pressure at low air mass flows and therefore at low engine speeds is smaller than for a PWS (Gygax and Schneider (1988), Kollbrunner (1980)). Since good driveability is characterized by high engine torque at low engine speeds, a PWS may be the preferable charger for small SI engines.

- **Supercharging over entire engine speed range**: The charging device is coupled to the engine for all engine operating points and compresses the air over the entire engine speed range. In contrast, when a downsized engine is supercharged with a mechanical charger, the engine is supercharged only at higher engine speeds since the inner compression ratio of the combustion engine does not need to be reduced in order to avoid the problem of knocking at low engine speeds. Therefore, at low engine speeds the mechanical charger must be uncoupled from the engine. In order to guarantee good driveability, the engine torque may not change during the uncoupling and coupling of the charger. As this torque constancy still is an unsolved problem, a mechanical charger was out of question.

- **Controlling compression ratio of the charger**: The PWS analyzed in this project has a bypass valve – the gas pocket valve (GPV) – which allows to control the exhaust gas enthalpy available for the charging process. The actuator GPV not only avoids engine knocking by controlling intake manifold pressure, but it also widens the range in which the SI engine operates without pumping losses, see Mayer et al. (1990). The reason is that bypassing that part of the exhaust gas mass flow whose enthalpy is not needed for the compression process lowers the pressure before the charging device.

1.2 Motivation for the Research Presented

If an SI engine is supercharged with a PWS, not only boost pressure has to be controlled in order to avoid engine knocking, but also external exhaust gas recirculation (EGR). If the fraction of the re-

circulated exhaust gases within the cylinder is lower than a certain level (approximately 20%, see Heywood (1988)) the recirculated exhaust gases lower the engine torque as a result of a lack of oxygen, above that level misfiring may lead to a complete breakdown of the engine torque. Therefore, in order to guarantee good driveability of a car powered by a pressure wave supercharged SI engine, undesirable EGR must be avoided.

Undesirable EGR may occur in steady-state and transient engine operating conditions since the exhaust gases and the fresh air are in direct contact during the supercharging process of a PWS. This leads to the motivation of this work which is formulated in the following:

- Understand the interaction between the pressure wave supercharger and the SI engine.

- Understand the physics of steady-state exhaust gas recirculation and of transient exhaust gas recirculation during load steps.

Therefore, a combined model of a pressure wave supercharger with gas pocket valve and an SI engine is developed and tested on a dynamic engine test bench.

Until now, two main types of PWS models exist:

- On the one hand, models used for control purposes which are based on *black box approaches* (e.g., Pfiffner (2001)) or *grey box approaches* (Pauli and Amstutz (1989), Pfiffner et al. (1997)). In the case of a *black box approach* the model is not physically based and therefore can only be derived from measurement data. Thus, it must not be used for model extrapolation. If a model is based on a *grey box approach*, some processes are modeled using physical laws. Nevertheless, this model approach requires a lot of "magic" functions in order to validate the model. Since these "magic" functions have to be identified by measurement data and do not represent physical effects, models based on *grey box approaches* may not be extrapolated as well.

- On the other hand, there exist models based on the formulation of partial differential equations in one or two spatial dimensions, as presented in Zehnder (1970), Zehnder (1971), Wallace and Aldis, and, more recently, in the work of Piechna

(1998a), Piechna (1998b), Piechna (1999), Selerowicz and Piechna (1999). These models focus on calculating a snapshot of the system states of interest. However, the computation times required do not permit the simulation of the PWS model together with an engine model in real time.

The modeling approach presented here is a *white box approach* which fills the gap between the two already existing modeling approaches. If a model is based on a *white box approach*, the model takes into account all the effects of first order by physically based relations and neglects effects of higher order. Thus, this model approach still requires model parameters for the validation of the model. However, these model parameters have to describe physical phenomena. Then, the model parameters can be derived from a small range of measurement data and they may be extrapolated. Since less important effects are neglected and iteration usually is not needed, the resulting model can be computed in real time.

1.3 Goals

The objective of the research described here is to develop a simulation tool which predicts the stationary and transient behaviors of the whole system "PWS SI engine" with satisfactory accuracy in real time.

As a first step, the main part of the system is modeled, namely the PWS. The resulting static model is called *PWS Model*. Using measured states as input data, the *PWS Model* has to predict the states of interest with a relative error smaller than 5%.

In a next step, a mean value model of an engine system is developed in order to connect the *PWS Model* to the engine system model. The resulting *PWS Engine Model* is a simulation tool which is able to simulate the transient working behavior of the system "PWS SI engine". The relative error of the characteristic time constants of the simulation tool *PWS Engine Model* has to be smaller than 10%. This relative error is larger than the one for the *PWS Model* since errors of the submodels are cumulative.

Both the *PWS Model* and the *PWS Engine Model* have to be physically based. Such a *white box approach* permits, on the one hand, the simulation tool to be adapted to other engine and PWS

sizes and, on the other hand, to compute the model with extrapolated values.

In summary, the main objectives of the research described here are the following :

1. The development of a mean value model of a PWS which can be integrated as a submodel into an engine system model in order to simulate the steady-state and the transient operating behavior of a PWS together with an SI engine.

2. The modeling approach has to be physically based (*white box approach*) in order to allow model extrapolation.

3. The relative error of the *PWS Model* has to be smaller than 5%.

4. The relative error of the simulation tool *PWS Engine Model* during transients has to be smaller than 10%.

5. The simulation tool has to simulate the processes in real time in order to ensure that the model proposed here can be used – in a future step – for controller design.

1.4   Approach

In order to model the entire system "PWS SI engine", the system is substructured into devices which can store mass and energy (receivers) and devices which produce the flows between these receivers (generalized throttles). The relevant dynamics of the model are represented by the energy and mass storage of the "receivers", whereas "the throttles" are described by static algebraic relations.

The main part of the simulation tool *PWS Engine Model* is the static submodel *PWS Model*. The PWS is modeled as a generalized "throttle", i.e., the outputs of the *PWS Model* are mass and enthalpy flows. The model neglects the fast dynamics of building a new stationary pressure wave diagram since the dynamics of the system caused by the filling-emptying process of the tubes are predominate. The *PWS Model* calculates a simplified pressure wave process and the corresponding pressure wave diagram, based on the theory of the one-dimensional, linear gas dynamics (Sauer (1960), Zierep (1963)). The *PWS Model* is validated by steady-state measurements.

Other static submodels of the simulation tool are the SI engine, the throttles, and the catalysts. Neglecting any delays of the combustion process, the SI engine is modeled as a generalized pump. Both the throttles and the catalysts are described by static functions.

The tubes of the system "PWS SI engine" are represented by receivers in the simulation tool *PWS Engine Model*. The receivers define the relevant dynamics of the system. In the control volume of each receiver, mass and energy balance equations are solved, taking into account convection and radiation for the heat losses through the control volume. One receiver volume represents the thermal mass of the system "PWS SI engine" and therefore defines the slow dynamics of the system.

Connecting all these submodels, we obtain the simulation tool *PWS Engine Model*. All models are based on matlab/simulink.

1.5 Main Contributions

The main contributions of this research are:

- Description of the pressure wave process of a pressure wave supercharger including steady-state exhaust gas recirculation by a physically based mean value model approach. The model calculates the outputs as a function of the measured states as pressures and temperatures in the channels of the PWS and of the actual PWS rotational speed. The calculation is based on the algebraic relations of the one-dimensional linear gas dynamics. The resulting model is the static model *PWS Model* whose outputs show an error which is smaller than 5%.

- Derivation of the nonmeasurable, PWS typical leakage losses out of the cell wheel, the nonmeasurable mixing zone length, and its exhaust gas fraction profile by model parameter identification.

- Development of a simulation tool capable of simulating the transient working behavior of a pressure wave supercharger together with an SI engine including transient exhaust gas recirculation effects. Due to the fact that the simulation tool *PWS Engine Model* is a physically based *white box approach*,

the simulation tool can be computed in real time and with extrapolated input data. The model error is in a satisfactory range.

- Presentation and explanation of one possibility of how transient exhaust gas recirculation during a load step can be avoided. Moreover, this study points out clearly the working principle of the gas pocket valve and explains its influence on the pressure wave process.

- Development of a simulation tool which can be used for system analysis, system optimization, and model based controller design.

Chapter 2

System Description

The first section of this chapter outlines the individual parts of the entire engine system, whereas the second section documents the control approach of the system and points out the problem of controlling EGR. The third section introduces the working principle of the pressure wave supercharger with gas pocket valve.
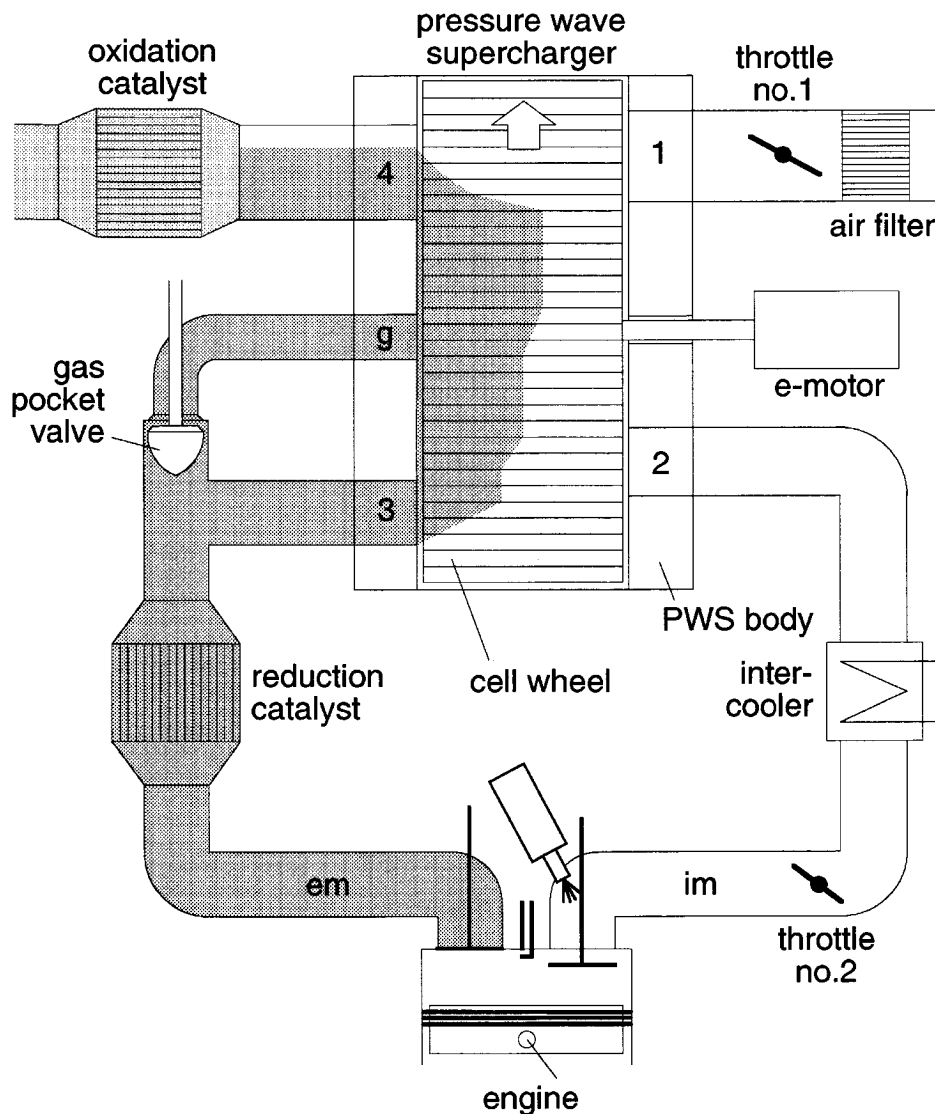
2.1 System Structure

The engine under consideration is a small spark ignition (SI) engine supercharged with a pressure wave supercharger (PWS) with gas pocket valve (GPV, see Mayer et al. (1990)). This engine is part of the *SAVE* project, described in Guzzella and Martin (1998), Cortona (2000), and Soltic (2000). The whole system consists of the SI engine, the PWS, the tubes of the inlet and outlet system, three throttles, an intercooler, an air filter, and two catalysts (Weber and Guzzella (2000)), as shown in Fig. 2.1.

The SI engine is a two-cylinder four-stroke engine with a displacement of 360 ccm (SAB360, see Appendix A). Its air-to-fuel ratio is controlled to be slightly "rich" ($\lambda_v \approx 0.98 \dots 1.00$).

The PWS has a cell wheel whose length and diameter are approximately equal ($l_{cw} \approx d_{cw} \approx 64mm$). It is driven by an electrical motor and therefore can be adjusted independently of the engine speed. In contrast to other PWS with GPV, e.g., as described in Croes (1979),

11

Mayer et al. (1990), this GPV is separated from the PWS body. The
exhaust gases flowing through the GPV enter the PWS via the gas
pocket channel (channel g) which is completely detached from the
channel area of channel 3.

Figure 2.1: System structure of the pressure wave supercharged
SI engine SAB360: pressure wave supercharger with gas
pocket valve

The exhaust gas enthalpy flowing through channel 3 into the PWS
is used for the compression process of the fresh air which enters the
PWS through channel 1 (Fig. 2.1). One part of the compressed fresh

air then flows out of the PWS through channel 2 towards the SI engine. The other part remains in the cell wheel, together with the exhaust gases. The exhaust gas enthalpy entering the PWS through channel g does not deliver any energy to the compression process of the fresh air but to the scavenging process of the cell wheel. During the scavenging process the exhaust gases from channel 3 and channel g flow through channel 4 towards the oxidation catalyst, together with some fresh air of the fresh compressed air which remains in the cell wheel after the compression process. The fresh air in channel 4 is called scavenging air. As a result, the fresh air flowing through channel 1 into the PWS is the sum of the compressed fresh air in channel 2 and the scavenging air in channel 4.

The throttle no. 2 controls the engine torque in the naturally aspirated mode, whereas the throttle GPV is the actuator that controls engine torque in the supercharged mode. In this mode the throttle no. 2 is fully open (WOT) in order to avoid unnecessary pumping losses of the SI engine (Heywood (1988)).

The intercooler cools the charged air almost to ambient temperature in order to achieve high engine torque.

The aftertreatment of the exhaust gases is done in two steps. The reduction catalyst is the first catalyst. Due to the slightly rich air-to-fuel ratio it primarily reduces the NO_x. The oxidation catalyst is the second catalyst. It oxidizes the remaining CO and HC with the help of additional fresh air from the manifold 1.

The throttle no. 1 allows to lower the pressure in manifold 1. As a result, the amount of fresh air in manifold 4, the scavenging air, decreases. Hence, the mixing temperature in manifold 4 increases. Therefore, as long as the scavenging air mass flow is not zero, the operating conditions in the oxidation catalyst can be improved using throttle no. 1 in order to lower the pressure p_1.

2.2 Controlled State Variables

2.2.1 Present Control Approach

Besides the control of the air-to-fuel ratio the controlled state variables of the engine system are:

- Intake manifold pressure: Engine knocking must be avoided.

Therefore, the intake manifold pressure p_{im} is limited to a given maximum value which is a controller parameter. Since this pressure limit only is reached when the engine operates in supercharged mode (WOT), the actuator that controls the intake manifold pressure is the gas pocket valve.

- Temperature before oxidation catalyst: The control of the temperature before the oxidation catalyst allows to guarantee a high conversion rate in the oxidation catalyst. This temperature is controlled by the actuator throttle no. 1, see Fig. 2.3. By closing the throttle no. 1 the pressure p_1 can be lowered. As a result, the scavenging air in manifold 4 decreases. This causes an increasing temperature T_{ch4}. However, in order to guarantee zero EGR, the pressure p_1 may be lowered only to the level at which the PWS still completely scavenges.

- Rotational speed of the PWS: The rotational speed of the PWS must be controlled in order to guarantee a pressure wave process which is adjusted to the actual thermodynamic boundary condition in the manifolds next to the PWS. If the focus is on maximum engine torque, the rotational speed of the PWS is set to this value where the intake manifold pressure p_{im} is maximal. If the target is minimal fuel consumption of the engine, the rotational speed of the PWS has to be chosen the way that the ratio p_2/p_3 is maximal (Fig. 2.2). In this case, the pumping losses of the engine are minimal.

- Exhaust gas recirculation: The exhaust gases recirculated within the PWS must be avoided because engine torque would be reduced by EGR as a result of a lack of oxygen in the cylinder or even break down if the recirculated exhaust gases cause misfiring. The actuators that control EGR are both the throttle no. 1 and the GPV. As mentioned above, the closing position of the throttle no. 1 is limited by the constraint of zero EGR. The values of the allowable closing positions are experimentally determined. In stationary engine operating mode the position of the throttle no. 1 follows these values as a function of engine speed and intake manifold pressure. During a load step, when the GPV is closed, the throttle no. 1 is fully opened as fast as possible in order to guarantee optimal conditions for complete

scavenging. Despite this opening, the scavenging process may be incomplete if the closing velocity of the GPV is too fast. Therefore, the GPV is the second actuator for controlling EGR. By limiting the maximum closing velocity of the GPV, the PWS also scavenge completely during transients. Summarizing, the actuator throttle no. 1 controls EGR in steady-state engine operating conditions, whereas the actuators throttle no. 1 and GPV control EGR during load steps.
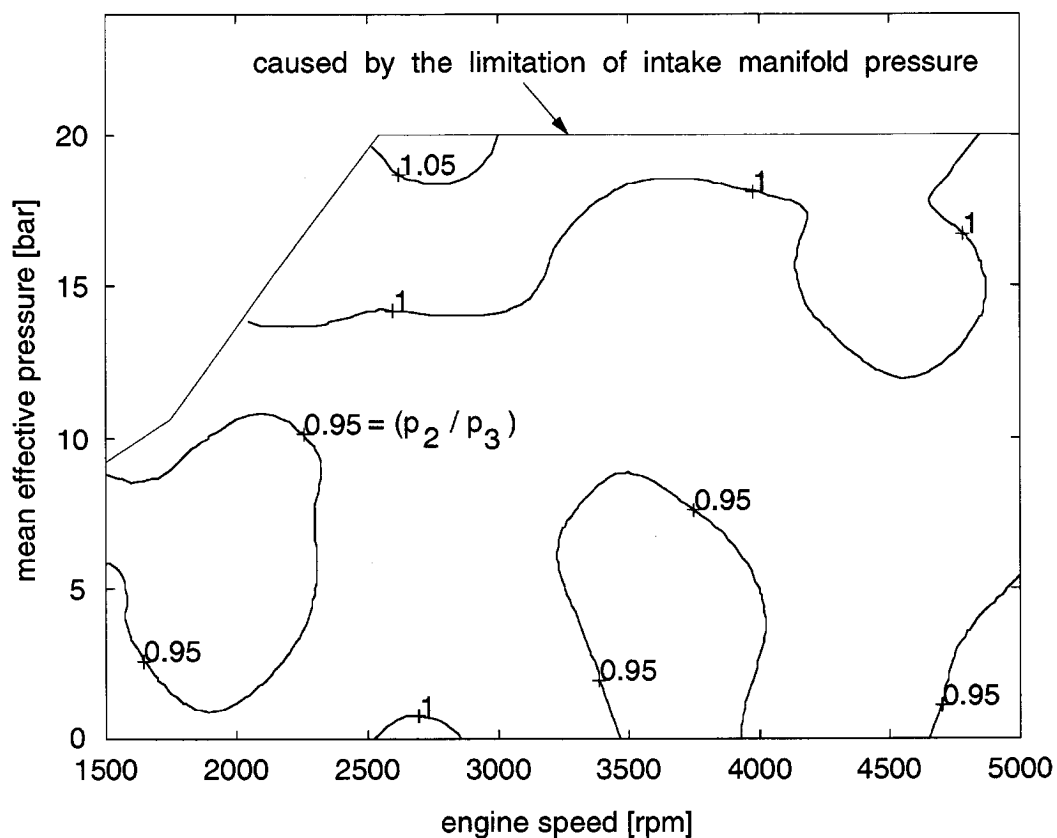

Figure 2.2: Measured ratio of p_2/p_3 in the investigated engine operating range of the engine SAB360

2.2.2 Avoiding EGR

The problematic nature of controlling EGR is that the start of an exhaust gases recirculation event during a load step cannot be detected fast enough in order to guarantee zero EGR. An air-to-fuel ratio sensor

in manifold 4, e.g., would indicate a deteriorated scavenging process during a load step (see Fig. 2.3), but this information would be too late for the avoidance of EGR, since the PWS already does not scavenge completely. Another possibility would be to detect EGR by measuring the position of throttle no. 2 and intake manifold pressure. Again, the information is too late.
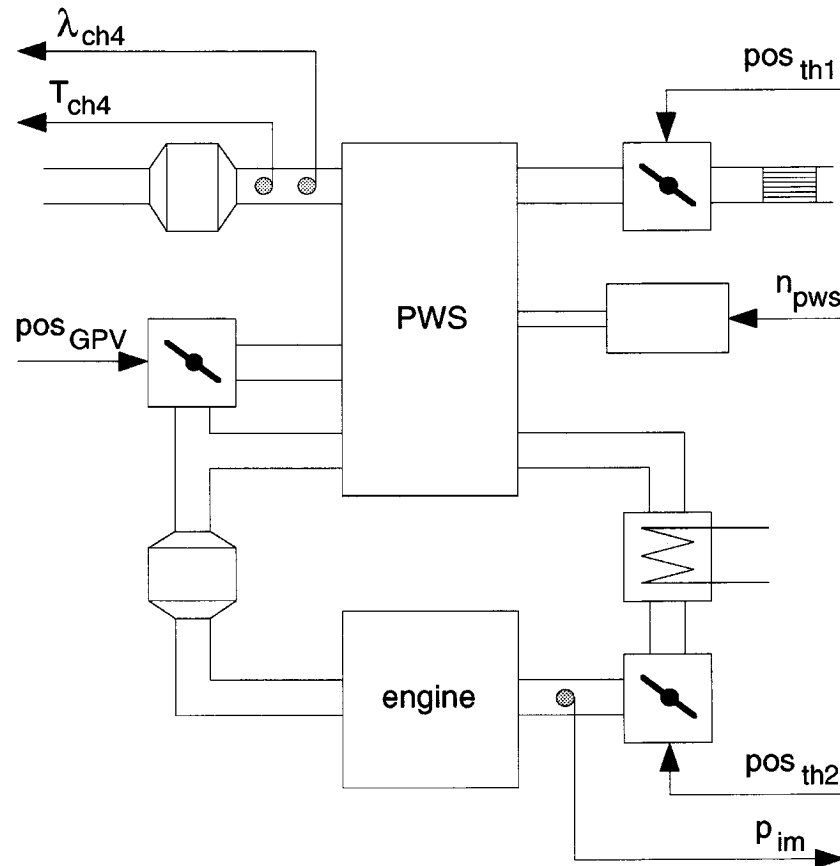
Figure 2.3: Controlled state variables and the actuators of the pressure wave supercharged SI engine SAB360 (air-to-fuel ratio control not depicted)

Therefore, if zero EGR has to be guaranteed, the maximum closing velocity of the GPV must be limited. The allowable closing velocity can be determined in two ways:

1. Experimental determination of the maximum closing velocity of the GPV. The closing velocity must be varied at numerous engine operating points in order to guarantee zero EGR for any

load step independent of the step size and of the engine operating point.

2. Model based determination of the maximum closing velocity of the GPV. Since the model is physically based, the amount of experiments is significantly reduced. A small set of measurement data is sufficient, firstly, to validate the model, and, secondly, to verify the allowable closing velocity of the GPV which results from simulation.

The first step of a model based determination of the maximum GPV closing velocity is developing a model of the entire engine system. This first step is described in the presented work. The second step is to use the model for system optimization and model based controller design. The second step is the goal of future research.

2.3 The Pressure Wave Supercharger

In the first subsection, the working principle of a pressure wave supercharger (PWS) are explained for zero exhaust gas recirculation (EGR) and without a mixing zone between exhaust gases and fresh air in the cell wheel. The second subsection points out the function of the gas pocket valve (GPV). The third subsection then shows the pressure wave process for EGR including a mixing zone.

2.3.1 Pressure Wave Process Without EGR and Without Mixing Zone

The working principle of a PWS is best explained by describing the state change of the fluid in one cell of the PWS cell wheel during one full rotation of the wheel.

The state change of the fresh air and of the exhaust gases is visualized in the *state diagram*, see Fig. 2.4. Please notice that the axes in the *state diagram* are not dimensionless, in contrast to literature, e.g., in Hörler (1969). The state diagram shows the different states of the fresh air and of the exhaust gases in the same cell over the whole wave process. The state is defined by the static pressure and the velocity. It is common to connect these individual state points
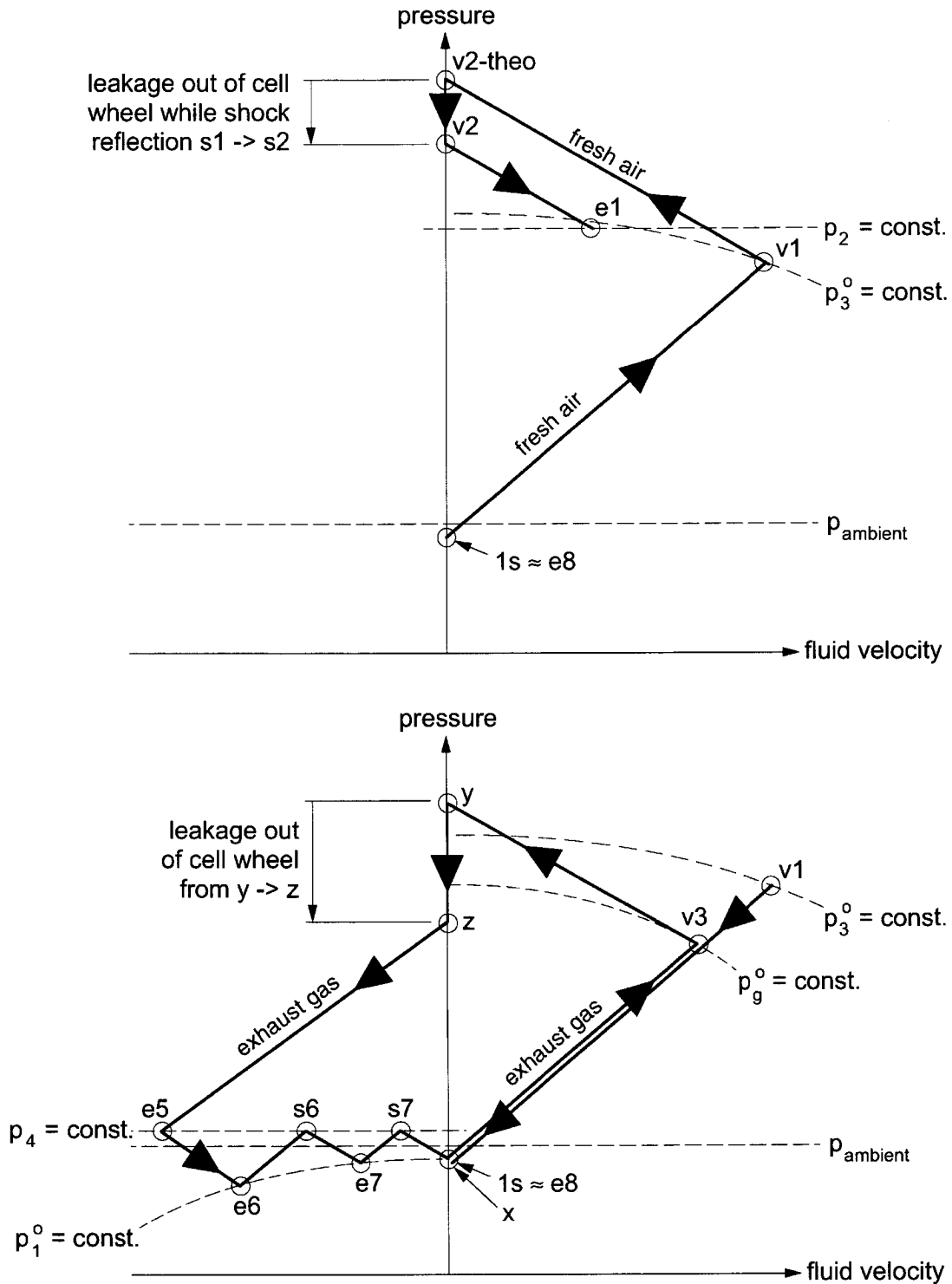
Figure 2.4: State changes in the *state diagram*; Above state changes of fresh air: $1s \rightarrow v1 \rightarrow v2 - theo \rightarrow v2 \rightarrow e1$; Below state changes of exhaust gases: $v1 \rightarrow x \rightarrow v3 \rightarrow y \rightarrow z \rightarrow e5 \rightarrow ... \rightarrow 1s$ (axes not dimensionless)

with a line, although the state of the fluid changes abruptly from one state to the next one.

The geometrical relations between waves, contact front, and PWS body geometry are depicted in the *wave diagram*, see also Berchtold (1961), Croes (1979), Gyarmathy (1983). The cycle for the fluid in the cell starts at state $1s$, see Fig. 2.5. The description of the state change is divided into the two parts "high pressure part" (state $1s$ to state z) and "low pressure part", which starts with the opening of channel 4.
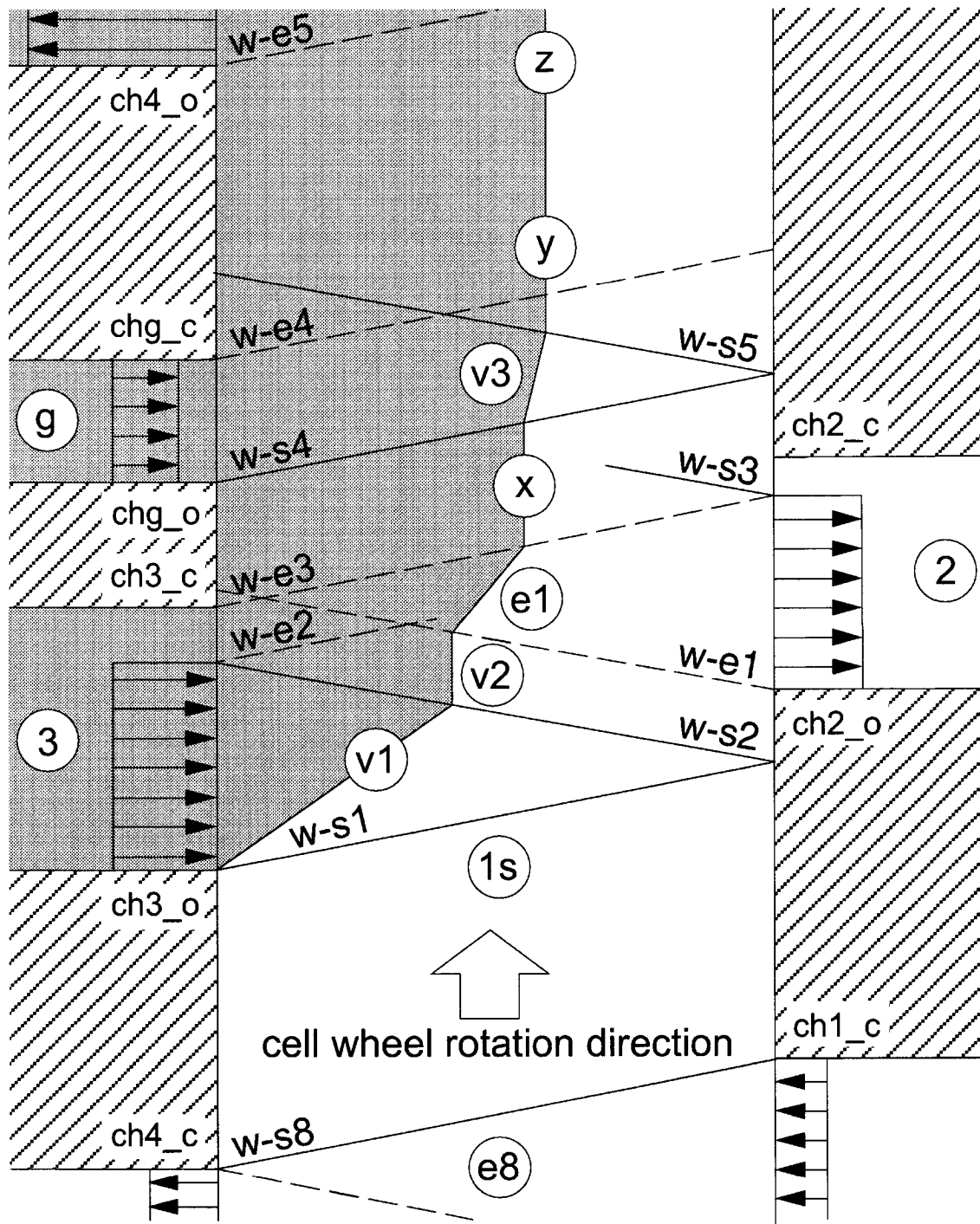
High Pressure Part

The fluid at state $1s$ consists of fresh air only, which flew into the cell from channel 1. The fluid velocity is zero due to the boundary condition *wall* (Croes (1979)) both on the gas and on the air side. Pressure and temperature are approximately the same as in channel 1, see Fig. 2.4. The explanation for this fact follows at the end of the description of the pressure wave process.

$$\text{State } 1s: \begin{cases} u_{1s} & = 0 \qquad \text{: boundary condition} \\ p_{1s} & \approx p_1 \\ T_{1s-a} & \approx T_1 \end{cases}$$

The rotation of the cell wheel transports the cell to the point where channel 3 opens. This triggers the first event: the primary compression process. Due to the pressure ratio $p_3/p_{1s} > 1$ and the sudden opening of channel 3 a pressure wave $s1$ starts to move. It compresses the fresh air in the cell up to the static pressure p_3, see Fig. 2.4, and the temperature rises polytropically. At the place in the cell where the shock wave $s1$ has already passed, the fluid – exhaust gases and fresh air – is moving with the same velocity towards the air side. The fact that two media standing in contact have always the same pressure and velocity is the consequence of the *contact condition* (Sauer (1960), Zierep (1963)).

$$\text{State } v1: \begin{cases} u_{v1} & = u_3 \qquad \text{: contact condition} \\ p_{v1} & = p_3 \qquad \text{: contact condition} \\ T_{v1-a} & > T_{1s-a} \\ T_{v1-e} & = T_3 \end{cases}$$

Figure 2.5: Simplified pressure wave diagram of high pressure part without mixing zone and zero EGR

When the wave $s1$ meets the air side, the fluid flows with the velocity u_{v1} over the whole cell length. The boundary condition *wall* at the air side demands zero velocity. In order to satisfy this condition, the secondary compression wave $s2$ starts, compresses the fluid in the cell above the value of p_3 and decelerates the fluid to zero velocity. The theoretical pressure rise (state point $v2 - theo$ in Fig. 2.4) is lowered by leakage losses out of the cell. If the rotational speed of the PWS is well tuned to the states $1s$ and 3, the wave $s2$ meets the gas side exactly when channel 3 closes. For a short moment, the cell is closed at both sides.

$$\text{State } v2: \begin{cases} u_{v2} & = 0 \qquad : \text{boundary condition} \\ p_{v2} & > p_{v1} \\ T_{v2-a} & > T_{v1-a} \\ T_{v2-e} & > T_{v1-e} \end{cases}$$

With the opening of channel 2, the fluid in the cell gets in contact with the fluid in channel 2 with the lower pressure p_2. Due to the boundary condition *same pressure*, see Fig. 2.4, the fluid expands in the expansion wave $e1$ to p_2. In a first approximation the pressure in channel 2 remains constant regardless of the outflowing mass since the volume of the cell is much smaller than that of channel 2. Also for $p_{v1} = p_2$ the expanded temperature T_{e1-a} is slightly higher than T_{v1-a} since the state change in a compression process is polytropic and in an expansion process approximately isentropic, see Hörler (1969), Baehr (1992).

$$\text{State } e1: \begin{cases} p_{e1} & = p_2 \qquad : \text{boundary condition} \\ u_{e1} & \neq 0 \\ T_{e1-a} & = T_{v1-a} + \Delta T_{v1-a} \\ T_{e1-e} & = T_{v1-e} + \Delta T_{v1-e} \end{cases}$$

If the rotational speed of the PWS is not well tuned to the states $1s$ and 3, channel 3 is still open when $s2$ meets the gas side. In this case the fluid in the cell expands over the expansion wave $e2$ to p_3 by flowing into channel 3 (backflow). The resulting fluid velocity from the point where $e2$ starts until channel 3 closes in a first approximation is zero. This lowers the exhaust gas enthalpy flowing into the PWS. Consequently, maximal boost pressure (p_2) is not achieved. The same problem of backflow exists at the air side, when the wave $e3$ meets

the open channel 2 and is reflected as the shock wave s3. For a well tuned rotational speed of the PWS, the wave e2 is identical with the wave e3 and backflow does not occur.

After channel 3 has closed, the boundary condition *wall* at the gas side demands zero velocity. This condition can only be satisfied by an expansion wave, because the fluid in the cell is running away from the wall at the gas side. The expansion wave e3 decelerates the inflowing exhaust gases to zero velocity and lowers pressure and temperature. The fluid's state is the state x.

$$\text{State } x: \begin{cases} u_x & = 0 \quad\quad : \text{boundary condition} \\ p_x & \approx p_{1s} \\ T_{x-a} = T_{1s-a} + \Delta T_{1s-a} \\ T_{x-e} < T_{v1-e} \end{cases}$$

Neglecting wave reflections at the contact front, the next relevant process part starts when channel g opens. The reason for the inflow process caused by the shock wave s4 is the low pressure p_x.

$$\text{State } v3: \begin{cases} u_{v3} & = u_g \quad : \text{contact condition} \\ p_{v3} & = p_g \quad : \text{contact condition} \\ T_{v3-a} > T_{x-a} \\ T_{v3-e} = T_g \end{cases}$$

Either the reflected shock wave s5 or the expansion wave e4 decelerate this second inflow process to zero velocity, depending on which wave first meets the contact front. The reason for the wave s5 as well as for e4 is the boundary condition *wall*, for s5 at the air side (fluid flows against the wall), and for e4 at the gas side (fluid flows away from the wall). As a result of the deceleration the pressure rises from field v3 to field y.

$$\text{State } y: \begin{cases} u_y & = 0 \quad\quad : \text{boundary condition} \\ p_y & > p_{v3} \\ T_{y-a} > T_{v3-a} \\ T_{y-e} > T_{v3-e} \end{cases}$$

After channel g has closed, the cell contains all exhaust gases flowing through channel 3 and channel g into the cell wheel. It also contains compressed fresh air, which did not flow out through channel 2

towards the engine. In the following, this compressed fresh air is called *unused compressed fresh air*. At state y, the exhaust gas penetration has reached its maximum. The *high pressure part* of the pressure wave process is finished.

Due to the high pressure level in the cell compared to the one in channel 4 and channel 1, respectively, pressure is reduced by leakage out of the cell, through the gap between cell wheel and PWS housing, into channel 4 and channel 1, see state changes in Fig. 2.4. During the leakage process, temperatures in the cell evolve isentropically.

$$
\text{State } z: \quad
\begin{cases}
u_z & = 0 & : \text{boundary condition} \\
p_z & < p_y & : \text{result of leakage} \\
T_{z-a} & < T_{y-a} \\
T_{z-e} & < T_{y-e}
\end{cases}
$$

Low Pressure Part

When channel 4 opens, the fluid in the cell gets in contact with the lower pressure p_4 in channel 4, see Fig. 2.6. This triggers the first relevant process in the *low pressure part*: the first expansion wave $e5$ accelerates the fluid in the cell towards channel 4. The scavenging process of the cell wheel has started. The opening of channel 1 triggers the second relevant process: the deceleration of the first scavenging velocity by all following waves – alternating expansion and compression waves. The reason is the *positive low pressure difference*

$$
\Delta p_{\mathrm{lp}} := p_4 - p_1 > 0 \tag{2.1}
$$

which results from several pressure losses: air filter, friction in the tube 1 and 4, and pressure losses over the oxidation catalyst.

In an SI engine that works without external EGR, the target of the scavenging process is to move all burnt gases out of the cell wheel into channel 4. This can happen in three different ways:

1. The contact front leaves the cell wheel exactly at the place where channel 4 closes. No fresh air is in channel 4, the *unused compressed fresh air* remains completely in the cell wheel.

2. Part or all of the *unused compressed fresh air* leaves the cell wheel towards channel 4. The fresh air in channel 4 is called scavenging air.
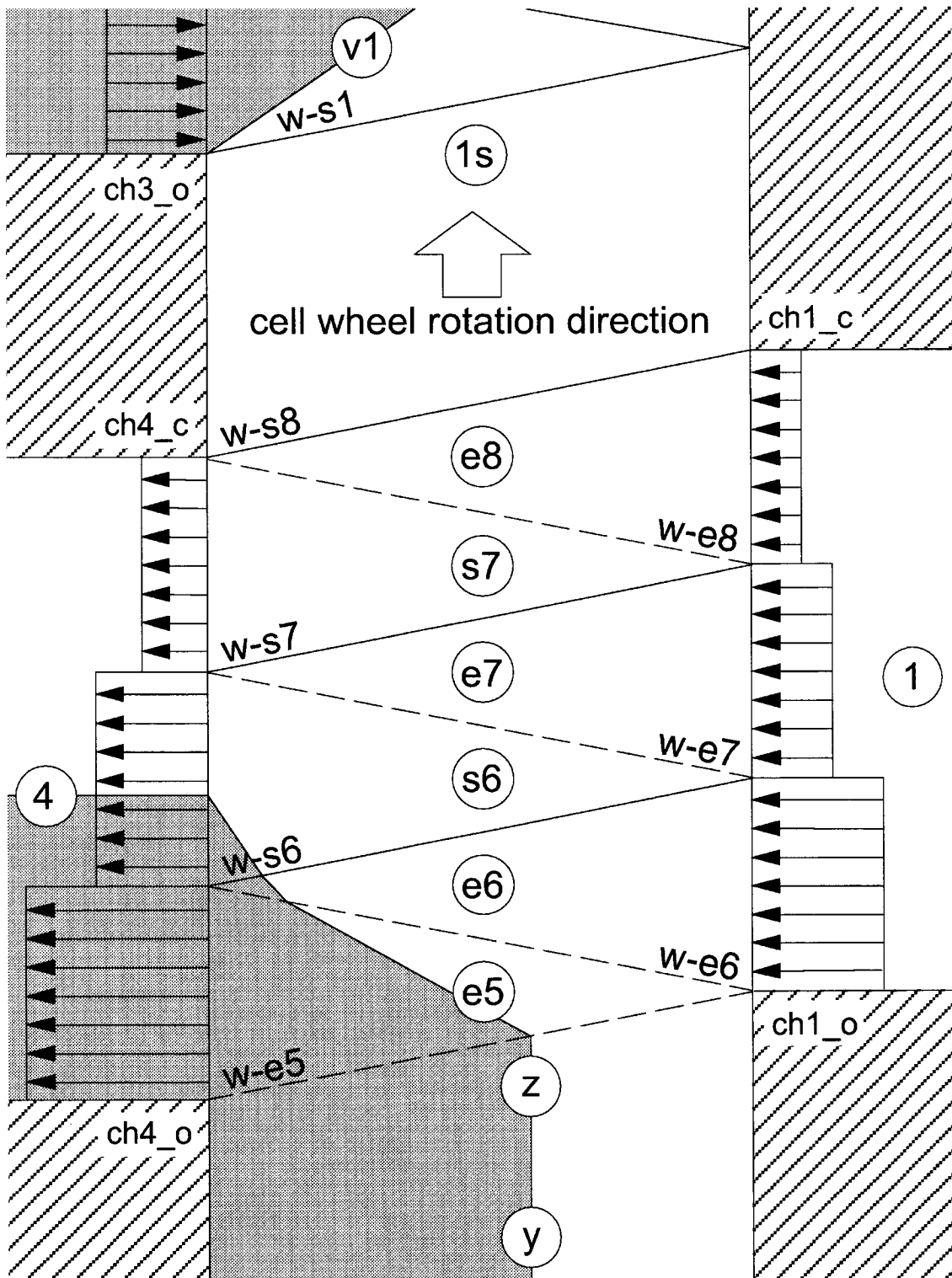
Figure 2.6: Simplified pressure wave diagram of low pressure part without mixing zone and zero EGR

3. Not only all *unused compressed fresh air* flows into channel 4, but also some additional fresh air coming directly from channel 1.

Scavenging air in channel 4 increases from 1) to 3). Responsible for that is the rising *scavenging energy*:

$$e_{\mathrm{sc}} \propto \frac{p_z}{p_4 - p_1} \qquad (2.2)$$

According to Eq. 2.2, two criteria for complete scavenging exist:

- Fairly low leakage → p_z sufficiently high.

- Geometry of tube 1, air filter, tube 4, and oxidation catalyst generously sized and with a smooth shape → Δp_{lp} sufficiently small.

The *low pressure part* finishes with the boundary condition *wall* either at the gas or at the air side, which causes either a final compression or an expansion wave, depending on the geometry and the actual rotational speed of the PWS. For the case of zero EGR the fluid in the cell consists of fresh air from channel 1 and, depending on the scavenging energy, of some *unused compressed fresh air*, which did not leave the cell wheel towards channel 4. This part of *unused compressed fresh air* repeatedly goes through the entire wave process until it completely leaves the cell wheel, Spinnler and Jaussi (1986).

The rotation of the cell wheel transports the cell from the closed channel 1 to the opening of channel 3. Neglecting a small heat transfer, the cell temperature does not change. Leakage does not occur due to $p_1 \approx p_{\mathrm{a}}$. Thus, the pressure also remains constant. The state of the fluid is now 1s. One full cycle is finished.

2.3.2 The Gas Pocket Valve

In the *high pressure part* the exhaust enthalpy from channel 3 is used for compressing the fresh air running into channel 2. Bypassing some exhaust gases through the gas pocket valve (GPV) while the throttle no. 2 is fully open (WOT), the exhaust gas pressure in channel 3 is reduced (Fig. 2.1). This lowers the compression of the fresh air in channel 2 and therefore engine torque. The engine then operates in

supercharged mode but not at full load condition. Besides that, the exhaust gas enthalpy flowing through the GPV increases the pressure p_y relatively to p_g because the pressure gain due to the deceleration from state $v3$ to y increases. The higher pressure p_y also produces a higher p_z. Consequently, the GPV fulfills two tasks:

- It controls the compression rate of the fresh air in channel 2.

- It produces the highest scavenging energy possible, even at engine part-load conditions.

## 2.3.3   Pressure Wave Process With EGR and With Mixing Zone

In contrast to a turbocharger, exhaust gases and fresh air are in direct contact in the cell wheel of a pressure wave supercharger. This is the main reason for unforced external exhaust gas recirculation. Two ways of external exhaust gas recirculation exist: *low pressure EGR* and *high pressure EGR*. These two paths are described in the following subsection. Afterwards, the phenomenon of transient exhaust gas recirculation is explained (Sec. 2.3.3).

Stationary Exhaust Gas Recirculation

The *wave diagram* in Fig. 2.7 a) shows the situation for steady-state *low pressure EGR* including a mixing zone.

Although the mean contact front (exhaust gas fraction = 50%) leaves the cell wheel into channel 4, some exhaust gases still remain in the cell wheel because of the mixing zone. With the beginning of the next pressure wave cycle, this exhaust gas remnant is added to the new mixing zone. Therefore, it will appear in channel 2 after a few (3 ... 5) cell wheel revolutions. Due to the mixing zone, there is also some fresh air in channel 4 during *low pressure EGR*. This explains why steady-state EGR occurs together with still some scavenging air in channel 4. Steady-state *low pressure EGR* is therefore caused by scavenging energy being too low (see Eq. 2.2).

Steady-state EGR can also be caused by *high pressure EGR*. In this case, together with the mixing zone at the place where channel 2 closes the exhaust gas penetration is larger than the cell length and ends in
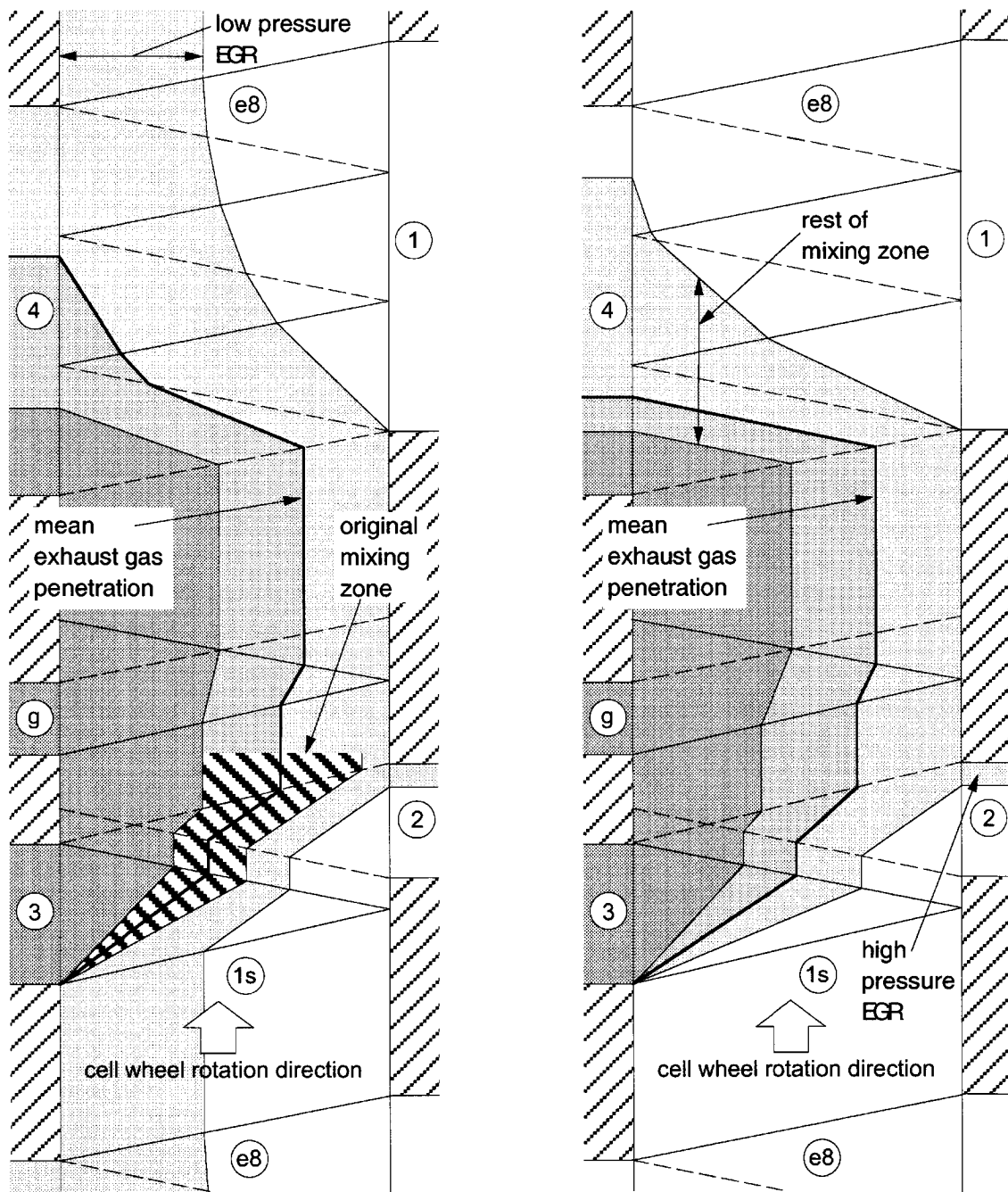
Figure 2.7: Simplified pressure wave diagram with mixing zone and EGR; Left: a) EGR caused by incomplete scavenging; Right: b) EGR recirculated directly from channel 3 into channel 2

the open channel 2. This situation is shown in the wave diagram to the right in Fig. 2.7 b). There are two reasons for too large an exhaust gas penetration:

- Boost pressure p_2 much smaller than p_3.

- Cell too short.

The first point can be the result of leakage in the manifold 2, which lowers p_2 to ambient pressure, whereas the reason for the second point is a cell wheel of too small a dimension. Since the mixing zone can be developed up to one third or even more of the cell length (Hörler (1969)), usually the cell wheel length is dimensioned such that – with respect to the PWS rotational frequency – the mean value of the exhaust gas penetration at full load condition is approximately in the center of the cell in the field y.

Summarizing, stationary EGR can be avoided by:

- Increasing scavenging energy as much as possible.

- Adjusting the cell wheel length and the rotational speed of the PWS correctly to the expected exhaust gas volume flow.

- Ensuring that the connecting of the tubes from the channel 2 to the cylinders of the SI engine is airtight.

The criterion 1) can be reached with low leakage out of the cell wheel and with a generously designed and smoothly shaped tube 1, air filter, tube 4, and oxidation catalyst. The criterion 2) is satisfied if the PWS is correctly designed, whereas the criterion 3) depends on the tightness of the intake system.

Transient Exhaust Gas Recirculation

During a load step of the SI engine, when the GPV is rapidly shut, the pressure in the gas pocket drops for a short time, since the mass flowing through the GPV is smaller than the mass flowing through channel g into the PWS. This mass deficit in the gas pocket reduces not only the gas pocket pressure p_g, but also the pressures p_y and finally p_z. For the short time of the gas pocket pressure drop, the scavenging

pressure p_z can be insufficiently high to permit complete scavenging. For this short time *low pressure EGR* occurs and the engine torque drops due to the deficit of oxygen in the cylinder. Transient EGR is therefore caused by a substantial gas pocket pressure decrease while closing the GPV.

The pressure p_3 is the pressure "upstream" of the GPV. Therefore, the pressure p_3 rises whenever the GPV is closed. This leads to a higher pressure p_x. Due to the rising pressure p_x the mass flowing out of the gas pocket decreases which leads to an increasing gas pocket pressure after the gas pocket pressure drop. The scavenging process becomes complete again and finally engine torque increases.

This chapter pointed out the working principle of a pressure wave supercharger including the phenomenon of steady-state and transient exhaust gas recirculation which only can be explained by the existence of a mixing zone in the cell wheel. The following chapter describes the modeling of the pressure wave process including a mixing zone.

Chapter 3

Modeling of the Plant

This chapter describes in detail the modeling of the pressure wave supercharger although the model is based on the known linear one-dimensional gas dynamics. The reason is that the presented model approach is the result of developing and testing numerous models for best model accuracy. The decision which waves have to be taken into account and which can be neglected comes out of systematically testing the different models. The resulting pressure wave diagram is the one presented in this chapter. In order to point out every assumption, all the neglects, and the physically based model parameters, all equations of the model are documented.

The first section of this chapter explains the basic idea of dividing the system "PWS SI engine" into static and dynamic parts and shows the structure of the resulting model. It gives also reasons why the dynamics of the pressure wave supercharger can be neglected in this model approach. The second section derives the equations for the one-dimensional linear gas dynamics, used for modeling the pressure wave supercharger. The third section then describes in detail the modeling of the pressure wave supercharger. The modeling of the devices as SI engine, receiver, and throttle is explained in the last section.

In the following, some fixed expressions are used. The expression "channel" represents the cross-sectional area where the fluid flows into and out of the PWS. Thus, the "channel" has no volume. In contrast, the expression "manifold" is used for the tubes enclosing

the PWS. The volume of the "manifold" is given by the tube volume, for instance, from channel 2 to the throttle no. 2. The expression "gas side" defines the side of the cell where the exhaust gases flow into and out of the PWS. The expression "air side" represents the side of the cell where the ambient air flows into and the compressed air out of the PWS. The model of the entire system "PWS SI engine" is termed *PWS Engine Model*, whereas the main submodel of this simulation tool is the model of the PWS, called *PWS Model*.

3.1 Modeling Principles

The first subsection points out why the dynamics of the PWS may reasonably be neglected when the *PWS Model* is to be connected to an engine system model. As a result, the *PWS Engine Model* can be divided into submodels representing the static and dynamic characteristics of the system "PWS SI engine". The second subsection lists all these submodels and shows the structure of the resulting simulation tool. The third subsection then clarifies which states of the *PWS Engine Model* are inputs and which are outputs of the *PWS Model*.

3.1.1 Dynamics of the Pressure Wave Supercharger

The dynamics of a PWS are determined by the time needed to build a new pressure wave diagram which satisfies the actual thermodynamic boundary condition (pressure, temperature) in the manifolds next to the PWS, see Fig. 3.1. Since these dynamics are fast compared to those of the filling-emptying process of the manifolds (receiver dynamic) and even much faster than the dynamics of the walls (thermal mass), the former dynamics can be neglected. The typical time constant of the PWS is on the order of 1 ms, whereas the time constant of the manifolds is on the order of 100 ms, compare Amstutz (1991), Mayer (1988), and Wallace and Aldis. The thermal mass of the entire system (engine body, exhaust tubes, PWS body) stores exhaust gas enthalpy. This mass has to be heated up during a load step. The time until the wall temperature has reached its new steady-state value, when the wall temperature is in balance with the fluid temperature in the tube and with ambient temperature, is in the range between 6 ... 12 minutes, depending on the engine.

The time constant of the PWS is defined by the length of the cell wheel divided by the speed of sound for the primary compression process $s1$:

$$\tau_{\text{pws}} \simeq \frac{l_{\text{cell}}}{\sqrt{\kappa R T_{1\text{s}}}} \tag{3.1}$$

The dynamics of the PWS are approximately 100 times faster than those of the receiver, which in turn are at least 300 times faster than

the dynamics of the wall mass:

$$\tau_{\mathrm{pws}} \ll \tau_{\mathrm{receiver}} \tag{3.2}$$

$$\tau_{\mathrm{receiver}} \ll \tau_{\mathrm{thermal\,mass}} \tag{3.3}$$

Thus, the dynamics of the PWS can be neglected since the dynamics of the thermodynamic states in the manifolds enclosing the PWS are much slower. The PWS is modeled as a static device whose outputs are mass and enthalpy flows ("generalized" throttle).
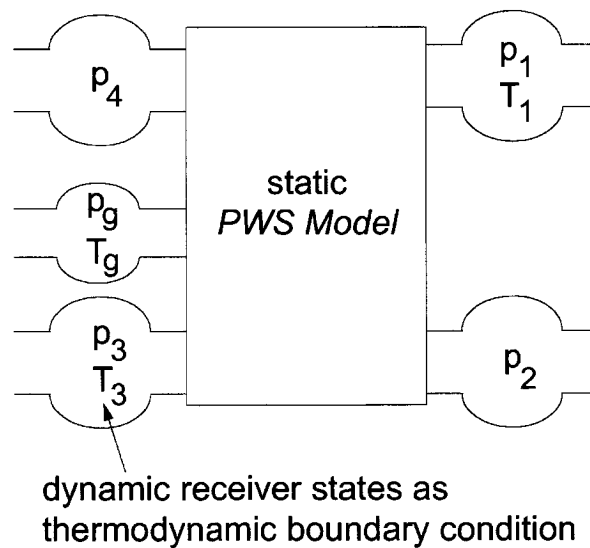

Figure 3.1: Thermodynamic boundary condition in the manifolds (receivers) next to the PWS representing the relevant dynamics; PWS modeled as a "generalized" throttle (static block)

3.1.2   Dynamic and Static Parts of the *PWS Engine Model*

The pressure wave supercharger is modeled as a static function neglecting the fast dynamics of building a new wave diagram. The SI engine is modeled as a static part of the system "PWS SI engine" as well, neglecting any delay of the combustion process. Both the throttles and the catalysts are described by static functions. The fast

dynamics of the system are determined by the mass and enthalpy storage of the fluid in the receivers, whereas the slow dynamics are caused by the energy storage in the wall mass of the exhaust system.
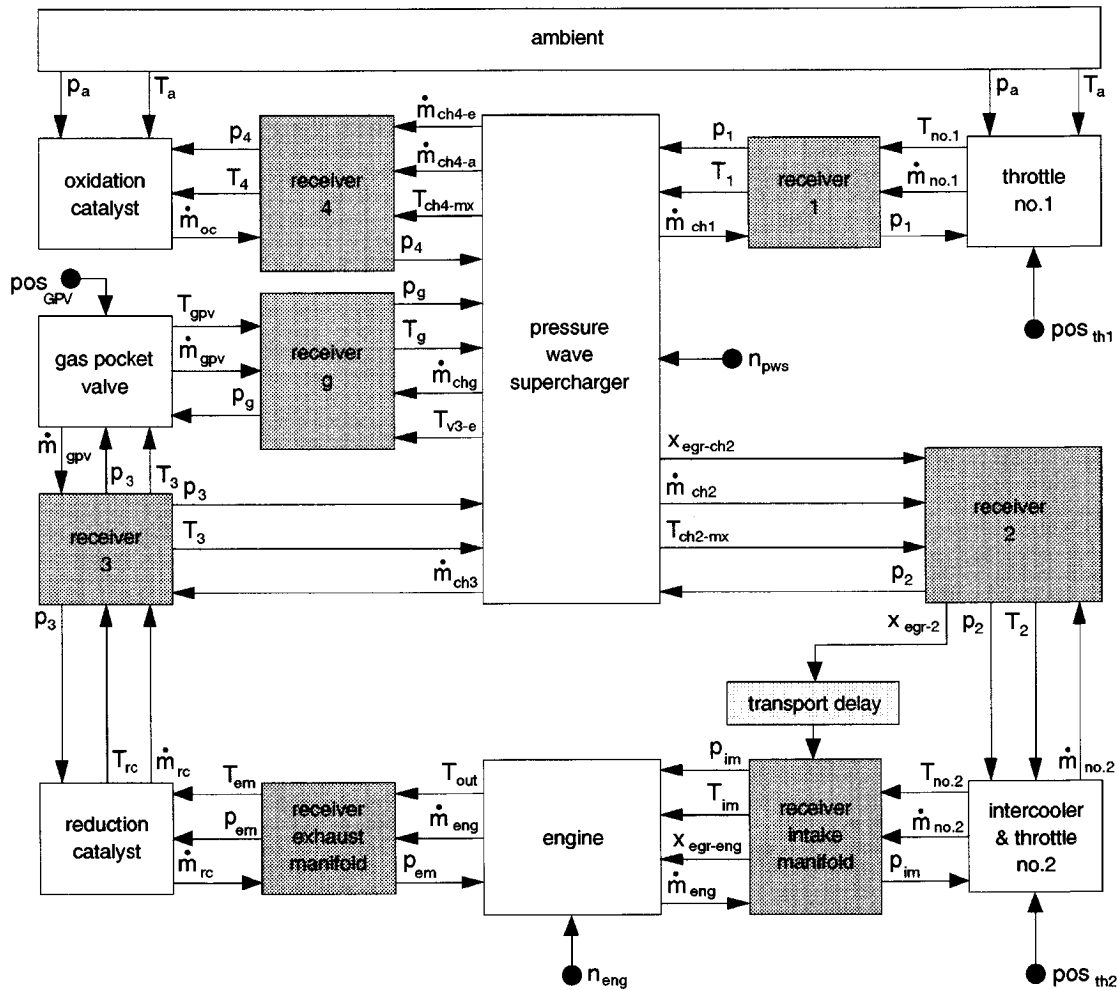
Figure 3.2: Signal flow chart of the dynamic simulation tool *PWS Engine Model*; dynamic parts (receiver) shaded; static parts white; simulation tool inputs: n_{eng}, n_{pws}, pos_{th1}, pos_{th2}, and pos_{GPV}

The simulation tool *PWS Engine Model* allows to simulate the transient behavior of the system "PWS SI engine". The details of how all submodels are interconnected, and of which states are input and output of which submodels, are illustrated in Fig. 3.2. The additional block *transport delay* represents the transportation time of the EGR rate from channel 2 to the cylinder. Summarizing, the

PWS Engine Model is characterized by:

- the following dynamic parts:
  - receiver 1   :   manifold between throttle no. 1 and channel 1
  - receiver 2   :   manifold between channel 2 and throttle no. 2
  - receiver im   :   manifold between throttle no. 2 and SI engine (intake manifold)
  - receiver em   :   manifold between SI engine and reduction catalyst (exhaust manifold)
  - receiver 3   :   manifold between reduction catalyst and the two next devices as channel 3 and GPV
  - receiver g   :   manifold between GPV and channel g
  - receiver 4   :   manifold between channel 4 and oxidation catalyst

- the following static parts:
  - pressure wave supercharger: *PWS Model*
  - SI engine
  - transportation time from channel 2 to cylinder: transport delay
  - throttle no. 1
  - throttle no. 2
  - intercooler
  - reduction catalyst
  - gas pocket valve (GPV)
  - oxidation catalyst

- the following inputs:
  - position of throttle no. 1   : pos_{th1}
  - position of throttle no. 2   : pos_{th2}
  - position of gas pocket valve   : pos_{GPV}
  - rotational speed of the PWS   : n_{pws}
  - engine speed   : n_{eng}

3.1.3 Inputs and Outputs of the *PWS Model*

The calculation of the output values of the *PWS Model* is divided into the parts *high pressure part*, *leakage*, and *low pressure part*, see Fig. 3.3. The transient thermodynamic boundary condition in the manifolds next to the PWS (see Fig. 3.1) are the inputs for the *PWS Model*.
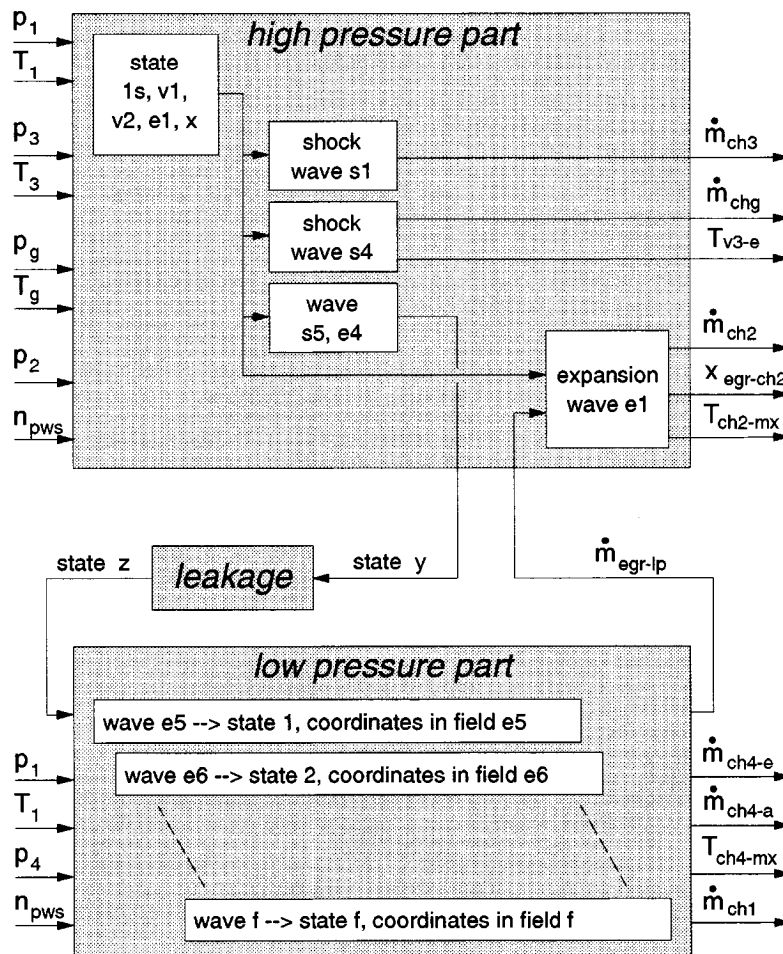
Figure 3.3: Signal flow chart of the *PWS Model*: thermodynamic condition in the receivers next to the PWS and n_{pws} as model inputs, mass and enthalpy flows as model outputs

3.2   Gas Dynamics

Whereas the first subsection derives the algebraic equations for the one-dimensional, linear gas dynamics, the second subsection explains the differences between compression and expansion processes.

3.2.1   One-Dimensional, Linear Gas Dynamics

The gas dynamics used in this model are based on the linear wave theory. The linear wave theory is defined by the assumption that the characteristics are straight lines over the complete *x-t-area* (Sauer (1960), Zierep (1963)). The total differential of the specific entropy *s* as a function of the position *x* and the time *t* in the *x-t-area* is:

$$\frac{ds}{dt} = \frac{\delta s}{\delta t} + u\frac{\delta s}{\delta x} = 0 \tag{3.4}$$

In contrast to the non-linear wave theory, the linear wave theory allows to calculate the next state in the *x-t-area* without any iteration since the state of interest only depends on the given states and the constant process parameter (Eq. 3.4). This fact helps to reduce computation time in order to simulate transient phenomena.

Assuming a perfect gas behavior the basic equations for the linear, one-dimensional gas dynamics follow from mass, energy, and impulse balances which are formulated for a stationary shock wave in a narrow, adiabatic tube (Fig. 3.4, Endres (1985) and Gyarmathy (1983)). The fact that the two media always have to be in contact – same velocity and same pressure – furnishes the additional *contact conditions*. These six linear independent equations can be solved for the variables of interest, see Eq. 3.13.

In order to formulate the balance equations for a stationary shock wave, the following substitutions are made:

$$\hat{u}_1 := w - u_1 \tag{3.5}$$

$$\hat{u}_2 := w \tag{3.6}$$
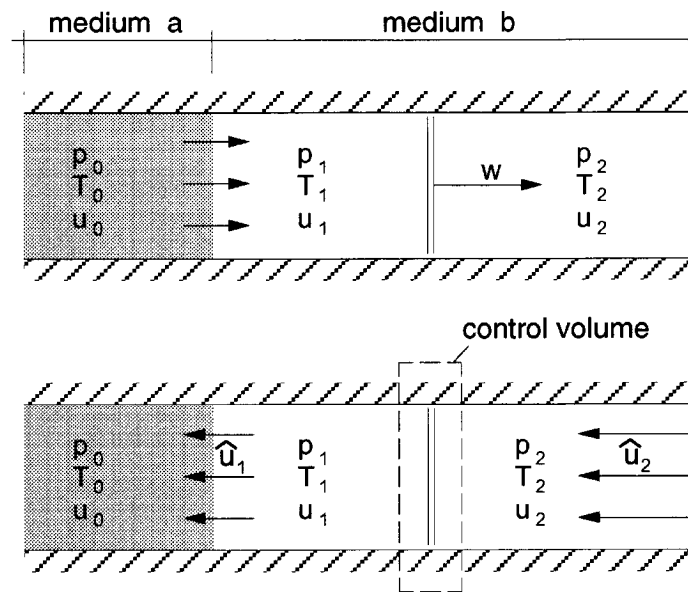
Figure 3.4: Above: one-dimensional shock wave in a narrow, adiabatic tube; Below: stationary shock wave in the control volume

The set of the six linear independent equations is:

mass balance:

$$\rho_1 \hat{u}_1 = \rho_2 \hat{u}_2 \qquad (3.7)$$

impulse balance:

$$p_1 + \rho_1 \hat{u}_1^2 = p_2 + \rho_2 \hat{u}_2^2 \qquad (3.8)$$

energy balance:

$$c_\mathrm{p} T_1 + \frac{\hat{u}_1^2}{2} = c_\mathrm{p} T_2 + \frac{\hat{u}_2^2}{2} \qquad (3.9)$$

perfect gas behavior:

$$p_1 = \rho_1 R T_1 \qquad (3.10)$$

$$c_\mathrm{p} = constant$$

$$c_\mathrm{v} = constant$$

contact conditions:

$$u_0 = u_1 \qquad (3.11)$$

$$p_0 = p_1 \qquad (3.12)$$

given states:

$$p_0 \, , \; T_0 \, , \; \rho_0 \, , \; p_2 \, , \; T_2 \, , \; \rho_2 \, , \; u_2$$

unknown states:

$$p_1 \, , \; T_1 \, , \; \rho_1 \, , \; u_1 \, , \; u_0 \, , \; w$$

After some transformations the relevant equations for the one-dimensional shock wave in the narrow, adiabatic tube read as follows:

pressure ratio over the shock:

$$\pi_\mathrm{s} = \frac{p_0}{p_2} \qquad (3.13)$$

speed of sound in 2:

$$a_2 = \sqrt{\kappa R T_2} \qquad (3.14)$$

fluid velocity in 1:

$$u_1 = a_2 \sqrt{\frac{2}{\kappa}} \; \frac{\pi_\mathrm{s} - 1}{\sqrt{\pi_\mathrm{s}\left(\kappa + 1\right) + \kappa - 1}} \qquad (3.15)$$

shock velocity:

$$w = \sqrt{\frac{R T_2}{2}} \sqrt{\pi_\mathrm{s}\left(\kappa + 1\right) + \kappa - 1} \qquad (3.16)$$

fluid temperature in 1:

$$T_1 = T_2 \, \pi_\mathrm{s} \, \frac{\pi_\mathrm{s}\left(\kappa - 1\right) + \kappa + 1}{\pi_\mathrm{s}\left(\kappa + 1\right) + \kappa - 1} \qquad (3.17)$$

The unknown states p_1 and u_0 follow from the contact condition, the state ρ_1 then results from the perfect gas behavior.

3.2.2 Compression and Expansion Processes

When a cell of the PWS opens to a tube (manifold), the following process is either a compression or an expansion process, depending on the pressure ratio given by the pressure in the tube divided by the pressure in the cell:

- **Shock wave**: If the pressure ratio is bigger than 1, the fluid in the tube flows into the cell. Simultaneously, a faster shock wave propagates through the fluid in the cell. The shock wave compresses the fluid in the cell up to the static pressure of the inflowing fluid. Since the pressure rises unsteadily over the shock (Jenny (1949)), the entropy has to increase over the shock. Therefore, the state of the fluid evolves polytropically in a compression process (Hörler (1969), Baehr (1992)).

- **Expansion wave**: If the pressure ratio is smaller than 1, the fluid flows out of the cell towards the tube while expanding to the pressure in the tube. In contrast to the compression wave, the pressure decrease across the expansion wave occurs over a non-negligible distance in the x dimension. The states do not change abruptly in an expansion process. This is the reason why expansion processes are nearly isentropic (Baehr (1992)).

The following modeling part of the PWS distinguishes between compression and expansion process by:

1. **Process parameter**: The process parameter *adiabatic compression efficiency* η_c defines the change of entropy for compression processes. As explained above, an *adiabatic expansion efficiency* is not necessary since expansion processes are nearly isentropic. In the model approach presented expansion processes are assumed to be completely isentropic.

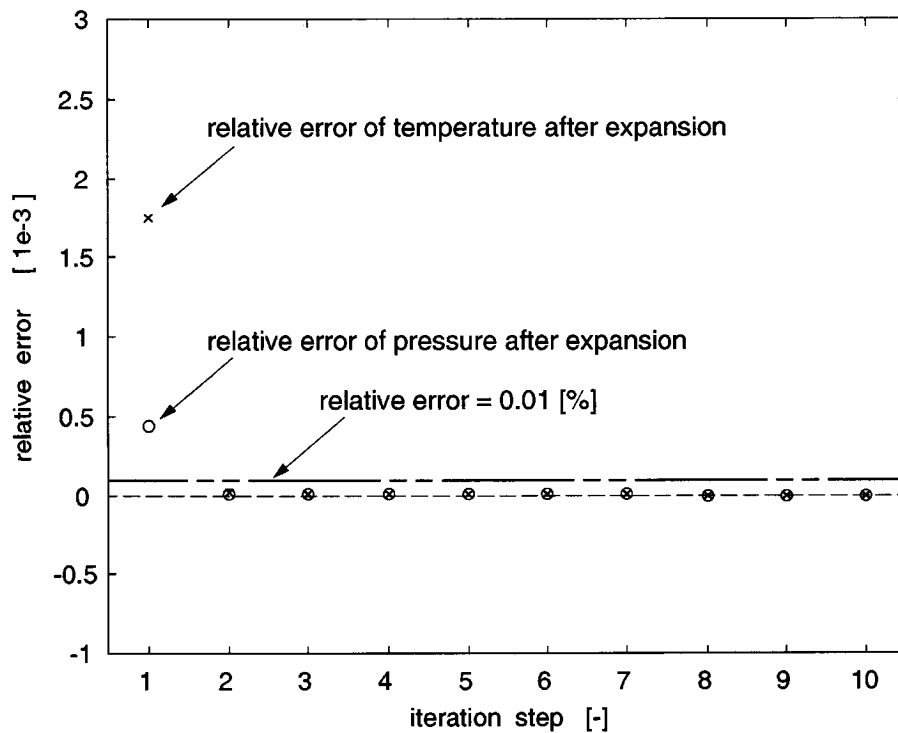2. **Relevant temperature for speed of sound**:

    2.1 In the case of a compression wave: The temperature which defines the speed of sound for compression processes is the fluid temperature of the not yet compressed medium:

$$T_{\text{sound−compression}} = T_2 \tag{3.18}$$

2.2 In the case of an expansion wave: The relevant temperature that defines the speed of sound for expansion processes is in a first approximation the mean value of the temperatures before and after the expansion wave:

$$T_{\text{sound-expansion}} \approx \frac{T_1 + T_2}{2} \tag{3.19}$$

If the pressure of the expanded fluid is given, the expanded temperature can be calculated by using Eq. 3.17. Then, the relevant temperature for the speed of sound can be derived (Eq. 3.19).

Figure 3.5: Decreasing relative error of the state after expansion as a function of iteration steps

If the fluid velocity of the expanded fluid is given, e.g., the boundary condition *wall*, the temperature for the speed of sound has to be estimated in a first step since the pressure after expansion in unknown:

$$T_{\text{sound-expansion-1}} = T_1 \tag{3.20}$$

The estimated temperature for the speed of sound allows to derive a first value of the state (pressure and temperature) after expansion.

Using this first set of values a new relevant temperature for the speed of sound can be derived:

$$T_{\text{sound}-\text{expansion}-2} = \frac{T_1 + T_{2-\text{first}}}{2} \qquad (3.21)$$

The second value of the temperature for the speed of sound leads to a temperature and pressure of the expanded fluid with an error smaller than 0.01% compared with the value after 10 iteration steps, see Fig. 3.5. The reason is that the temperature for the speed of sound in Eq. 3.15 only slightly affects the value of the resulting pressure after expansion. Therefore, the iteration already stops after the second step:

$$T_{\text{sound}-\text{expansion}} = T_{\text{sound}-\text{expansion}-2} \qquad (3.22)$$

Using the second value of the temperature as the relevant temperature for the speed of sound together with the given boundary condition after expansion, the new state of the expanded fluid can be computed by using the algebraic relations listed in Eq. 3.13 – 3.17.

3.3   Model of Pressure Wave Supercharger

The whole pressure wave process is divided into the three parts:

- *High Pressure Part*

- *Leakage Phenomenon*

- *Low Pressure Part.*

The *High Pressure Part* (see Sect. 3.3.1) and the *Low Pressure Part* (see Sect. 3.3.3) together predict the model outputs as mass and enthalpy flows including EGR in the channels. The Section 3.3.2 entitled *"Leakage Phenomenon"* describes the model for the leakage mass flow out of the cell wheel into the channels on the low pressure side.

According to Piechna and Lisewski (1998), and Piechna (1998a), both the fluid velocity and the shock wave front are fully developed approximately after the length of one cell diameter in the sense that the fluid velocity is nearly one-dimensional and the states change in a thin zone in the flat shock wave. This allows to assume the flow to be one-dimensional as well as the state change in the shock wave to occur abruptly. Therefore, the gas dynamics used in this model approach are based on the linear, one-dimensional wave theory described in Sec. 3.2.

3.3.1   High Pressure Part

The calculation of the *High Pressure Part* starts with the opening of channel 3 (state $1s$) and ends with the derivation of the state after channel g has closed (state y), see Fig. 3.6. The modeling assumes the simplified wave process as depicted in Fig. 3.6, where, e.g., wave reflections at the contact front are neglected.

The modeling of the *High Pressure Part* includes the following steps:

1. Assume the fluid state in the field $1s$.

2. Compute the fluid states in all observed fields, the wave velocities, and the coordinates of the wave diagram, starting with state $1s$ and ending with state y.

3. Calculate the mass flow of the exhaust gases flowing through channel 3 into the PWS; using this mass flow as the mass flowing out of manifold 3, the mass and energy balances in manifold 3 can be solved.

4. Compute the mass flow of the exhaust gases, which are recirculated directly from channel 3 into channel 2.

5. Calculate the mass and enthalpy flows in channel 2; using these two flows as the mass and enthalpy flowing into manifold 2, the mass and energy balances in manifold 2 can be solved.

6. Calculate the mass flow of exhaust gases flowing through channel g into the PWS; using this mass flow as the mass flowing out of manifold g, the mass and energy balances in manifold g can be solved.

7. Pass the derived values at state y on to the submodel *leakage*, see Fig. 3.3.

An additional result of the submodel *high pressure part* is the rotational speed of the PWS where the ratio of p_2/p_3 is at its maximum value. This rotational speed of the PWS is called *ideal* rotational speed of the PWS.

State 1s

Leakage losses out of the cell during the rotation from the point where channel 1 closes to the point where channel 3 opens can be excluded due to $p_1 \approx p_a$. If any pressure losses during the inflow process through channel 1 are neglected also, the pressure in the cell before channel 3 opens is:

$$p_{1s} = p_1 \tag{3.23}$$

The temperature in the cell at state 1s is different at the gas and at the air side. At the air side, in a first approximation the temperature is equal to ambient temperature since the heat exchange with the PWS body is negligible due to the fast rotational speed of the PWS. At the gas side, the temperature is significantly higher than ambient temperature (temperature around 180 °C, see Fig. 3.7). This results from the hot PWS body on on the gas side and from the *natural EGR*
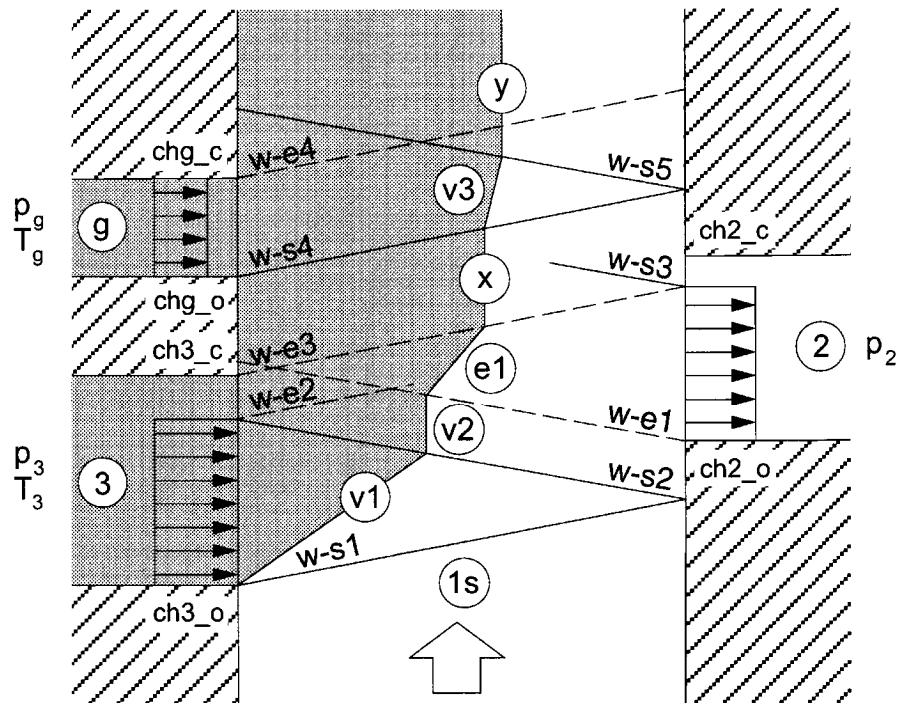
Figure 3.6: Model of simplified wave diagram of the *High Pressure Part*
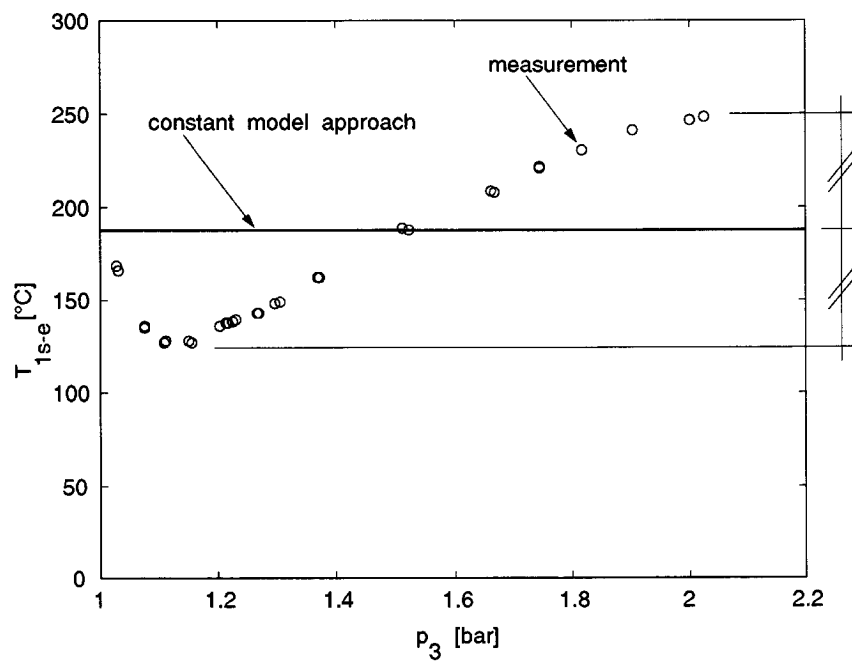
Figure 3.7: Fluid temperature in the cell at location 1s on the gas side

which is caused by the incomplete scavenging of 0.5 ... 1.0% of the exhaust gases. The measured temperature T_{1s-e} rises with increasing engine load due to the rising exhaust gas enthalpy and increases at lowest engine loads as well due to the worse scavenging, see Fig. 3.7.

The temperature at state $1s$ at the gas side does hardly influence the temperature of the compressed fresh air in channel 2 because the part of the fluid in the cell which is close to the gas side with the temperature T_{1s-e} does not leave the cell towards channel 2 after it is compressed to state $1s$ but remains in the cell wheel.

By contrast, the influence of the higher temperature at the gas side compared to the one of the air side cannot be neglected for the mean speed of sound of the shock wave $s1$.

Therefore, the state $1s$ is assumed to be as follows:

$$T_{1s-a} = T_1 \tag{3.24}$$

$$T_{1s-e} = T_1 + \Delta T_{1s-e} \tag{3.25}$$

Inflow Process Through Channel 3

When the cell reaches channel 3, the pressure ratio $p_3/p_{1s} > 1$ causes the *primary* pressure wave $s1$. It accelerates the exhaust gases into the cell and compresses the fresh air to state $v1$. The process parameter η_c takes into account the main losses such as friction when the fluid flows from the manifold into the cell as well as the polytropic state change of the fluid during the compression process.

Compression efficiency: The compression efficiency η_c is assumed to be a function of the pressure ratio over a compression wave (see Fig. 3.8) since a higher compression ratio causes a more polytropic state evolution:

$$\eta_c = f(\pi) \tag{3.26}$$

Notice that the compression efficiency describes the losses for all observed compression waves as a function of the pressure ratio of each individual compression wave. The compression efficiency for the actual pressure ratio over the shock i leads to the polytropic exponent n for the process i and the medium j:

$$n_{i-j} = \frac{\eta_c \kappa_j}{\eta_c \kappa_j - \kappa_j + 1} \tag{3.27}$$

The temperature of the compressed medium j is given by Eq. 3.27. However, in order to calculate the fluid velocity of the two adjoining media j and k that are standing in contact with each other, the value of the polytropic exponent is a mean value due to the *contact conditions*:

$$n_{i-m} = \frac{n_{i-j} + n_{i-k}}{2} \tag{3.28}$$
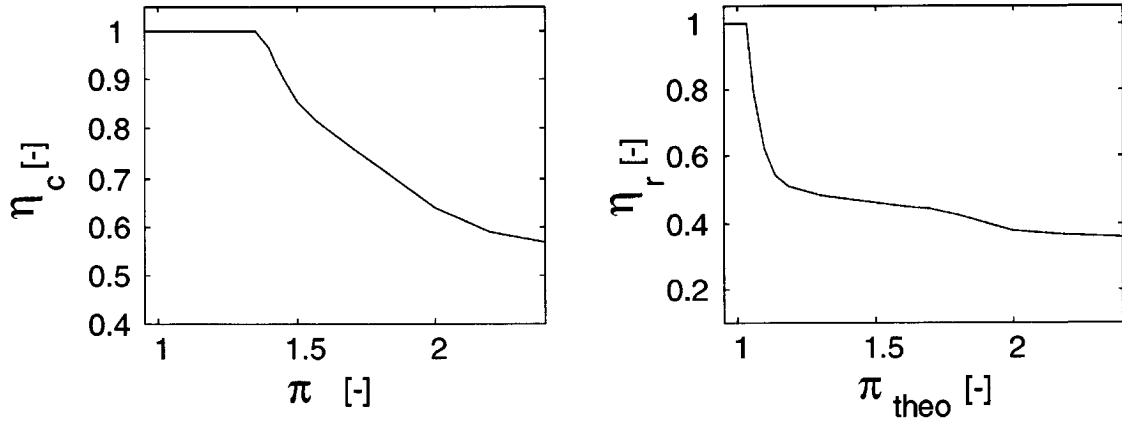
Figure 3.8: Model parameters η_c and η_r derived from identification

The pressure ratio π_{s1} over the pressure wave $s1$ is given by the thermodynamic boundary condition:

$$\pi_{s1} = \frac{p_{v1}}{p_{1s}} = \frac{p_3}{p_{1s}} \tag{3.29}$$

Since the fluid velocity in the cell at state $1s$ is 0, the relative and absolute fluid velocities in the field $v1$ are identical:

$$u_{v1} = u_{ch3} = \sqrt{2RT_{1s-m}} \frac{\pi_{s1} - 1}{\sqrt{\pi_{s1}(n_{s1-m} + 1) + n_{s1-m} - 1}} \tag{3.30}$$

with the relevant temperature for the speed of sound

$$T_{1s-m} = \frac{T_{1s-a} + T_{1s-e}}{2} \tag{3.31}$$

and the polytropic exponent, which is a function not only of the compression efficiency but also of the material characteristics

$$n_{1s-m} = \frac{n_{1s-a} + n_{1s-e}}{2} \tag{3.32}$$

Now, the exhaust gas mass flow in channel 3 can be calculated:

$$\dot{m}_{ch3} = \frac{p_{v1}}{RT_{v1-e}} \, A_{ch3-eff} \, u_{ch3} \qquad (3.33)$$

where the temperature is given by the thermodynamic boundary condition

$$T_{v1-e} = T_3 \qquad (3.34)$$

and

$$A_{ch3-eff} = f(geometry, n_{pws}) \qquad (3.35)$$

The channel area, where the fluid flows with constant velocity u_{ch3} into the cell, depends not only on the channel geometry but also on the actual rotational speed of the PWS. When the reflected shock wave $s2$ hits the open channel 3, it is reflected as the expansion wave $e2$. The fluid in the cell expands from p_{v2} to the lower pressure p_3 and accelerates the exhaust gases in the cell towards channel 3. The resulting velocity in a first approximation is 0. The fluid velocity is 0 from the point where the wave $s2$ meets channel 3 until channel 3 closes, see Fig. 3.6. Hence, the exhaust enthalpy flow through channel 3 is reduced, see Berchtold (1961). This effect is taken into account in Eq. 3.35.

Due to the contact conditions the primary compressed fresh air has the same pressure and velocity as the exhaust gases flowing into the cell through channel 3. The temperature of the primary compressed fresh air becomes:

$$T_{v1-a} = T_{1s-a} \, \pi_{s1} \, \frac{\pi_{s1}\,(n_{s1-a} - 1) + n_{s1-a} + 1}{\pi_{s1}\,(n_{s1-a} + 1) + n_{s1-a} - 1} \qquad (3.36)$$

Ideal Rotational Speed of the PWS

If the focus is on the maximum of the pressure p_2 for a given state in channel 3, i.e., p_3, T_3, then the rotational speed of the PWS has to be chosen the way that the shock wave $s2$ has to meet the gas side exactly when channel 3 closes:

1. **Condition for ideal rotational speed of the PWS**: The rotational speed of the PWS is ideal when the compression wave $s2$

meets the gas side exactly at the point where channel 3 closes. In this case the fluid velocity in the whole channel 3 is $u_{ch3} \neq 0$.

2. **Impact of ideal rotational speed of the PWS**: When the rotational speed of the PWS is ideal the enthalpy flow through channel 3 and therefore the charging energy are at the maximum. As a result the ratio p_2/p_3 is at its maximum (Piechna (1998b)).

The condition for the ideal rotational speed of the PWS on the one hand depends on the thermodynamic boundary condition which influences all processes from state $1s$ to state $v2$. On the other hand, it depends on the geometry of the PWS:

$$n_{\text{pws}-\text{ideal}} = f\left(p_{1s}, T_{1s}, p_3, T_3, l_{ch3}, l_{cell}\right) \qquad (3.37)$$

The changes of state $1s$ are negligible compared to those of state 3. Additionally, the influence of T_3 on $n_{\text{pws}-\text{ideal}}$ is of second order compared to the influence of p_3. Thus, for a given PWS geometry, equation 3.37 can be simplified as follows:

$$n_{\text{pws}-\text{ideal}-\text{simplified}} = f\left(p_3\right) \qquad (3.38)$$

Basically, the relation found in Eq. 3.38 allows to adjust the rotational speed of the PWS to the actual thermodynamic boundary condition in order to guarantee a maximum pressure ratio p_2/p_3. To avoid the problem of measuring the pressure p_3, it is possible to use the inverse of the measured relation:

$$p_2 = f\left(p_3\right)$$

and to measure the actual p_2. Due to the fast dynamics of the PWS the estimated value of p_3 is close to the actual value.

State $v2$

After the primary shock wave $s1$ reaches the air side, the fluid in the whole cell is compressed to:

$$p_{v1} \equiv p_3$$

and flows with the velocity:

$$u_{v1} \equiv u_{ch3}$$

towards the wall of the air side. The boundary condition *wall* at the air side demands zero velocity, see Croes (1979). In order to satisfy the latter condition, the primary shock wave $s1$ is reflected as a shock wave again. This shock wave is called *secondary* shock wave $s2$. It decelerates the fluid to zero velocity and lets the pressure increase up to:

$$p_{v2-\text{theo}} = \pi_{v2-\text{theo}}\, p_{v1} \qquad (3.39)$$

The theoretical pressure in Eq. 3.39 is lowered by leakage losses out of the cell through the gap between cell wheel and housing. Taking these losses into account, the pressure in the cell becomes p_{v2} and the fluid velocity is zero:

$$u_{v2} \equiv 0$$

Reflection efficiency: The leakage losses mentioned above can be described by the model parameter *efficiency for shock reflection*, η_r. It is assumed to be a function of the theoretical pressure ratio for a shock reflection, see Fig. 3.8:

$$\eta_{r-i} = f\left(\pi_{\text{theo}-i}\right) \qquad (3.40)$$

Notice that the reflection efficiency describes the losses for all observed reflected compression waves as a function of the theoretical pressure ratio of each reflected compression wave. The reflection efficiency for the actual theoretical pressure ratio over the shock i leads to the real pressure ratio:

$$\pi_i = \eta_{r-i}\left(\pi_{i-\text{theo}} - 1\right) + 1 \qquad (3.41)$$

Fitting the reflection efficiency as a function of the theoretical pressure ratio allows to compute the state after a shock reflection without iteration since the theoretical pressure can be derived without using any model parameter.

Considering the boundary condition *wall* (zero velocity) at the air side:

$$u_{v2-\text{rel}} \equiv |u_{v1}|$$

$$= \sqrt{2RT_{v1}}\ \frac{\pi_{s2-\text{theo}} - 1}{\sqrt{\pi_{s2-\text{theo}}\left(n_{s2-m} + 1\right) + n_{s2-m} - 1}} \qquad (3.42)$$

and using the known function for the reflection efficiency:

$$\pi_{s2} = \eta_{r-s2} \left(\pi_{s2-theo} - 1\right) + 1 \tag{3.43}$$

leads to the state in the field $v2$:

$$p_{v2} = \pi_{s2}\, p_{v1} \tag{3.44}$$

$$u_{v2} \equiv 0 \tag{3.45}$$

$$T_{v2-a} = T_{v1-a}\, \pi_{s2}\, \frac{\pi_{s2}\left(n_{s2-a} - 1\right) + n_{s2-a} + 1}{\pi_{s2}\left(n_{s2-a} + 1\right) + n_{s2-a} - 1} \tag{3.46}$$

$$T_{v2-e} = T_{v1-e}\, \pi_{s2}\, \frac{\pi_{s2}\left(n_{s2-e} - 1\right) + n_{s2-e} + 1}{\pi_{s2}\left(n_{s2-e} + 1\right) + n_{s2-e} - 1} \tag{3.47}$$

High Pressure EGR

The exhaust gases which are recirculated directly from channel 3 into channel 2 because one part of the mixing zone flows into channel 2 is called in the following *high pressure EGR*. The following estimation of the time which is needed to develop a mixing zone of one cell length shows that *high pressure EGR* is a priori possible.

The available time for *high pressure EGR* is:

$$\Delta t_{available} = t_{ch2-closes} - t_{ch3-opens} \sim (2 \ldots 6) \cdot 10^{-4}\,[s] \tag{3.48}$$

The time necessary to build a mixing zone over one cell length can be derived as follows:

- Reynolds number of the flow in a cell:

$$Re_d = \frac{\bar{u}_{v1} d_{cell}}{\nu} \sim (1 \ldots 3) \cdot 10^4\,[-] \tag{3.49}$$

- diffusion coefficient for turbulent flow (Boulouchos (1994)):

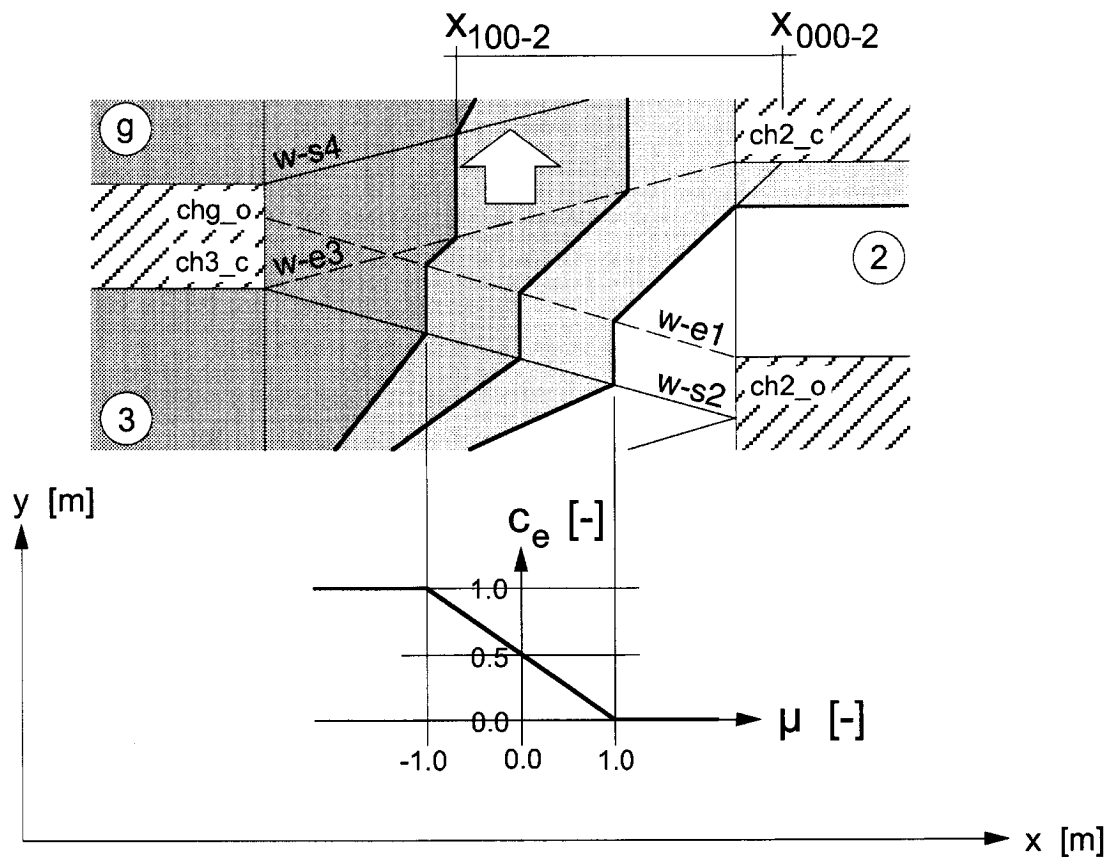$$D \sim 1.2 \cdot 10^{-9} \cdot \frac{T^{5/3}}{p} \sim (4 \ldots 8) \cdot 10^{-5}\,[m^2/s] \tag{3.50}$$

(T in [Kelvin], p in [bar])

- time needed for the diffusion over one cell length:

$$t_{\text{diff}} \sim \frac{l_{cell}^2}{D} \sim (1 \dots 2) \cdot 10^{-4} \, [s] \qquad (3.51)$$

Thus, *high pressure EGR* is possible due to:

$$\Delta t_{\text{available}} \sim t_{\text{diff}} \qquad (3.52)$$

Figure 3.9: Model for EGR directly recirculated from channel 3 into channel 2 due to the mixing zone at the location where channel 2 closes; mixing zone with linear exhaust gas fraction profile

There are two reasons for *high pressure EGR* occurring:

- Rotational speed of the PWS too slow.

- Cell wheel too small.

In order to determine the *high pressure EGR* mass flow, it is necessary to:

1. Assume an exhaust gas fraction profile over the mixing zone.

2. Calculate the coordinates of the mixing zone at the place channel 2 closes, see Fig. 3.9.

When two species are mixed, two exhaust gas fraction profiles are basically possible, a profile which can be described by the function tangens hyperbolicus and a profile which can be described by a linear function:

$$
\begin{aligned}
\text{"tangens hyperbolicus"} &: c_\text{e}(\mu) = \frac{\tanh(2) - \tanh(2\mu)}{2\tanh(2)} \\
\text{"linear"} &: c_\text{e}(\mu) = \frac{1}{2}(1 - \mu)
\end{aligned}
\tag{3.53}
$$

with:

$$
\int\limits_{-1}^{+1} c_\text{e}(\mu) d\mu \equiv 1
\tag{3.54}
$$

This allows the derivation of a mean fraction between a higher and lower integration limit independently of the absolute length of the mixing zone on the x–axis, see Fig. 3.10.

Although the tangens hyperbolicus profile is the usual assumption for the mixing zone of two species, a linear profile will be tested by identification also, since the impact of the overlapping of several mixing zones in the cell wheel on the EGR mass flow is not clear. Therefore, only the model validation will allow to decide which profile function best explains the measured data. The criterion is the variance of the identified mixing zone length. The profile function where the variance is smaller will be chosen for the validation of the *PWS Model*.

The effect of the centripetal acceleration on the contact front (Hörler (1969)) is neglected since the distance of the sloping surface in the x-dimension is smaller than the expected mixing zone length.
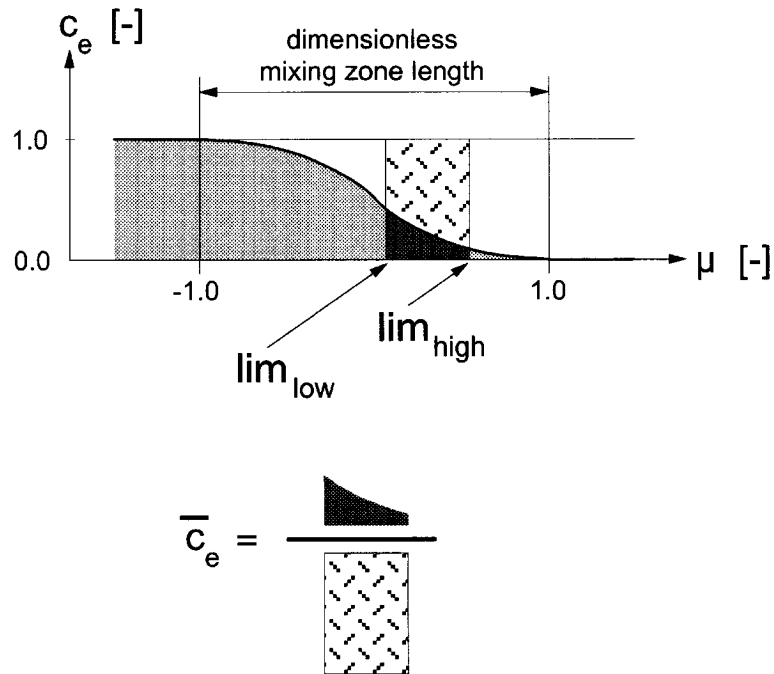
Figure 3.10: Derivation of the mean exhaust gas fraction from the exhaust gas fraction profile and the integration limits, case "tangens hyperbolicus" profile
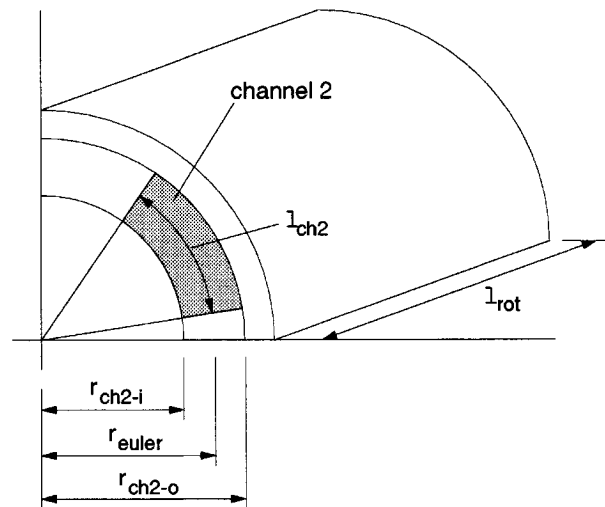
Figure 3.11: Nomenclature of the PWS body geometry: inner, outer, and "euler" radius, length of open channel at "euler" radius, cell wheel length

Also the influence of flow characteristics (not exactly one-dimensional, Piechna (1999)) on the contact front and therefore on the mixing zone are not taken into account because their impact on the EGR mass flow is of second order compared to the one of the mixing zone.

Using the geometrical data of the place where channel 2 closes, see Fig. 3.9, 3.10, and 3.11, the mean fraction of the directly recirculated exhaust gases and finally its mass flow can be derived:

- dimensionless integration limits on the μ-axis for the exhaust gases recirculated directly in the *high pressure part* (see Fig. 3.10):

$$lim_{\text{e-high-hp}} = 1.0 \tag{3.55}$$

$$lim_{\text{e-low-hp}} = lim_{\text{e-high-hp}} - \frac{x_{000-2} - x_{\text{ch2-c}}}{|x_{100-2} - x_{000-2}|/2} \tag{3.56}$$

- mean fraction of the *high pressure EGR* (see Fig. 3.10):

$$\bar{c}_{\text{e-hp}} = \frac{1}{lim_{\text{e-high-hp}} - lim_{\text{e-low-hp}}} \int_{lim_{\text{e-low-hp}}}^{lim_{\text{e-high-hp}}} c_{\text{e}}(\mu)d\mu \tag{3.57}$$

- mass flow of *high pressure EGR*:

$$\dot{m}_{\text{egr-hp}} = \bar{c}_{\text{e-hp}} \left(x_{000-2} - x_{\text{ch2\_c}}\right) \cdot$$
$$\frac{p_2}{RT_{\text{e1-e}}} \frac{n_{\text{pws}}}{60} \pi \left(r_{\text{ch2-o}}^2 - r_{\text{ch2-i}}^2\right) \tag{3.58}$$

Outflow Process Through Channel 2

In the field $e1$ the pressure is given by the pressure in manifold 2. Thus, when channel 2 opens, the fluid at state $v2$ expands to state $e1$ due to $p_2 < p_{v2}$. The expansion wave $e1$ accelerates the fluid in the cell towards channel 2. The temperature of the fluid (for air and for exhaust gas) and the fluid velocity in field $e1$ are:

$$T_{\text{e1-a}} = T_{\text{v2-a}}/\left(\pi_{\text{e1}} \frac{\pi_{\text{e1}}(\kappa_{\text{a}} - 1) + \kappa_{\text{a}} + 1}{\pi_{\text{e1}}(\kappa_{\text{a}} + 1) + \kappa_{\text{a}} - 1}\right) \tag{3.59}$$

$$T_{\text{e1-e}} = T_{\text{v2-e}}/\left(\pi_{\text{e1}} \frac{\pi_{\text{e1}}(\kappa_{\text{e}} - 1) + \kappa_{\text{e}} + 1}{\pi_{\text{e1}}(\kappa_{\text{e}} + 1) + \kappa_{\text{e}} - 1}\right) \tag{3.60}$$

$$u_{e1} = u_{ch2} = \sqrt{2RT_{e1-m}} \frac{\pi_{e1} - 1}{\sqrt{\pi_{e1}\left(\kappa_m + 1\right) + \kappa_m - 1}} \qquad (3.61)$$

with the pressure ratio π_{e1}, which is given by the calculated pressure in the field $v2$ and the thermodynamic boundary condition in channel 2

$$\pi_{e1} = \frac{p_{v2}}{p_2} \qquad (3.62)$$

and T_{e1-a-m} as the average temperature over the wave $e1$, which is taken as the relevant temperature of the speed of sound in Eq. 3.61

$$T_{e1-m} = \frac{T_{v2-a} + T_{e1-a} + T_{v2-e} + T_{e1-e}}{4} \qquad (3.63)$$

In the case of zero EGR, the mass flow through channel 2 could now be derived from the known states pressure, temperature, and fluid velocity in the field $e1$. But since the model also includes EGR, the first step is to estimate the mass flow in channel 2 in order to receive a first approximate value of the mixing temperature T_{ch2-mx}. As a next step, a first value of the mass flow in channel 2 can be calculated ($\dot{m}_{ch2-a-app}$). Since the estimation of $\dot{m}_{ch2-a-app}$ is exact for steady-state conditions, no iteration is needed for T_{ch2-mx} and $\dot{m}_{ch2}$, respectively. The relative error during the simulation of a transient process is on the order of 1% and is thus negligible.

The mass flow in channel 2 is:

$$\dot{m}_{ch2} = \frac{p_2}{RT_{ch2-mx}} A_{ch2-eff} \, u_{ch2} \qquad (3.64)$$

where the effective area depends again both on the geometry and on the actual rotational speed of the PWS

$$A_{ch2-eff} = f(geometry, n_{pws}) \qquad (3.65)$$

and T_{ch2-mx} represents the mixing temperature

$$T_{ch2-mx} = \frac{c_{p-a} T_{e1-a} \dot{m}_{ch2-a-app} + c_{p-e} T_{e1-e} \dot{m}_{egr}}{c_{p-a} \dot{m}_{ch2-a-app} + c_{p-e} \dot{m}_{egr}} \qquad (3.66)$$

with the estimated air mass flow in channel 2

$$\dot{m}_{ch2-a-app} = \dot{m}_{ch3} + \dot{m}_{chg} - \dot{m}_{fuel-app} - \dot{m}_{egr} \qquad (3.67)$$

and the fuel mass flow for a stoichiometric air-to-fuel ratio

$$\dot{m}_{\text{fuel-app}} = (\dot{m}_{\text{ch3}} + \dot{m}_{\text{chg}}) \frac{k_{\text{stoich}}}{1 + k_{\text{stoich}}} \qquad (3.68)$$

The EGR rate $\dot{m}_{\text{egr}}$ in Eq. 3.66 and 3.67 is the sum of *high pressure EGR* and *low pressure EGR*. The EGR mass flow caused by incomplete scavenging in the low pressure part is an output variable of the submodel *Low Pressure Part*. After the computation of the whole *PWS Model*, the fraction of exhaust gases in channel 2 amounts to:

$$x_{\text{egr-ch2}} := \frac{\dot{m}_{\text{egr}}}{\dot{m}_{\text{ch2}}} \qquad (3.69)$$

where

$$\dot{m}_{\text{egr}} = \dot{m}_{\text{egr-hp}} + \dot{m}_{\text{egr-lp}} \qquad (3.70)$$

State x

Neglecting any reflection of the expansion wave $e1$, see Fig. 3.6, both at the contact front and at the wall of the gas side, the next relevant process is the expansion over the wave $e3$. The fluid at state $v1$ expands to state x due to the boundary condition $u = 0$ on the gas side since the fluid is flowing away from the wall. The boundary condition $u = 0$ leads to the pressure ratio over $e3$:

$$u_{\text{x-rel}} \equiv |u_{\text{v1}}|$$
$$= \sqrt{2RT_{\text{e3-m-first}}} \frac{\pi_{\text{e3-first}} - 1}{\sqrt{\pi_{\text{e3-first}} (\kappa_{\text{m}} + 1) + \kappa_{\text{m}} - 1}} \qquad (3.71)$$

where the relevant temperature for the speed of sound has to be estimated because it is an expansion process where the expanded pressure is not given

$$T_{\text{e3-m-first}} = \frac{T_{\text{e1-e}} + T_{\text{e1-a}}}{2} \qquad (3.72)$$

Using the first estimation of the relevant temperature for the speed of sound a first value of the pressure ratio π_{e3} can be derived. This allows to calculate a first approximate state x:

$$T_{\text{x-e-first}} = T_{\text{e1-e}} / \left(\pi_{\text{e3-first}} \frac{\pi_{\text{e3-first}} (\kappa_{\text{e}} - 1) + \kappa_{\text{e}} + 1}{\pi_{\text{e3-first}} (\kappa_{\text{e}} + 1) + \kappa_{\text{e}} - 1} \right) \qquad (3.73)$$

$$T_{\text{x}-\text{a}-\text{first}} = T_{\text{e1}-\text{a}} \Big/ \left(\pi_{\text{e3}-\text{first}} \frac{\pi_{\text{e3}-\text{first}} \left(\kappa_{\text{a}} - 1 \right) + \kappa_{\text{a}} + 1}{\pi_{\text{e3}-\text{first}} \left(\kappa_{\text{a}} + 1 \right) + \kappa_{\text{a}} - 1} \right) \qquad (3.74)$$

The first estimation of state x leads to the second value of the pressure ratio over the wave $e3$. Since the influence of the estimated temperature for the speed of sound on the pressure ratio is small compared to the influence of the boundary condition, the value of the resulting pressure ratio changes around 0.01% after the second iteration step. Therefore, the pressure ratio is known after two iteration steps:

$$u_{\text{x}-\text{rel}} \equiv |u_{\text{ch3}}| = \sqrt{2RT_{\text{e3}-\text{m}}} \frac{\pi_{\text{e3}} - 1}{\sqrt{\pi_{\text{e3}} \left(\kappa_{\text{m}} + 1 \right) + \kappa_{\text{m}} - 1}} \qquad (3.75)$$

with the second and final value of the relevant temperature for the speed of sound for wave $e3$

$$T_{\text{e3}-\text{m}} = \frac{T_{\text{v1}-\text{e}} + T_{\text{x}-\text{e}-\text{first}} + T_{\text{v1}-\text{a}} + T_{\text{x}-\text{a}-\text{first}}}{4} \qquad (3.76)$$

After two iteration steps, the state x is completely known:

$$p_{\text{x}} = \pi_{\text{e3}} \, p_{\text{v1}} \qquad (3.77)$$

$$u_{\text{x}} \equiv 0 \qquad (3.78)$$

$$T_{\text{x}-\text{e}} = T_{\text{e1}-\text{e}} \Big/ \left(\pi_{\text{e3}} \frac{\pi_{\text{e3}} \left(\kappa_{\text{e}} - 1 \right) + \kappa_{\text{e}} + 1}{\pi_{\text{e3}} \left(\kappa_{\text{e}} + 1 \right) + \kappa_{\text{e}} - 1} \right) \qquad (3.79)$$

$$T_{\text{x}-\text{a}} = T_{\text{e1}-\text{a}} \Big/ \left(\pi_{\text{e3}} \frac{\pi_{\text{e3}} \left(\kappa_{\text{a}} - 1 \right) + \kappa_{\text{a}} + 1}{\pi_{\text{e3}} \left(\kappa_{\text{a}} + 1 \right) + \kappa_{\text{a}} - 1} \right) \qquad (3.80)$$

Inflow Process Through Channel g

The GPV lowers the pressure p_3 to p_{g} by throttling. Even at lowest load condition the pressure in the gas pocket manifold is slightly higher than ambient pressure, since the PWS – from channel g via channel 4 to ambient – still represents a "throttle" with its pressure losses.

The isentropic expansion process caused by the wave $e3$ lowers the pressure p_3 to p_x. At lowest load condition, p_x is in the region of p_{1s} because the state change in the compression wave $s1$ is approximately compensated by the expansion process in the expansion wave $e3$, neglecting the difference of the process parameters n and κ, respectively.

Consequently, the gas pocket pressure p_g is higher than p_x for steady-state conditions. This explains why the exhaust gases from the gas pocket manifold also flow into the cell wheel.

Only during a short closing time of the GPV, p_g can drop below p_x. This transient phenomenon results from the receiver dynamic of the gas pocket manifold. At the first instant of closing the GPV fast, the mass flowing into the manifold "gas pocket" is smaller than the mass flowing out of the gas pocket into the PWS. This deficit between in- and outflowing mass is responsible for a pressure drop of p_g.

Simultaneously, the pressure p_x increases due to the rising pressure p_3. At a certain point in time, the pressure level in the field x is higher than in the gas pocket manifold. Consequently, the shock wave $s3$ changes to an expansion wave which causes a **backflow** out of the cell into the gas pocket manifold.

The *PWS Model* takes this backflow into account by changing the compression process $s4$ into the expansion process $(e4 - bf)$. When backflow occurs, the temperature T_{v3-e} is needed for the enthalpy flow from the PWS into the gas pocket manifold. That explains why T_{v3-e} is an output variable of the *PWS Model*, see Fig. 3.3.

The two cases that have to be distinguished are:

- **Flow into the PWS**: The exhaust gases are accelerated by the shock wave $s4$ similarly to $s1$. The mass flow through channel g is:

$$\dot{m}_{chg} = \frac{p_g}{RT_g}\, A_{chg-eff}\, u_{chg} \qquad (3.81)$$

with the fluid velocity

$$u_{chg} = u_{v3} = \sqrt{2RT_{x-m}}\,\frac{\pi_{s4} - 1}{\sqrt{\pi_{s4}\left(n_{s4-m} + 1\right) + n_{s4-m} - 1}} \qquad (3.82)$$

the pressure ratio

$$\pi_{s4} = \frac{p_{v3}}{p_x} = \frac{p_g}{p_x} \qquad (3.83)$$

and the relevant temperature for the speed of sound

$$T_{x-m} = \frac{T_{x-a} + T_{x-e}}{2} \tag{3.84}$$

- **Flow out of the PWS (backflow)**: Due to $p_g < p_x$, the shock wave $s4$ changes to the expansion wave $(e4 - bf)$. The exhaust gases at state x expand to state $v3$ and flow back into the gas pocket manifold. The mass flow and temperature are:

$$\dot{m}_{chg-bf} = \frac{p_g}{RT_{v3-e-bf}} A_{chg-eff} \, u_{chg-bf} \tag{3.85}$$

$$T_{v3-e-bf} = T_{x-e} / \left(\pi_{e4-bf} \frac{\pi_{e4-bf} (\kappa_e - 1) + \kappa_e + 1}{\pi_{e4-bf} (\kappa_e + 1) + \kappa_e - 1} \right) \tag{3.86}$$

with the fluid velocity

$$
\begin{aligned}
u_{chg-bf} &= u_{v3-bf} \\
&= -\sqrt{2RT_{e4-bf-m}} \frac{\pi_{e4-bf} - 1}{\sqrt{\pi_{e4-bf} (\kappa_m + 1) + \kappa_m - 1}}
\end{aligned} \tag{3.87}
$$

the pressure ratio

$$\pi_{e4-bf} = \frac{p_x}{p_{v3}} = \frac{p_x}{p_g} \tag{3.88}$$

and the relevant temperature for the speed of sound

$$T_{e4-bf-m} = \frac{T_{x-e} + T_{v3-e} + T_{x-a} + T_{v3-a}}{4} \tag{3.89}$$

Since the reflected shock wave $s5$ does not meet the open channel g, the effective channel area $A_{chg-eff}$ is independent of the rotational speed of the PWS:

$$A_{chg-eff} = f \, (geometry) \tag{3.90}$$

State y

Due to the deceleration (Eq. 3.91) the pressure in the cell after the completed *High Pressure Part* is higher than in channel g. This results from the shock reflection $s4$ to $s5$ at the air side. The theoretical

pressure ratio $\pi_{s5-\text{theo}}$ follows from the boundary condition *wall* at the air side:

$$u_{y-\text{rel}} \equiv |u_{v3}|$$

$$= \sqrt{2RT_{v3-m}} \; \frac{\pi_{s5-\text{theo}} - 1}{\sqrt{\pi_{s5-\text{theo}} \left(n_{s5-m} + 1\right) + n_{s5-m} - 1}} \qquad (3.91)$$

The real pressure ratio π_{s5} is:

$$\pi_{s5} = \eta_r \left(\pi_{s5-\text{theo}} - 1\right) + 1 \qquad (3.92)$$

with the same function for the shock reflection efficiency as shown in Eq. 3.40.

Pressure, fluid velocity, and temperature for air and exhaust gas at state y are:

$$p_y = \pi_{s5} \, p_{v3} \qquad (3.93)$$

$$u_y \equiv 0 \qquad (3.94)$$

$$T_{y-e} = T_{v3-e} \; \pi_{s5} \; \frac{\pi_{s5} \left(n_{s5-e} - 1\right) + n_{s5-e} + 1}{\pi_{s5} \left(n_{s5-e} + 1\right) + n_{s5-e} - 1} \qquad (3.95)$$

$$T_{y-a} = T_{v3-a} \; \pi_{s5} \; \frac{\pi_{s5} \left(n_{s5-a} - 1\right) + n_{s5-a} + 1}{\pi_{s5} \left(n_{s5-a} + 1\right) + n_{s5-a} - 1} \qquad (3.96)$$

If backflow into the gas pocket channel occurs, the state change from $v3$ to y is neglected due the pressure ratio p_x/p_{v3} which is close to 1. With the known state y the calculation of the *high pressure part* is finished. The state y is the input variable for the next process: the leakage out of the cell into the channels 4 and 1.

3.3.2   Leakage Phenomenon

Before channel 4 opens, leakage out of the cell into channel 4 and channel 1 occurs. The leakage mass flow lowers the pressure p_y to p_z which is the pressure before the first scavenging wave (wave $e5$, see Fig. 3.13). This pressure follows from identification. Assuming that the contact front remains approximately constant during the leakage process (see Fig. 3.12)

$$x_y \cong x_z \qquad (3.97)$$

and an isentropic state change in the cell since it is an expansion, the leakage mass flow is given by:

$$\dot{m}_{\text{le}-\text{e}} = (\dot{m}_{\text{ch3}} + \dot{m}_{\text{chg}} - \dot{m}_{\text{egr}-\text{hp}}) \left(1 - \frac{p_z}{p_y} \frac{T_{y-e}}{T_{z-e}}\right) \tag{3.98}$$
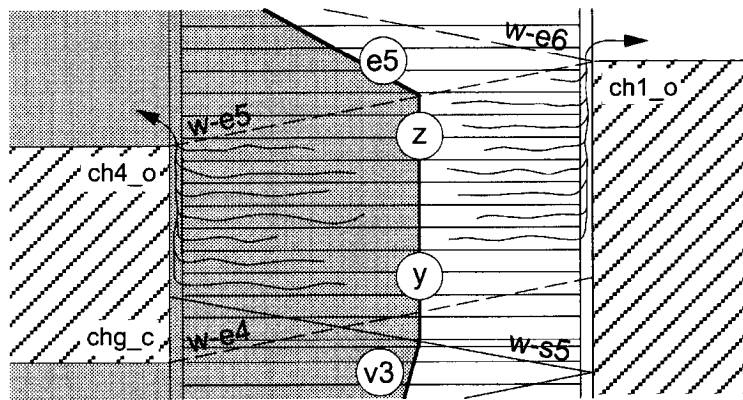
Figure 3.12: Leakage out of the cell wheel into channel 4 and into channel 1

In this model approach the leakage losses explain why the scavenging pressure p_z is lower than p_y. Using the equation 3.98, the leakage mass flow results from the identified model parameter p_z. Thus, if the value of the leakage mass flow is in the expected range, the value of p_z has to be in the correct region as well.

3.3.3   Low Pressure Part

The model for the *Low Pressure Part* assumes the simplified wave diagram shown in Fig. 3.13. Firstly, the state change including the coordinates of the mixing zone in all fields is to be calculated. Then, the position of the mixing zone at the place where channel 4 closes leads to the scavenging air mass flow in channel 4 and to the EGR mass flow caused by incomplete scavenging. Finally, the mass and energy balances deliver the mass and enthalpy flows in channel 4 and in channel 1.
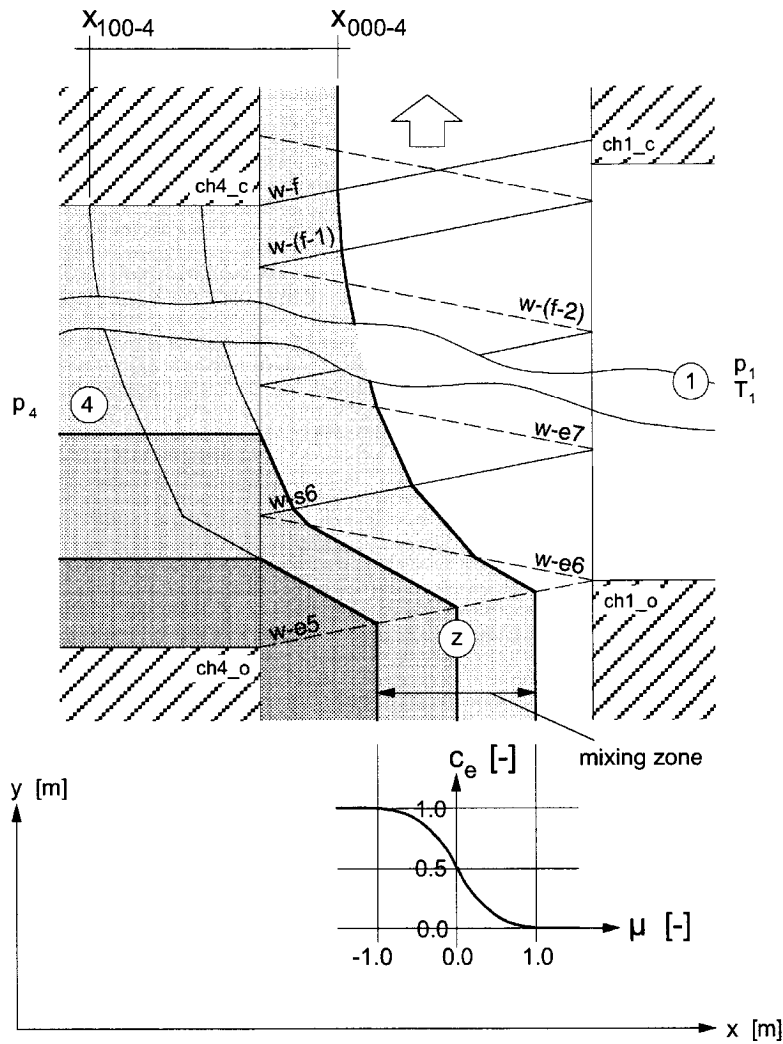
Figure 3.13: Model of simplified low pressure part

States in the Low Pressure Part

The first expansion wave of the *Low Pressure Part* (wave e5, see Fig. 3.13) accelerates the fluid in the cell towards channel 4, whereas all following expansion and shock waves decelerate the fluid from field to field due to the positive pressure difference:

$$\Delta p_{\mathrm{lp}} = p_4 - p_1 > 0\,.$$

When channel 4 closes, the boundary condition *wall* forces the shock wave f. It decelerates the fluid velocity to 0. Similarly to the calculation of the *High Pressure Part*, the state change in expansion waves

is assumed to be completely isentropic, whereas the same function for η_c as in Eq. 3.26 defines the polytropic state change in compression waves. The calculation of the submodel *low pressure part* is done as follows:

- The state change over the expansion wave i becomes:

$$u_i = u_{(i-1)} - u_{i-\text{rel}}$$

$$= u_{(i-1)} - \left(\sqrt{2RT_i} \frac{(\pi_i - 1)}{\sqrt{\pi_i(\kappa_i + 1) + \kappa_i - 1}} \right) \quad (3.99)$$

with the pressure ratio

$$\pi_i = \frac{p_4}{p_1} \quad (3.100)$$

the relevant temperature for the speed of sound (x_e is the dimensionless exhaust gas penetration)

$$T_i = x_{i-e} \frac{T_{i-e} + T_{(i-1)-e}}{2} + (1 - x_{i-e}) \frac{T_{i-a} + T_{(i-1)-a}}{2} \quad (3.101)$$

and the isentropic exponent

$$\kappa_i = x_{i-e} \kappa_e + (1 - x_{i-e}) \kappa_a \quad (3.102)$$

- The state change over the compression wave j becomes:

$$u_j = u_{(j-1)} - u_{j-\text{rel}}$$

$$= u_{(j-1)} - \left(\sqrt{2RT_j} \frac{(\pi_j - 1)}{\sqrt{\pi_j(n_j + 1) + n_j - 1}} \right) \quad (3.103)$$

with the pressure ratio

$$\pi_j = \frac{p_4}{p_1} \quad (3.104)$$

the relevant temperature for the speed of sound (x_e is the dimensionless exhaust gas penetration),

$$T_j = x_{j-e} T_{(j-1)-e} + (1 - x_{j-e}) T_{(j-1)-a} \quad (3.105)$$

and the polytropic exponent

$$n_j = x_{j-e} n_e + (1 - x_{j-e}) n_a \quad (3.106)$$

- The final process f is characterized by the boundary condition *wall* either on the gas or air side, depending on the wave diagram and PWS geometry:

$$p_f = \pi_f \ p_4 \qquad (3.107)$$

where the pressure ratio results from the boundary condition

$$u_f \equiv 0 = u_{(f-1)} - u_{f-\text{rel}}$$

$$= u_{(f-1)} - \left(\sqrt{2RT_f} \frac{(\pi_f - 1)}{\sqrt{\pi_f \ (n_f + 1) + n_f - 1}} \right) \qquad (3.108)$$

The pressure ratios over all waves in the *Low Pressure Part* is given by the thermodynamic boundary condition in channel 4, in channel 1, and by the scavenging pressure p_z. Thus, the calculation of the new, unknown state in the field i is done in the following steps:

1. The state in the field (i-1) is given by:
     - pressure: $p_{(i-1)}$
     - temperatures: $T_{(i-1)-e}$, $T_{(i-1)-a}$
     - fluid velocity: $u_{(i-1)}$
     - wave velocities: $w_{(i-1)-e}$, $w_{(i-1)-a}$
     - positions of the mixing zone: $x_{(i-1)-000}$, $x_{(i-1)-100}$

2. The given pressure in field i (either p_1 or p_4) leads to the temperature for exhaust gases and fresh air in field i:
     - temperatures: T_{i-e}, T_{i-a}

3. This allows to derive a weighted temperature for the speed of sound and a weighted process parameter for the wave i (Eq. 3.101, 3.102):
     - weighted temperature for the speed of sound: $T_{i-\text{sound}}$
     - weighted process parameter: n_i

4. Using these states, the fluid velocity and therefore the position of the mixing zone in field i can be calculated:
     - fluid velocity: u_i
     - positions of the mixing zone: x_{i-000}, x_{i-100}

5. Now, the state in field i is completely known:
   - pressure: p_i
   - temperatures: T_{i-e}, T_{i-a}
   - fluid velocity: u_i
   - wave velocities: w_{i-e}, w_{i-a}
   - positions of the mixing zone: x_{i-000}, x_{i-100}

This procedure is done for all fields in the *Low Pressure Part* with respect to the actual number of fields. That number depends on the actual rotational speed of the PWS.

Scavenging Mass Flow in Channel 4

The position of the mixing zone at the place where channel 4 closes, together with the exhaust gas fraction profile, allow to derive, firstly, a mean fraction of the scavenging air in channel 4 and, secondly, the scavenging air mass flow (for the nomenclature of the coordinates in x-dimension please see Fig. 3.10):

- dimensionless integration limits on the μ-axis for the scavenging air:

$$lim_{a-high-lp} = x_{ch4\_c} - \frac{x_{100-4}}{|x_{100-4} - x_{000-4}|/2} \qquad (3.109)$$

$$lim_{a-low-lp} = -1.0 \qquad (3.110)$$

- mean fraction of the scavenging air in channel 4:

$$\bar{c}_{a-lp} = 1 - \frac{1}{lim_{a-high-lp} - lim_{a-low-lp}} \int_{lim_{a-low-lp}}^{lim_{a-high-lp}} c_e(\mu)d\mu \qquad (3.111)$$

- scavenging air mass flow in channel 4:

$$\dot{m}_{ch4-a} = \bar{c}_{a-lp} \left(x_{ch4\_c} - x_{100-4}\right) \cdot$$
$$\frac{p_4}{RT_{(f-1)-a}} \frac{n_{PWS}}{60} \pi \left(r^2_{ch4-o} - r^2_{ch4-i}\right) \qquad (3.112)$$

Low Pressure EGR

The EGR mass flow caused by incomplete scavenging is called *low pressure EGR*. It can be calculated with respect to the mixing zone at location f.

In order to derive a mean fraction of the exhaust gases, the position of the mixing zone at the very location has to be derived. Two cases must be distinguished:

- The *high pressure EGR* mass flow is zero. The mixing zone at the place where channel 4 closes is still complete.

- *High pressure EGR* occurs. Then, the mixing zone at the place where channel 4 closes is incomplete since one part of the original mixing zone is already in channel 2.

The derivation of the mean fraction of the exhaust gases at the place where channel 4 closes takes into account the effect described above:

- dimensionless integration limits on the μ-axis for the exhaust gases:

$$lim_{\text{e}-\text{high}-\text{lp}} = \begin{cases} lim_{\text{e}-\text{low}-\text{hp}} : \dot{m}_{\text{egr}-\text{hp}} \neq 0 \\ 1.0 \qquad\qquad : \dot{m}_{\text{egr}-\text{hp}} = 0 \end{cases} \quad (3.113)$$

$$lim_{\text{e}-\text{low}-\text{lp}} = lim_{\text{e}-\text{high}-\text{lp}} - \frac{x_{000-4}}{|x_{100-4} - x_{000-4}|/2} \quad (3.114)$$

- mean fraction of the exhaust gases in the cell wheel after *channel 4 closes*:

$$\bar{c}_{\text{e}-\text{lp}} = \frac{1}{lim_{\text{e}-\text{high}-\text{lp}} - lim_{\text{e}-\text{low}-\text{lp}}} \int\limits_{lim_{\text{e}-\text{low}-\text{lp}}}^{lim_{\text{e}-\text{high}-\text{lp}}} c_{\text{e}}(\mu)d\mu \quad (3.115)$$

- *low pressure EGR* mass flow caused by incomplete scavenging:

$$\dot{m}_{\text{egr}-\text{lp}} = \bar{c}_{\text{e}-\text{lp}} \left(x_{000-4} - x_{\text{ch4\_c}} \right) \cdot$$
$$\frac{p_4}{RT_{(\text{f}-1)-\text{e}}} \frac{n_{\text{PWS}}}{60} \pi \left(r^2_{\text{ch4}-\text{o}} - r^2_{\text{ch4}-\text{i}} \right) \quad (3.116)$$

States in Channel 4 and Channel 1

The mass flow in channel 4 and in channel 1 follow from the mass balance:

$$\dot{m}_{ch4} = \dot{m}_{ch3} + \dot{m}_{chg} - \dot{m}_{egr} + \dot{m}_{ch4-a} \qquad (3.117)$$

$$\dot{m}_{ch1} = (\dot{m}_{ch2} - \dot{m}_{egr}) + \dot{m}_{ch4-a} \qquad (3.118)$$

Together with the known mass flows of exhaust gases and scavenging air the expanded temperature of the exhaust gases and of the remaining charged air in field $e5$ define the mixing temperature in channel 4. Since the process parameters n and κ are different for compression and expansion processes, the temperatures in the fields e5, s6, ..., (f-1) change slightly. Nevertheless, these differences can be neglected due to

$$p_4 \, / \, p_1 \simeq 1 \; \rightarrow n \; \simeq \; \kappa \, .$$

Thus, the expanded temperature for both the exhaust gases and the scavenging air in channel 4 can be approximated by the temperature in field $e5$ after the first scavenging wave $e5$ (see Fig. 3.13). Then, the mixing temperature in channel 4 becomes:

$$T_{ch4-mx} = \frac{c_{p-e}\,\dot{m}_{ch4-e}\,T_{e5-e} + c_{p-a}\,\dot{m}_{ch4-a}\,T_{e5-a}}{c_{p-e}\,\dot{m}_{ch4-e} + c_{p-a}\,\dot{m}_{ch4-a}} \qquad (3.119)$$

3.4   Model of Engine System

The first subsection explains how mass flow, exhaust temperature, and torque of the SI engine are modeled. The next two subsections then show the modeling of the parts receiver and throttle.

3.4.1   SI Engine Model

Mass Flow Through SI Engine

The volumetric efficiency λ_l of an SI engine describes the amount of gas flowing through the SI engine as a function of the thermodynamic states in the intake and exhaust manifolds as well as of the engine speed (Eq. 3.121), Heywood (1988). The volumetric efficiency λ_l is identified by measurements taken on the engine system. The sum of fresh air and fuel and recirculated exhaust gases through the engine is:

$$\dot{m}_{\text{eng}} = \lambda_l \, \frac{p_{\text{im}}}{R T_{\text{im}}} \, V_{\text{dis}} \, \frac{1}{2} \, \frac{n_{\text{eng}}}{60}$$
$$= \dot{m}_{\text{air}} + \dot{m}_{\text{fuel}} + \dot{m}_{\text{egr}} \qquad (3.120)$$

with the volumetric efficiency

$$\lambda_l = f(p_{\text{im}}, p_{\text{em}}, n_{\text{eng}}) \qquad (3.121)$$

The injected fuel flow is controlled by:

1. Feed-forward control by measuring intake manifold pressure.

2. Air-to-fuel ratio feed-back control based on the switch-type-air-to-fuel-sensor information.

Thus, the fuel mass flow for a stoichiometric air-to-fuel ratio becomes:

$$\dot{m}_{\text{fuel}} = \dot{m}_{\text{eng}} \frac{k_{\text{stoich}}}{1 + k_{\text{stoich}}} \qquad (3.122)$$

Temperature After Exhaust Valve

The engine outlet temperature just after the outlet valve is nearly constant over the engine's operating range. The differences in burning from one cycle to another are slight and therefore negligible. In contrast, the temperature of exhaust gases measured approximately 15 cm after the outlet valve increases with rising engine torque, see Fig. 3.14. The reason for this dependency is the rising mass flow of the exhaust gases which causes an increasing pressure in the outlet system. Since the outlet temperature just after the outlet valve cannot be measured, the temperature measured approximately 15 cm after the outlet valve is taken as being the temperature of the exhaust gases leaving the engine.
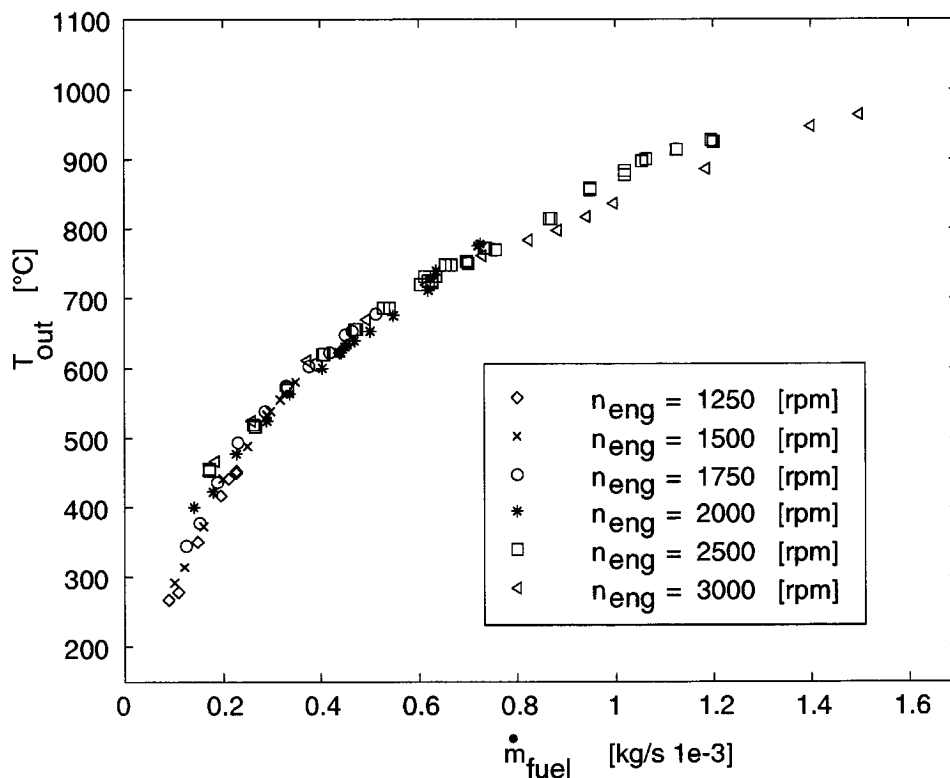
Figure 3.14: Measured temperature approximately 15 cm after outlet valve for different engine speeds as a function of fuel mass flow

In the *PWS Engine Model* this temperature is needed for the enthalpy flow into the exhaust manifold, see Fig. 3.2. In the following

the term *outlet temperature* is used for the temperature measured approximately 15 cm after the outlet valve. The outlet temperature can be described by a static function of fuel mass flow neglecting the small influence of engine speed, whereas the impact of EGR is not clear. Exhaust gases in the cylinder are inert gases which diminish the amount of oxygen available. As a result, not all the injected fuel can burn. This leads to a lower temperature in the exhaust manifold. On the other hand, the slower burning increases the outlet temperature and thus the temperature in the exhaust manifold. Since these two effects are in conflict, the outlet temperature is assumed to be independent of the EGR rate (Eq. 3.123) as long as the EGR rate is below 20%, when misfiring should not occur (Heywood (1988)).

$$T_{\text{out}} = f(\dot{m}_{\text{fuel}}) \tag{3.123}$$

Engine Torque

The engine torque can be described by a static function of fuel mass flow and engine speed (*Willans* approach, Heywood (1988)). It is assumed that the amount of fuel injected during the time of transient EGR does not change. Then, the transient EGR mass flow behaves like inert gas in the cylinder which diminishes the amount of free oxygen available for combustion. Thus, not all the injected fuel can burn:

$$T_{\text{eng}} = (1 - x_{\text{egr}}) \cdot f(\dot{m}_{\text{fuel}}, n_{\text{eng}}) \tag{3.124}$$

3.4.2 Receiver Model

The state change of a receiver is described by the mass *and* energy balances between inflow and outflow, assuming a perfect gas behavior. The formulation of the energy balance is necessary due to the charging process. This causes a temperature in the tubes different from ambient temperature (Hendricks (2001)).

The thermodynamic states such as pressure, temperatures (of fluid *and* wall in the outlet system), and mass are described by a mean value model (Pianese and Rizzo (1992)).

Mean value states of the fluid in a receiver:

$$\frac{dm_{\text{rec}}}{dt} = \dot{m}_{\text{in}} - \dot{m}_{\text{out}} \tag{3.125}$$

$$\frac{dT_{\mathrm{rec}}}{dt} = \frac{1}{c_{\mathrm{v}} m_{\mathrm{rec}}} \Big(\dot{H}_{\mathrm{in}} - \dot{H}_{\mathrm{out}} -$$

$$\dot{Q}_{\mathrm{conv-fluid}} - \dot{Q}_{\mathrm{rad-fluid}} - \frac{dm_{\mathrm{rec}}}{dt} c_{\mathrm{v}} T_{\mathrm{rec}} \Big) \qquad (3.126)$$

$$p_{\mathrm{rec}} = \frac{m_{\mathrm{rec}} R T_{\mathrm{rec}}}{V_{\mathrm{rec}}} \qquad (3.127)$$

Mean value state of the wall temperature:

$$\frac{dT_{\mathrm{wall}}}{dt} = \frac{1}{c_{\mathrm{v-wall}} m_{\mathrm{wall}}} \Big(\Big(\dot{Q}_{\mathrm{conv-fluid}} + \dot{Q}_{\mathrm{rad-fluid}} \Big) -$$

$$\Big(\dot{Q}_{\mathrm{conv-wall}} + \dot{Q}_{\mathrm{rad-wall}} \Big) \Big) \qquad (3.128)$$
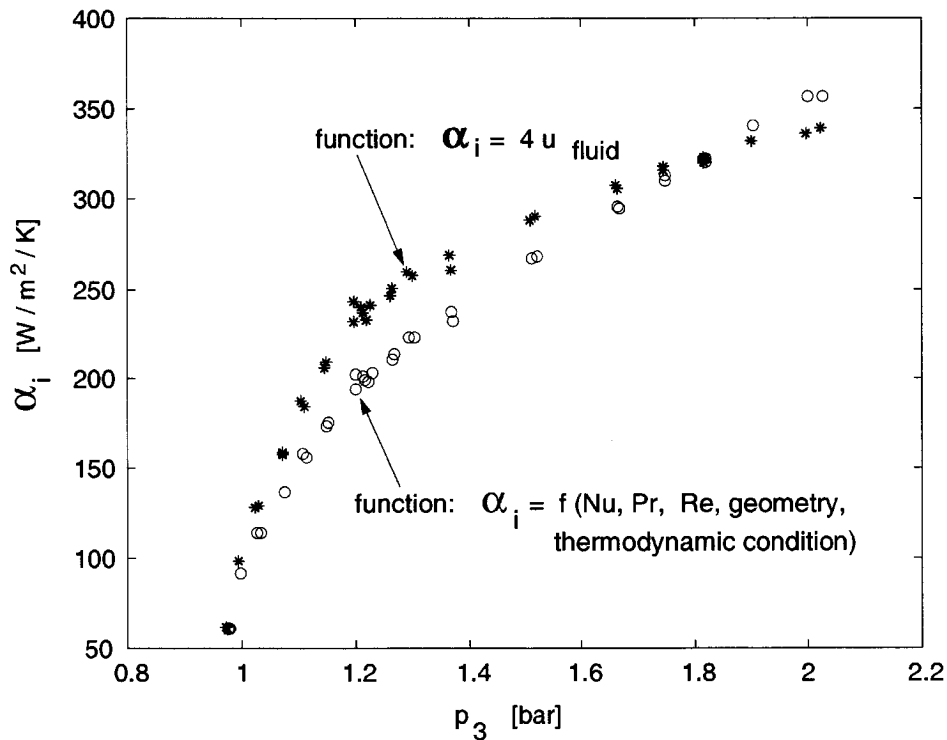
Figure 3.15: Heat transfer coefficient in the tube (p_3 represents the engine load range, the heat transfer coefficient is not only a function of p_3)

The heat transfer coefficient needed in Eq. 3.128 depends on the thermodynamic state and the geometry in the tube (Wisniewski

(1998), Shayler et al. (1999), Zhang et al. (1992)). Using these data, the Prandtl, Reynolds, and Nusselt numbers can be derived, which lead to the value of α. For the given geometry and thermodynamic states over the entire load range of the engine, a strong dependency of α on the fluid velocity in the exhaust manifold can be found, see Fig. 3.15, Pivec et al. (1998). In order to save computing time, this dependency is used to derive the actual heat transfer coefficient since the variable fluid velocity in the tube is already a known state:

$$\alpha_i = f(u_{\text{fluid}}) \tag{3.129}$$

The assumption of constant ambient condition (velocity, pressure, temperature) leads to:

$$\alpha_a = constant \tag{3.130}$$

3.4.3   Throttle Model

The throttle is seen as an adiabatic system (Baehr (1992)). All the neglected heat losses are described by the enclosing receivers, see Eq. 3.126. Assuming an isentropic acceleration of the fluid and an energy dissipation immediately after the throttling area at the same pressure, the complete state change over the throttle shows approximately an *isenthalpic* behavior. The air flow through a throttle then is computed as a function of its opening angle pos_{th} and of the states of the enclosing receivers. The throttles in the simulation tool *PWS Engine Model* take backflow into account as well.

The throttle coefficient c_{th} represents all the neglected friction losses and also the difference between geometrically calculated area and effective area. Thus, the mass flow through a throttle can be validated by adjusting the throttle coefficient (Mattarelli and Valentini (2000)). In this model approach, the throttle coefficient is assumed to be a function of the opening area .

The states of the receiver upstream have the index 1, downstream the index 3. The temperature of the fluid after throttling has the index 2. The temperature directly after the throttle is:

$$T_1 \equiv T_2 \tag{3.131}$$

The specific mass flow through the throttle is:

$$\frac{\dot{m}}{A \cdot c(pos_{\text{th}})} = \begin{cases} \frac{p_1}{\sqrt{RT_1}} \sqrt{\frac{2\kappa}{\kappa-1} \left[\left(\frac{p_3}{p_1}\right)^{\frac{2}{\kappa}} - \left(\frac{p_3}{p_1}\right)^{\frac{\kappa+1}{\kappa}} \right]} & : (i) \\ \frac{p_1}{\sqrt{RT_1}} \sqrt{\kappa} \left(\frac{2}{\kappa+1}\right)^{\frac{\kappa+1}{2(\kappa+1)}} & : (ii) \end{cases}$$

$$\begin{aligned} (i) \quad &(\text{subsonic}) : 1 \geq \frac{p_3}{p_1} \geq \left(\frac{2}{\kappa+1}\right)^{\frac{\kappa}{\kappa-1}} \\ (ii) \quad &(\text{sonic}) \quad : \frac{p_3}{p_1} < \left(\frac{2}{\kappa+1}\right)^{\frac{\kappa}{\kappa-1}} \end{aligned} \qquad (3.132)$$

Seite Leer /
Blank leaf

Chapter 4

Model Validation

This chapter describes the identification of the model parameters and presents both the validated static *PWS Model* and the validated simulation tool *PWS Engine Model*. The first section describes how the model parameters of the *PWS Model* are identified and shows the resulting validated *PWS Model*. The validated *PWS Model* then is inserted as a submodel into the simulation tool *PWS Engine Model*. The second section explains the procedure of validating the simulation tool *PWS Engine Model* and compares model prediction and measurement data during transients. The simulation tool not only requires a validation of its dynamics but also a static validation because the errors of each submodel are cumulative. The third section briefly recapitulates all the steps of identification and validation.

4.1 Validation of the *PWS Model*

The first subsection describes the principles of the parameter identification and the validation of the *PWS Model*. In Sect. 4.1.2 the identified model parameters are presented, and the last subsection shows the results of the validated *PWS Model*.

IDENTIFICATION
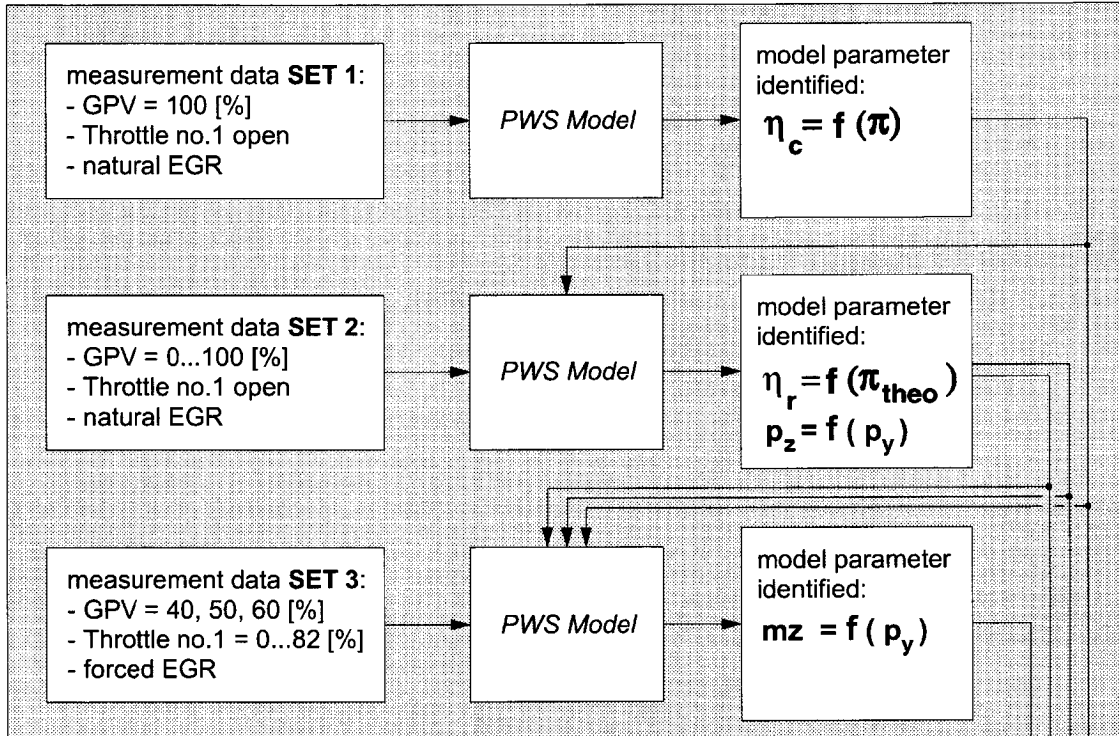
VALIDATION
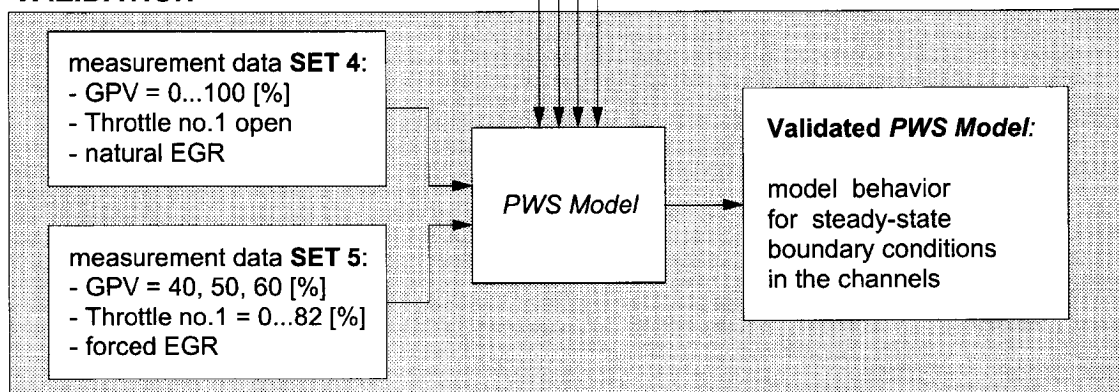
Figure 4.1: Steps of model parameter identification and validation of the *PWS Model*

4.1.1 Principles for Static Validation

Parameter Identification

The procedure of validating the static behavior of the *PWS Model* is depicted in Fig. 4.1. In order to derive the model parameters

$$\eta_c, \quad \eta_r, \quad p_z, \quad \text{and } mz,$$

the identification requires a full set of steady-state measurement data which is completely different from the data needed for validation. This is achieved by measuring each engine operating point twice. The criterion for each model parameter is the relative error of a specific model output, see Fig. 4.1. The relative error of the state x is defined as follows:

$$\epsilon(x) := \frac{1}{i} \sum_i \frac{|x_{i-\text{meas}} - x_{i-\text{calc}}|}{x_{i-\text{meas}}} \tag{4.1}$$

step	model parameter	criterion	limits
i)	$\eta_c = f(\pi)$	$\epsilon(\dot{m}_{ch3}) \leq 0.001$	$0 \leq \eta_c \leq 1$
ii)	$\eta_r = f(\pi_{theo})$	$\epsilon(\dot{m}_{ch2}, T_{ch2\text{-}mx}) \leq 0.001$	$0 \leq \eta_r \leq 1$
iii)	$p_z = f(p_y)$	$\epsilon(\dot{m}_{ch4\text{-}a}) \leq 0.001$	$p_4 \leq p_z \leq p_y$
iv)	$mz = f(p_y)$	$\epsilon(\dot{m}_{egr}) \leq 0.001$	$0 \leq mz \leq 1_{rot}$ $0 \leq mz \leq 2 x_y$

Table 4.1: Model parameters of the *PWS Model*

The model parameter identification is characterized by the following steps:

- **Step *i)*:** As a first step, the compression efficiency is identified by adjusting the compression efficiency for the compression processes of the inflow process through channel 3. The measurement delivers the mass flow of exhaust gases by measuring the

fuel mass flow and the signal of λ_v. Therefore, only the sum of the two mass flows through channel 3 and channel g is known. That explains why the first step of identification requires measurement data with fully closed GPV, see Fig. 4.1. In this case the gas pocket mass flow is 0 and the criterion for η_c is known.

- **Steps *ii), iii)*:** Using the identified function of η_c the reflection efficiency η_r and then the scavenging pressure p_z can be identified. The criterion for η_r is the mean error of mass flow and temperature in channel 2 because both influence the dynamic state in the receiver 2 of the simulation tool *PWS Engine Model*. The criterion for the model parameter p_z is the scavenging air mass flow in channel 4 rather than the sum of the scavenging air and the exhaust gases since the exhaust gas mass flow in channel 4 for steady-state conditions is identical to the exhaust gas mass flows in channels 3 and g, both of which are validated already by η_c.

- **Step *iv)*:** The target of the fourth step is to identify the mixing zone length from measurements. This requires measurement data with forced steady-state EGR which can be realized by:

   - Rotational speed of the PWS in the region of 50 ... 20% of the nominal value $\rightarrow$ wave process significantly disturbed.
   - Lowering p_1 by partially closing the throttle no. 1 $\rightarrow$ wave process still well tuned.

The forced EGR causes a slightly different speed of sound for the waves due to the higher temperature level in the whole wave process. But, as explained in Chapter 3, the influence of the speed of sound on the wave velocity is of second order compared to the influence of the pressure ratio on the wave velocity. Therefore, the wave process remains approximately the same but with different temperatures, which allows to use the developed *PWS Model* for prediction.

In contrast, the rotational speed of the PWS has to be lowered to 20% of the nominal value in order to force an EGR rate of about 15%. The changes of the pressure wave process cannot be neglected. Although the *PWS Model* takes into account the influence of the rotational speed of the PWS for the derivation of

the effective channel areas, the model accuracy for such dramatically changed rotational speeds of the PWS cannot be guaranteed. Therefore, the measurement data with forced steady-state EGR are obtained by lowering p_1 at the throttle no. 1 and not by a too slow rotational speed of the PWS.

Model Validation

After the identification of the four model parameters, the *PWS Model* is validated for the following two cases:

1. Throttle no.1 fully open: the system "PWS SI engine" operates without forced EGR. In this case the states of interest are the following mass flows and mixing temperatures in the channels of the PWS:
   - channel 2   : $\dot{m}_{ch2}$, T_{ch2-mx}
   - channel 3   : $\dot{m}_{ch3}$
   - channel g   : $\dot{m}_{chg}$
   - channel 4   : $\dot{m}_{ch4-a}$, T_{ch4-mx}

2. Throttle no.1 partially closed: the system "PWS SI engine" operates with forced EGR. In this case only the influence of the lowered pressure p_1 on the scavenging process is of interest:
   - channel 2   : x_{egr}
   - channel 4   : $\dot{m}_{ch4-a}$

   For both cases, the model outputs are calculated as a function of the following measured thermodynamic boundary condition:
   - channel 1   : p_1 , T_1
   - channel 2   : p_2
   - channel 3   : p_3 , T_3
   - channel g   : p_g , T_g
   - channel 4   : p_4
   - PWS   : $n_{pws-act}$

In the following two subsections, the identified model parameters and the results of the validated *PWS Model* are shown. The instrumentation of the system "PWS SI engine" and how the states of interest are derived from the measurement data are described in Appendix A.

4.1.2 Identified Model Parameters of the *PWS Model*

The following subsection presents graphically and discusses the identified functions of:

1. Compression Efficiency: $\eta_c = f(\pi)$

2. Reflection Efficiency: $\eta_r = f(\pi_{\text{theo}})$

3. Scavenging Pressure: $p_z = f(p_y)$

4. Mixing Zone: $mz = f(p_y)$
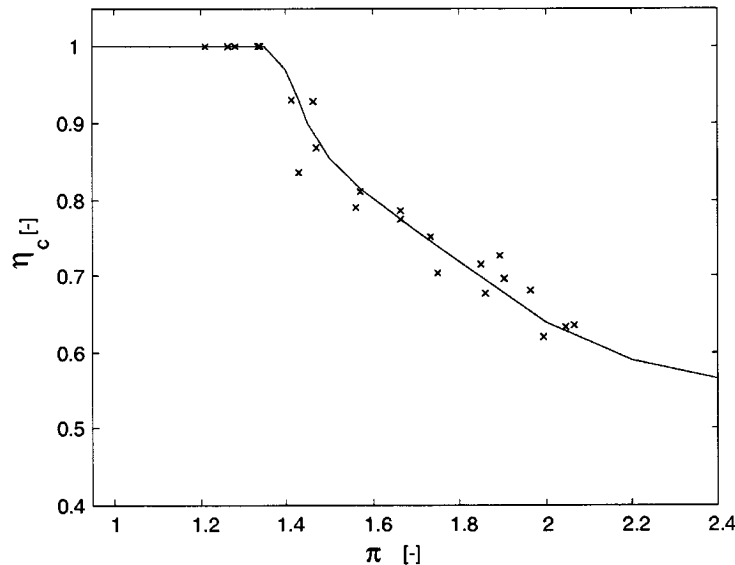
Figure 4.2: Identified compression efficiency as a function of the pressure ratio over a compression wave;
'x': values for $\epsilon = 0.001$, '–' identified function

1. Compression Efficiency: For a pressure ratio near 1 the state change in a compression process is nearly isentropic, whereas the state change becomes more polytropic as the pressure ratio increases. The identified function of the compression efficiency describes this characteristic, see Fig. 4.2.

2. Reflection Efficiency: At a theoretical pressure ratio of 1 the reflection efficiency has to be equal to 1 since there exists no leakage
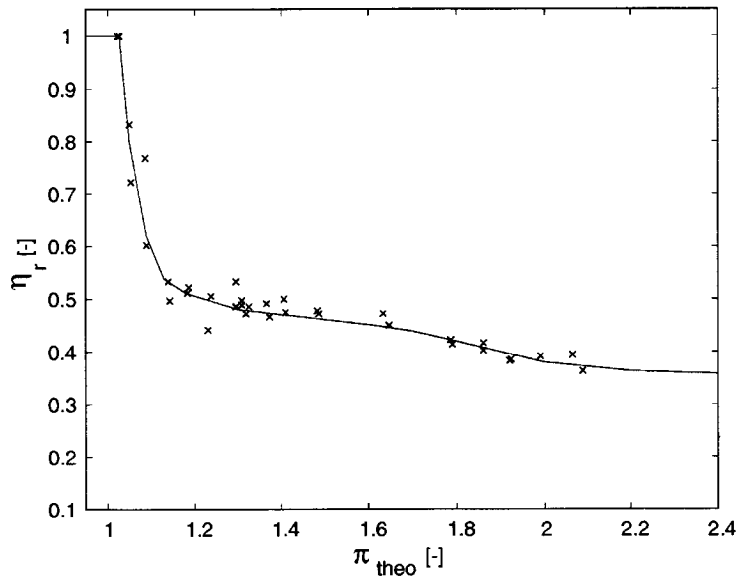
Figure 4.3: Identified reflection efficiency as a function of the theoretical pressure ratio over a shock reflected at a wall; 'x': values for $\epsilon = 0.001$, '$-$' identified function
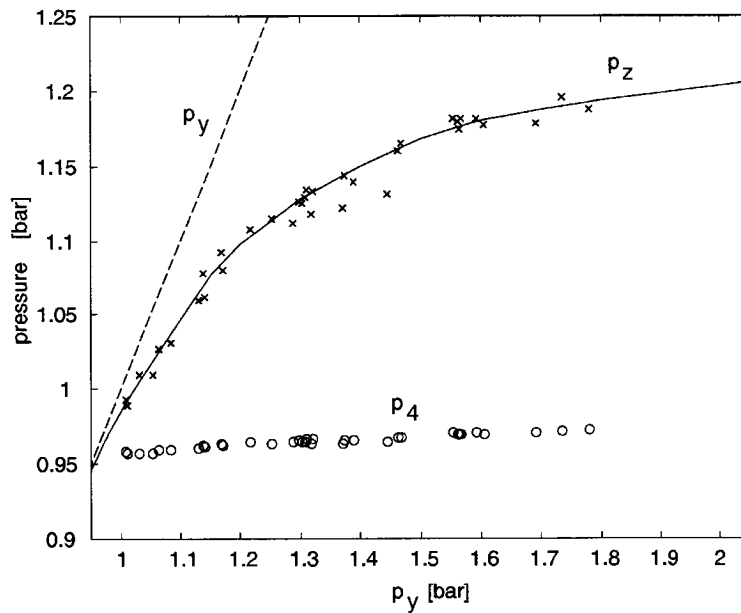
Figure 4.4: Identified scavenging pressure as a function of p_y; 'o': measured values of p_4; 'x': values for $\epsilon = 0.001$, '$-$' identified function

at that ratio. The leakage losses, which affect a smaller real pressure ratio for the reflected shock than the theoretical pressure ratio, have to rise with an increasing theoretical pressure ratio. This behavior is described by the identified function of η_r, see Fig. 4.3.

3. Scavenging Pressure: The identified function of p_z has to be between the calculated values of p_y and the measured values of p_4 (thermodynamic boundary condition). For a low pressure level of p_y the expected leakage losses between the high and low pressure parts of the wave process have to be small. Hence, p_z is close to p_y in this region but not larger than p_y since the leakage mass flow cannot be negative. The higher the pressure level of p_y is, the more significant the leakage losses have to be. The difference between p_z and p_y has to increase in this region. The identified function of p_z shows this behavior, see Fig. 4.4.

4. Mixing Zone: Compared to the range of p_y in Fig. 4.4 the ranges of p_y in Fig. 4.5 and 4.6 are smaller due to the smaller range of the measurement data when EGR is forced by lowering the pressure p_1. The mixing zone length is identified for both assumptions of the exhaust gas fraction profile:

- the tangens hyperbolicus profile

- the linear profile.

Testing these two profiles the values obtained for $\epsilon = 0.001$ do not show a significantly different standard derivation for one specific profile, compare Fig. 4.5 and 4.6. Consequently, the accuracy of the *PWS Model* does not depend on the exhaust gas fraction profile chosen.

In the following, the linear profile is taken for the model validation due to the slightly smaller standard derivation of the values with the relative error $\epsilon = 0.001$.

The length of the mixing zone is assumed to be a function of p_y due to the following two facts:

- The exhaust gas penetration at location y reaches its maximum.

- The mixing zone in the field y is already fully developed due to the available time for building a new mixing zone, see Sect. 3.3.1.
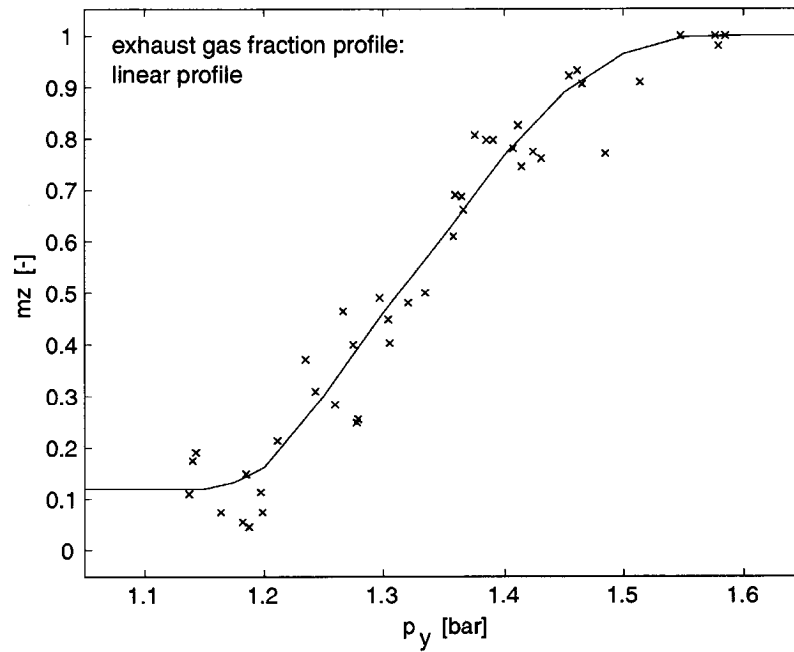
Figure 4.5: Identified mixing zone length assuming a linear exhaust
gas fraction profile;
'x': values for $\epsilon = 0.001$, '−' identified function
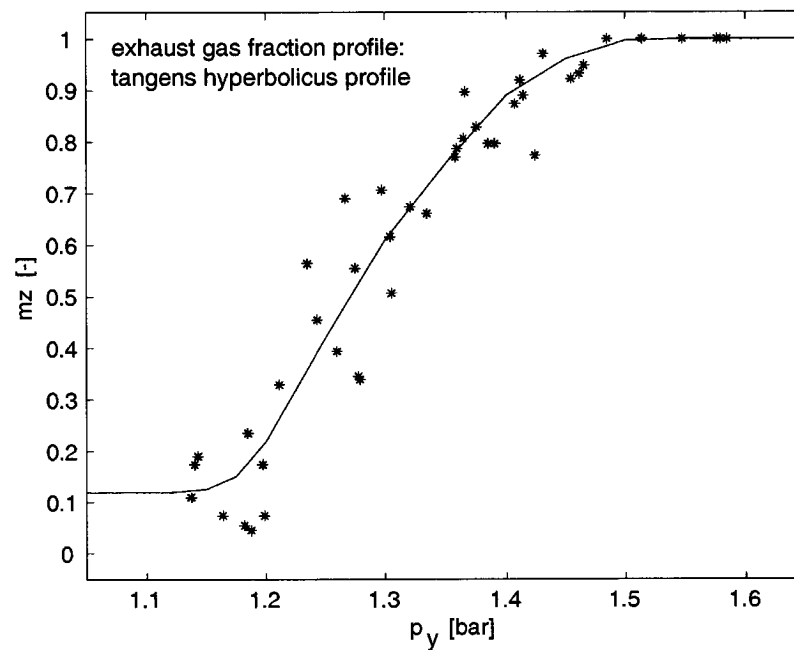
Figure 4.6: Identified mixing zone length assuming a tangens hyper-
bolicus exhaust gas fraction profile;
'x': values for $\epsilon = 0.001$, '−' identified function

4.1.3   Validated *PWS Model*

Model Inputs and Outputs

After the identification of the four model parameters, the *PWS Model* can be validated for the following two cases:

1. Throttle no.1 open: the system "PWS SI engine" operates without forced EGR.

2. Throttle no.1 partially closed: the system "PWS SI engine" operates with forced EGR.

In the first case the states of interest are the mass flows and mixing temperatures in the channels of the PWS, where the *natural* EGR is of minor importance (about 1.0% of the typical value of the mass flows in the channels). In the second case the focus is on the influence of the lowered pressure p_1 on the scavenging process. Thus, the outputs of the *PWS Model* are:

1. Throttle no.1 open, natural EGR:
   - channel 2   : $\dot{m}_{ch2}$, T_{ch2-mx}
   - channel 3   : $\dot{m}_{ch3}$
   - channel g   : $\dot{m}_{chg}$
   - channel 4   : $\dot{m}_{ch4-a}$, T_{ch4-mx}

2. Throttle no.1 partially closed, forced EGR:
   - channel 2   : x_{egr}
   - channel 4   : $\dot{m}_{ch4-a}$

The total mass flow in channel 4 results from the known mass flows of the exhaust gases and of the scavenging air, see Eq. 3.117. The mass flow in channel 1 follows from the known states in channels 2 and 4, see Eq. 3.118, Chap. 3.

The model outputs are a function of the thermodynamic boundary condition in the channels. Despite this fact, all model results are presented graphically as a function of p_3 only, because its range represents the entire operating range of the SI engine. As a result, the calculated model outputs do not show a smooth behavior over p_3.

A second reason for this behavior is the measurement error of state k which is around 0.5% (Inhelder (1996)):

$$p_k \pm \delta p$$
$$T_k \pm \delta T$$
$$\text{where } \delta p/p_k, \delta T/T_k \approx 0.5\%$$

Model Prediction and Measurement for Throttle no.1 Fully Open

The results of the validated *PWS Model* for the case of open throttle no. 1 (without forced EGR) are discussed in the list below whereas the following pages depict the validated model outputs. The Appendix B shows as an example one calculated pressure wave diagram.

- **Model Outputs in Channel 3 and in Channel g:** The model prediction of the mass flow through channel 3 and channel g shows a relative error on the order of 5%, see Fig. 4.7. The calculated mass flows through both channels point out the working principle of the GPV. When the GPV is closed, the mass flow through channel g decreases until it is 0 for a fully closed GPV. Simultaneously, the mass flow through channel 3 increases due to the rising pressure p_3. The sum of both calculated mass flows is compared with the measured exhaust gas mass flow. Please notice that:

  1. The mass flow through channel g does not directly depend on the actual GPV position but on the thermodynamic state in channel g which is given by the thermodynamic behavior of the system "PWS SI engine" and the actual GPV position.

  2. The function of η_c – found by identification using measurement data with zero mass flow in channel g – also defines the process parameter n for the inflow process through channel g as well as for all compression processes. The satisfactory agreement between measurement and prediction shows that η_c accurately describes the state change in compression processes.

- **Model Outputs in Channel 2**: The relative errors of the model outputs in channel 2 are on the order of 5%, see Fig. 4.8 and 4.9, except for the temperature at low pressure levels. In this region, the heat transfer from the PWS body to the compressed air in channel 2 leads to a higher temperature than predicted. The influence of the rising natural EGR rate in this region on the mixing temperature in channel 2 is taken into account by the model, see Fig. 4.17.

- **Model Outputs in Channel 4**: The prediction of the scavenging air mass flow in channel 4 is satisfactory, see Fig. 4.10. In contrast, the predicted mixing temperature in channel 4 shows a mean relative error of around 8% due to the neglected heat losses from channel 4 via the PWS body into the wall of the tube and into ambient, see Fig. 4.11. The model error increases again in the region of low engine operating conditions where the heat losses lower the temperature significantly due to the fairly small absolute value of the enthalpy flow.

- **Identified Leakage Losses**: The nonmeasurable leakage mass flow results from the identified p_z. The maximum value of the leakage fraction is around 10% (see Fig. 4.12) which is in the expected range (Hörler (1969)).

- **Exhaust Gas Penetration**: The only place in the wave process where the calculated pressure wave diagram can be validated with measurements is the field y. At this location, the exhaust gas penetration derived from the calculated wave diagram can be compared with the exhaust gas penetration which follows from measured states:

$$x_{\text{y−meas}} = \frac{\dot{m}_{\text{(ch3+chg)−meas}}}{\frac{p_{\text{g−meas}}}{RT_{\text{g−meas}}} \; \frac{n_{\text{pws}}}{60} \; \pi \; \left(r^2_{\text{chg−o}} - r^2_{\text{chg−i}} \right)} \tag{4.2}$$

The error between prediction and measurement for the position y is smaller than 5%, see Fig. 4.13, which leads to the following conclusions:

  1. The simplified wave diagram takes into account the relevant waves.

2. The neglect of the wave reflection at the contact front is allowable.

3. The calculated wave, fluid, and sound velocities are in the correct region.
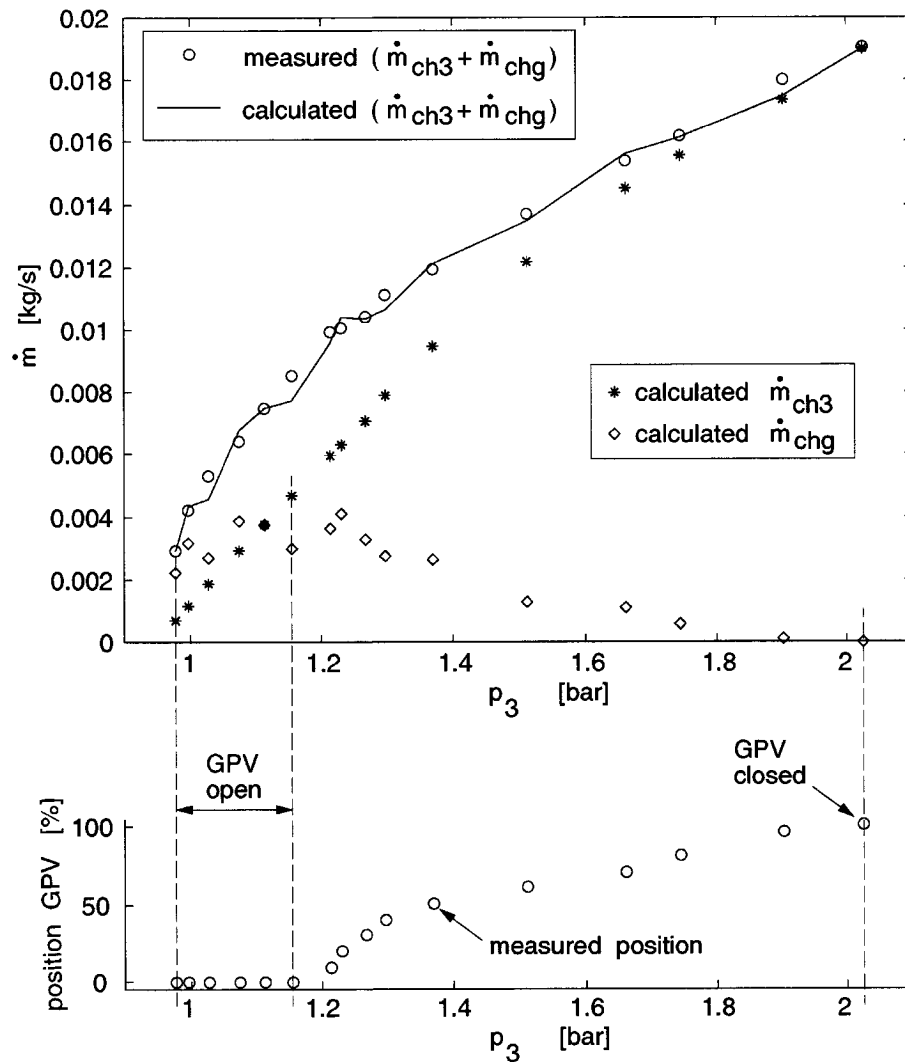
Figure 4.7: Above: model prediction of the sum of the mass flows in channel 3 and channel g compared with the measured ('o') exhaust gas mass flow through both channels; Below: measured GPV position
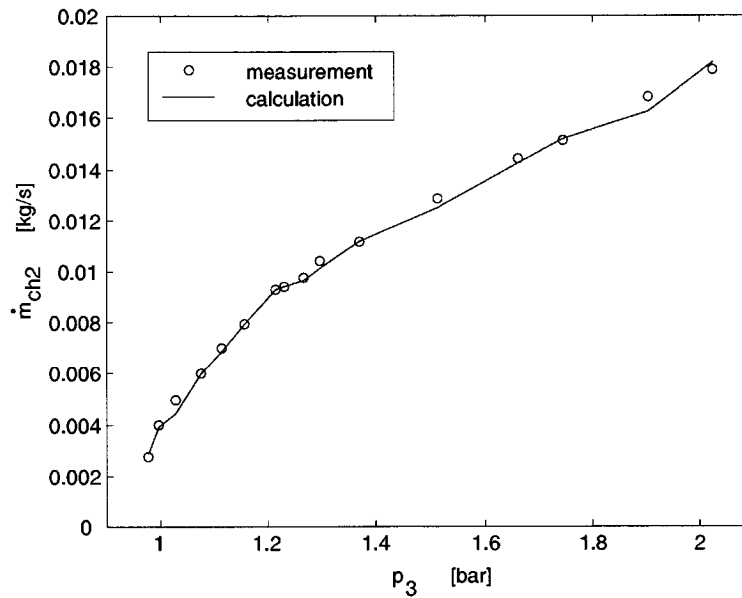
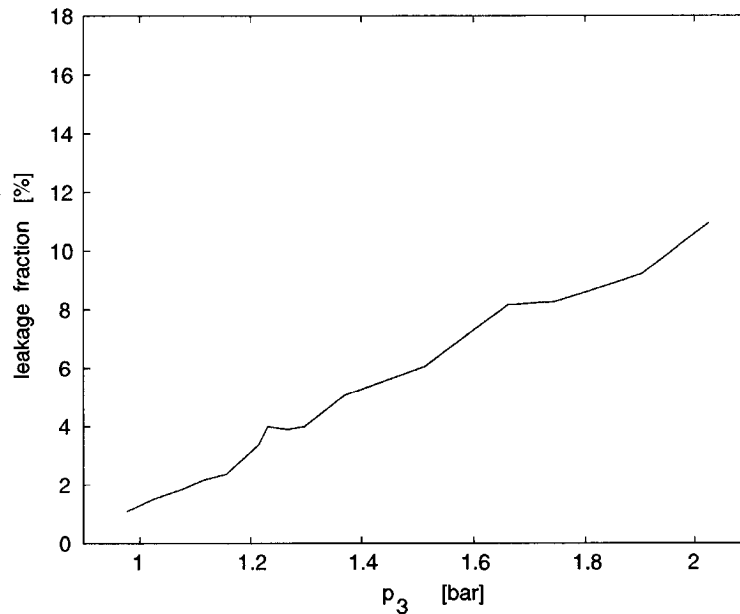**Figure 4.8:** Comparison between predicted and measured ('o') mass
flows in channel 2
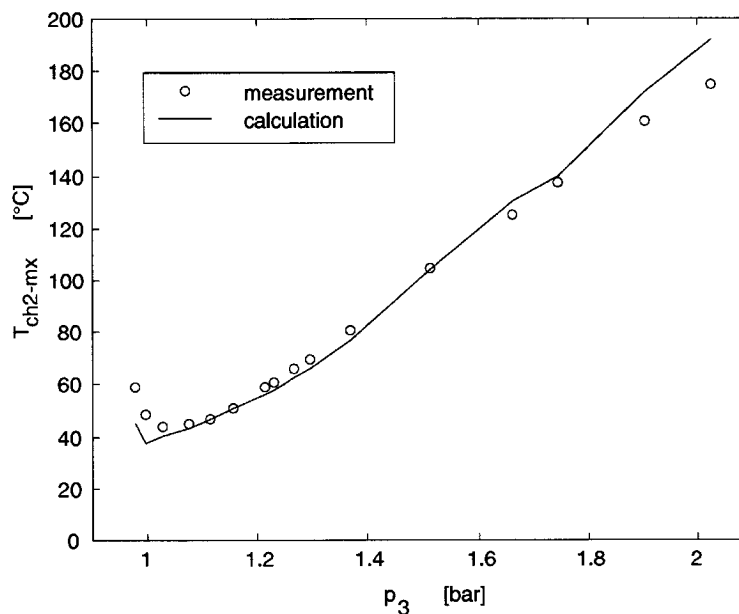
Figure 4.9: Comparison between predicted and measured ('o') mix-
ing temperature in channel 2
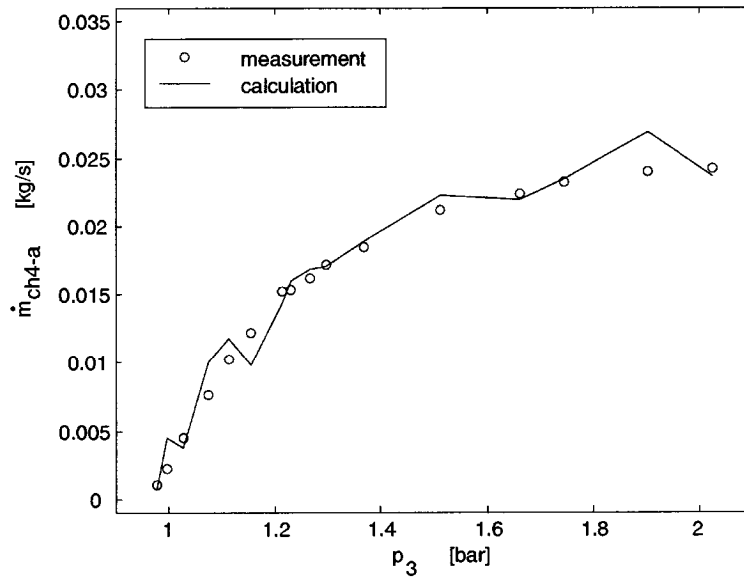
Figure 4.10: Comparison between predicted and measured ('o') scavenging air mass flow in channel 4
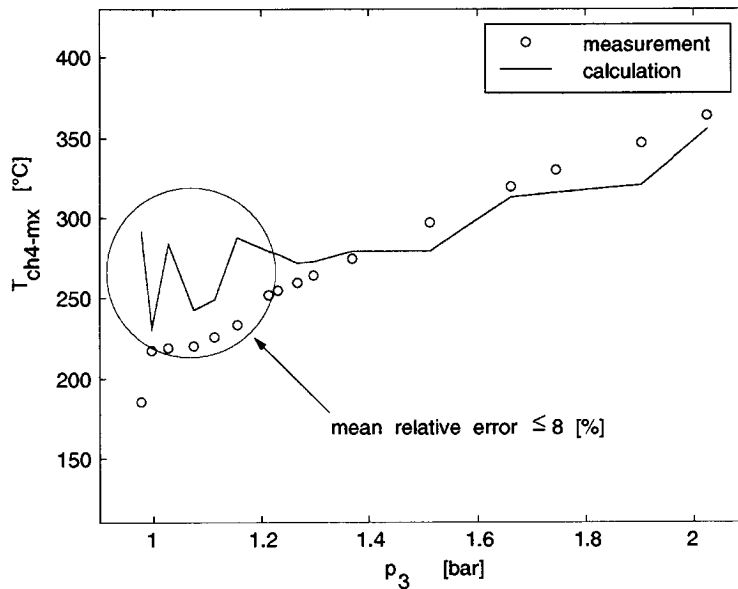
Figure 4.11: Comparison between predicted and measured ('o') mixing temperature in channel 4

Figure 4.12: Calculated leakage fraction as a result of the scavenging pressure p_z identified
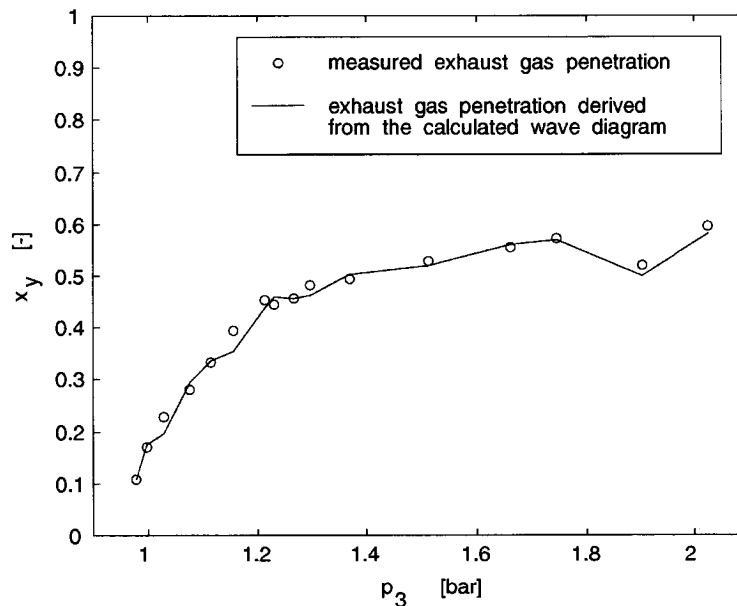
Figure 4.13: Exhaust gas penetration derived from the calculated wave diagram at location y compared with the exhaust gas penetration resulting from measurements ('o', Eq. 4.2)

Model Prediction and Measurement for Throttle no. 1 Partially Closed

In order to force steady-state EGR the pressure p_1 and therefore the scavenging energy (Eq. 2.2) are lowered by closing the throttle no. 1. Up to a certain closing position of the throttle no. 1 (in this case approximately 79%) the engine still operates in stationary mode, see Fig. 4.14 and 4.15. Above this certain limit, the engine torque breaks down completely as a result of the misfiring. The measurement data in Fig. 4.14 point out clearly that a value of the air-to-fuel ratio in channel 4 which is larger than 1.0 does not indicate zero steady-state EGR. This fact results from the mixing zone in the cell wheel.

The following list explains at which engine operating conditions EGR is forced and why the calculation of the scavenging process needs a sensitivity analysis. It then discusses the model results which are graphically presented on the following pages.

- **Forced EGR**: The pressure p_1 is lowered with throttle no. 1 at three constant GPV positions, namely for 40%, 50%, and 60% closing positions. The scavenging energy is lower due to the lowered p_1 and forces steady-state EGR. Due to the mixing zone, some scavenging air still exists in channel 4, but it decreases with a lower p_1.

- **Sensitivity of Scavenging Process**: The model of the *low pressure part* predicts the scavenging air mass flow for the boundary condition with a lowered p_1 with a relative error on the order of 10%, see Fig. 4.16. The relative error is higher compared to the case with fully open throttle no. 1 because of the sensitivity of the calculated scavenging process to the measured input data, such as pressure p_1 and p_4. The sensitivity of the state x on the low pressure difference is (Guzzella (1995)):

$$S_{\mathrm{x}} := \frac{\Delta x / x}{\Delta(p_4 - p_1)/(p_4 - p_1)} \qquad (4.3)$$

Even a small measurement error of the pressures p_1 and p_4 causes a significant error increase. Therefore, the calculation of the scavenging air mass flow and of the EGR rate is done in two different ways:

1. Calculation of the model outputs $\dot{m}_{ch4-a}$ and x_{egr} as a function of the measured values of p_1 and p_4, assuming no measurement error:

$$\dot{m}_{ch4-a} = f(p_{i-meas}, T_{i-meas}, n_{pws-meas})$$
$$x_{egr} = f(p_{i-meas}, T_{i-meas}, n_{pws-meas})$$

2. Calculation of the model outputs $\dot{m}_{ch4-a}$ and x_{egr} as a function of the measured values of p_1 and p_4, including a defined measurement error of 0.5%:

$$\dot{m}_{ch4-a} = f(p_{1-meas} \mp \Delta p, p_{4-meas} \pm \Delta p,$$
$$p_{i-meas}, T_{i-meas}, n_{pws-meas})$$
$$x_{egr} = f(p_{1-meas} \mp \Delta p, p_{4-meas} \pm \Delta p,$$
$$p_{i-meas}, T_{i-meas}, n_{pws-meas})$$

- **Results of Sensitivity Analysis for Forced EGR**: For the case of no measurement error the model predicts the scavenging air mass flow (Fig. 4.16) as well as the EGR rate (Fig. 4.19, 'x') quantitatively with satisfactory accuracy. When the input data is changed by a fictitious measurement error of 0.5%, the model predicts the changes of the scavenging air mass flow and of the EGR rate qualitatively correctly, see Fig. 4.18, 4.19. Therefore, the model of the scavenging process may be used for extrapolation.

- **Results of Sensitivity Analysis for Open Throttle no.1**: Also for the case of fully open throttle no. 1 the influence of a fictitious measurement error of 0.5% on the scavenging air mass flow and on the EGR rate is tested, see Fig. 4.17. The EGR rate in this case is called *natural* EGR rate since it is not forced either by the throttle no. 1 or by the rotational speed of the PWS. The model predicts both the scavenging mass flow and the natural EGR rate quantitatively (case no measurement error) and qualitatively (fictitious measurement error) with satisfactory accuracy.
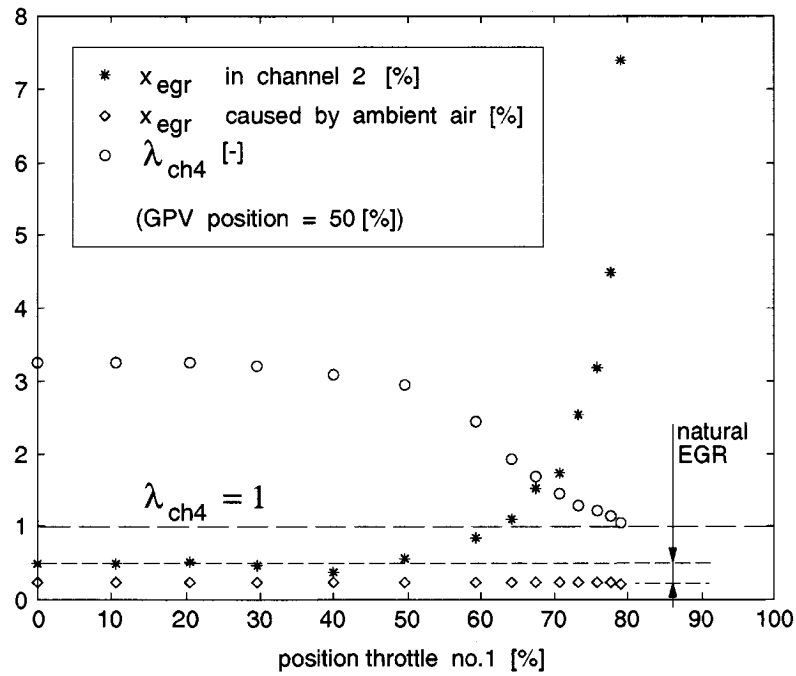
Figure 4.14: Measured air-to-fuel ratio in channel 4 (λ_{ch4}) and measured EGR rate (x_{egr}) as a function of the closing position of throttle no. 1 (GPV 50% closed)
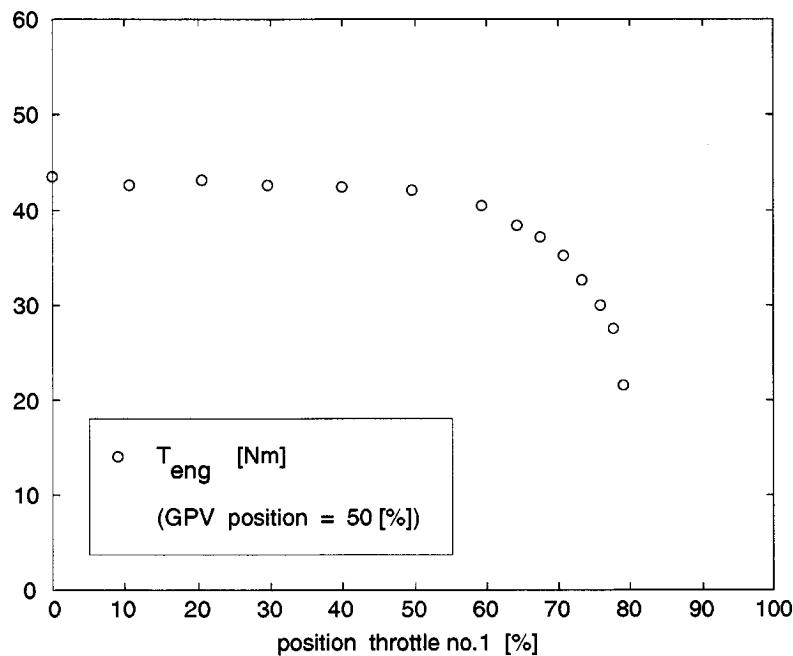
Figure 4.15: Measured engine torque as a function of the closing position of throttle no. 1 (GPV 50% closed)
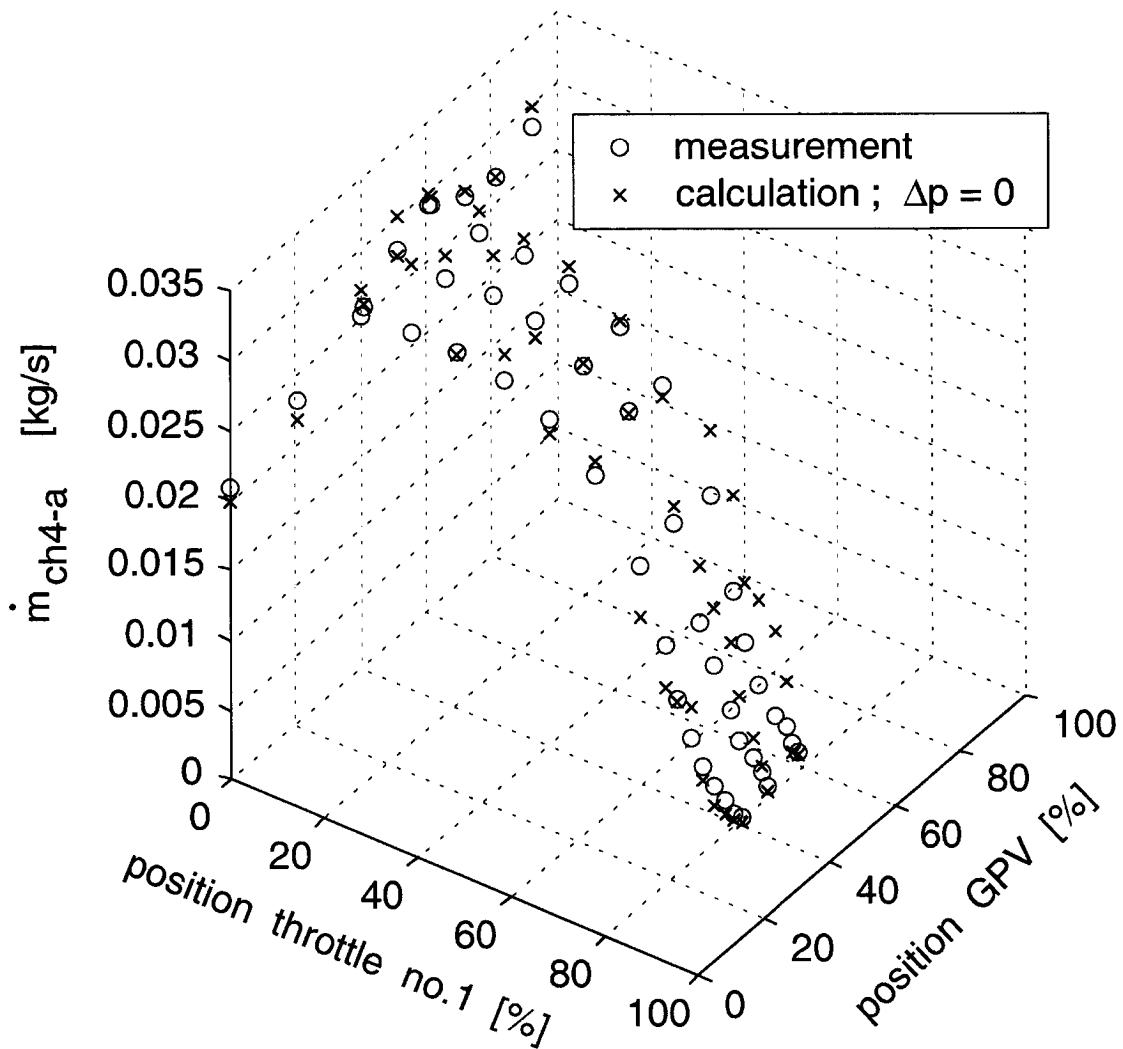
Figure 4.16: Comparison between measured ('o') and calculated ('x') scavenging air mass flow in channel 4 as a function of GPV position and position of throttle no. 1, case "zero measurement error"
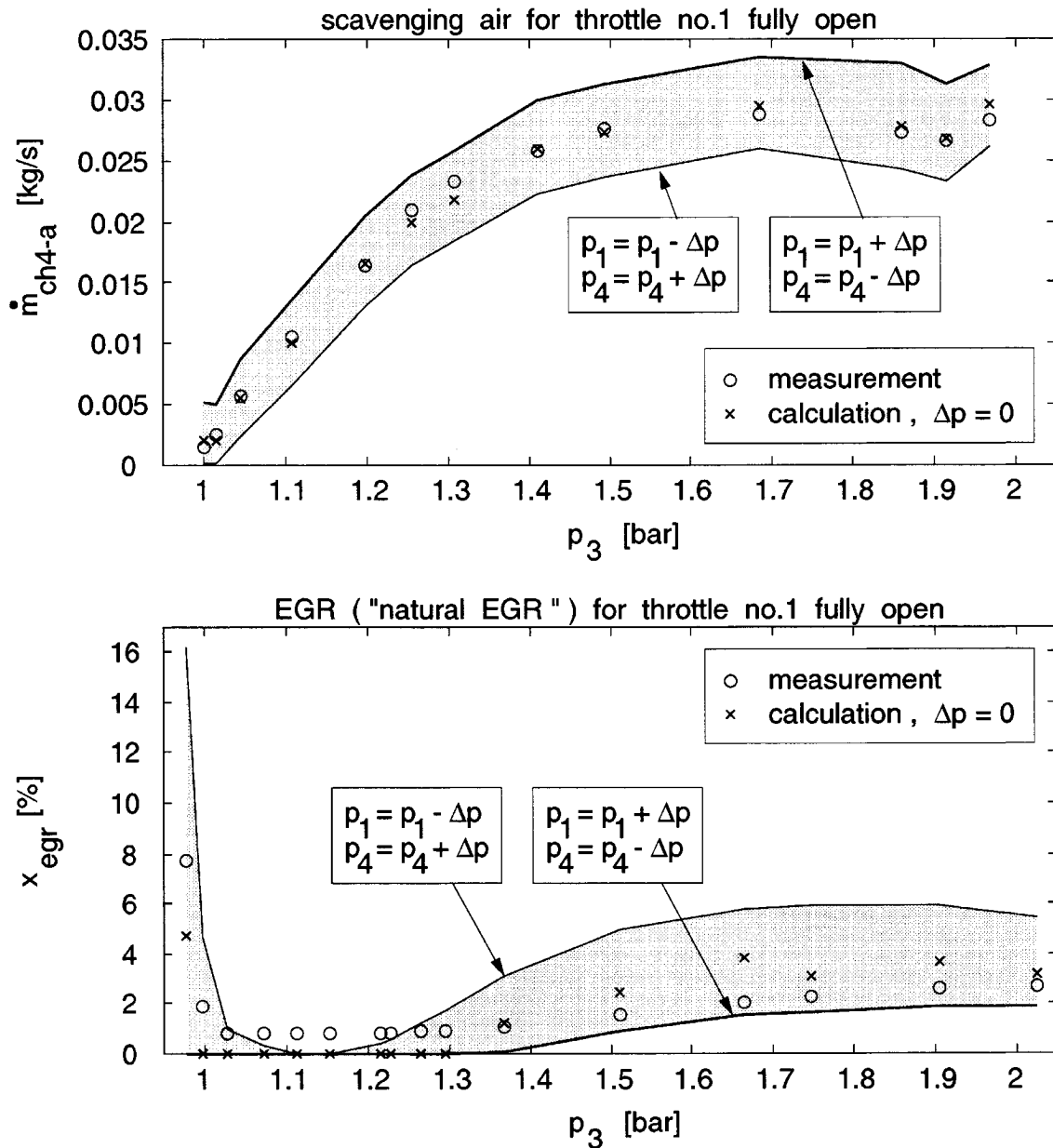
Figure 4.17: Above: sensitivity analysis of scavenging air mass flow in channel 4, '−': fictitious measurement error 0.5%; Below: sensitivity analysis of natural EGR rate in channel 2, '−': fictitious measurement error 0.5%
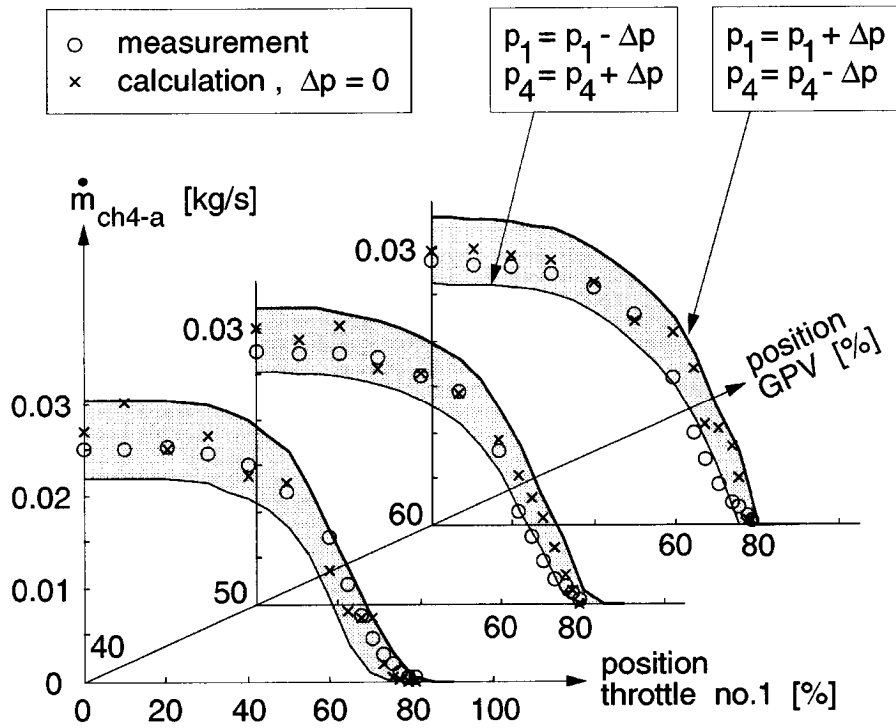
Figure 4.18: Sensitivity analysis of scavenging air mass flow in channel 4, '−': fictitious measurement error 0.5%
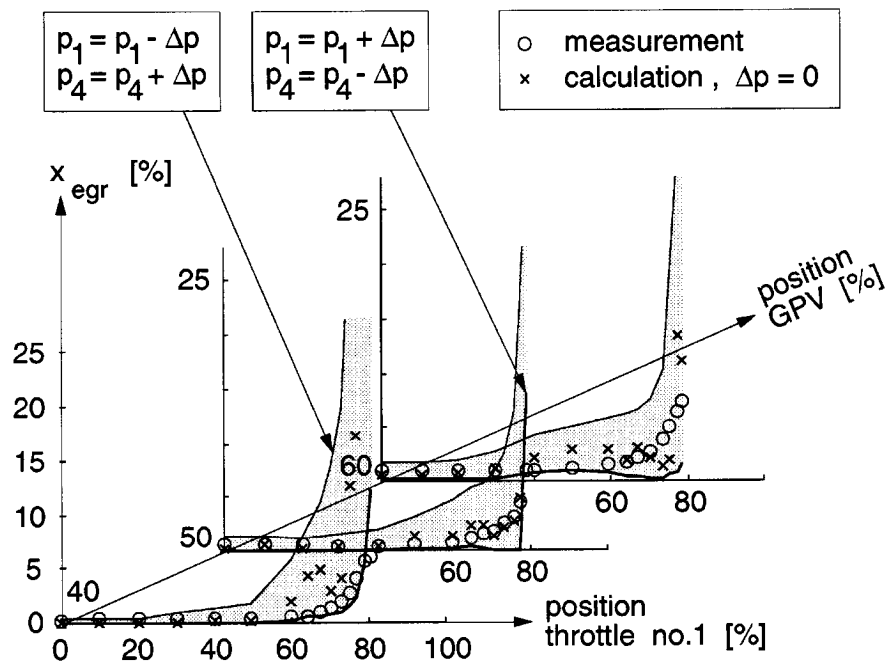
Figure 4.19: Sensitivity analysis of EGR rate in channel 2, '−': fictitious measurement error 0.5%

4.2 Validation of the *PWS Engine Model*

The first subsection describes the validation procedure of the simulation tool *PWS Engine Model* in order to guarantee a error of the simulation tool within the demanded range for steady-state and transient conditions. The second subsection shows the relative error of the validated simulation tool for steady-state conditions, whereas the third subsection compares measured and simulated state traces during load steps.

4.2.1 Principles for Dynamic Validation

Parameter Identification

After the *PWS Model* is validated it is inserted into the simulation tool *PWS Engine Model* as just one, but an important submodel. Although each submodel is already statically validated, the simulation tool *PWS Engine Model* requires a second static validation, see Fig. 4.20, since the errors of its submodels are cumulative.

The static behavior of the simulation tool is adjusted by the four steps described below:

- **Step *i)***: Identification of the **volumetric efficiency** λ_l of the SI engine for a fully closed GPV. The value of λ_l has to be adjusted at this system operating point since in this case the valve geometry and therefore the throttle coefficient of the GPV have no influence on the simulated states. The criterion for identification is the mean value of the intake manifold pressure and the gas pocket pressure, see Fig. 4.2. The reasons for choosing this criterion are, on the one hand, that the intake manifold pressure influences the pressure level of the high pressure loop "PWS-manifold2-engine-manifold3-PWS", on the other hand, that the gas pocket pressure influences the scavenging process via the pressures p_y and p_z. Thus, the errors of p_{im} and p_g have to be minimal in order to achieve a satisfactory agreement between simulated and measured state traces of the high pressure side (p_2, p_{im}, T_{eng}, p_3, p_g) as well as of the low pressure side (λ_{ch4}).

- **Step *ii)***: Identification of the **GPV throttle coefficient** for

system operating conditions with partially open GPV and fully open throttle no. 2. The resulting throttle coefficient adjusts the steady-state model behavior in the supercharged mode.
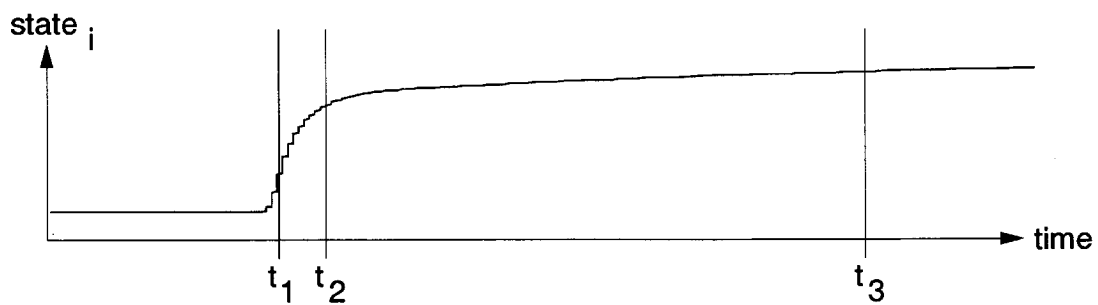
IDENTIFICATION
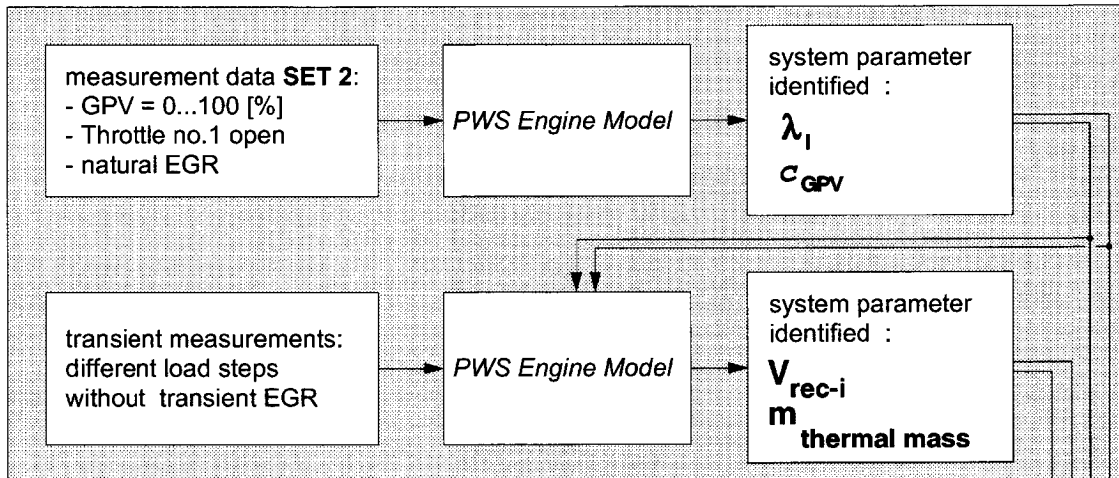
VALIDATION
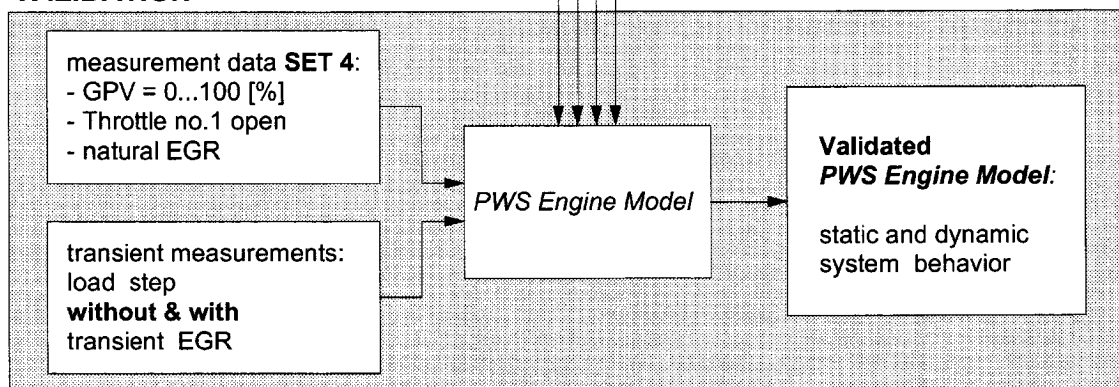
Figure 4.20: Validation principles for adjusting the steady-state and dynamic behavior of the simulation tool *PWS Engine Model*

- **Steps *iii), iv)*:** In the following two steps of identification, the dynamics of the simulation tool can be validated by adjusting the volumes of the receivers in the model. These receivers represent either the volumes of the tubes or the wall mass which

stores thermal energy. Since the measured state traces have not yet reached their steady-state value at the end of the measuring time, the two different dynamics (filling-emptying process of the tubes, energy storage in the wall) are identified by defining three individual points in the time scale in order to derive three different values of the rising state traces, see Fig. 4.2. This allows to identify the receiver volumes by variation until the simulated state traces describe the same dynamic behavior as the measured ones. The demanded model error of the transient behavior is 10%.

| step	system parameter	criterion	limits
i)	λ_l	$\min\left\{\varepsilon\left(p_{im}, p_g\right)\right\}$	$0 \le \lambda_l$
ii)	c_{GPV}	$\min\left\{\varepsilon\left(p_{im}, p_g\right)\right\}$	$0 \le c_{GPV} \le 1$
iii)	$V_{rec\text{-}i}$	$\varepsilon\left\{state_i(t_j)\right\} \le 10$ [%]	$j = 1, 2$
iv)	$m_{thermal\ mass}$	$\varepsilon\left\{state_i(t_j)\right\} \le 10$ [%]	$j = 2, 3$

Table 4.2: Above: System parameters of the simulation tool *PWS Engine Model*;
Belove: Defining three different points in time in order to validate the simulation tool *PWS Engine Model*

Model Validation

After the identification of the four system parameters described in the previous subsection, the simulation tool can be used for steady-state and transient simulations. Subsection 4.2.2 shows the relative error of the states of interest of the simulation tool *PWS Engine Model*, whereas Subsection 4.2.3 compares measured and simulated states during load steps.
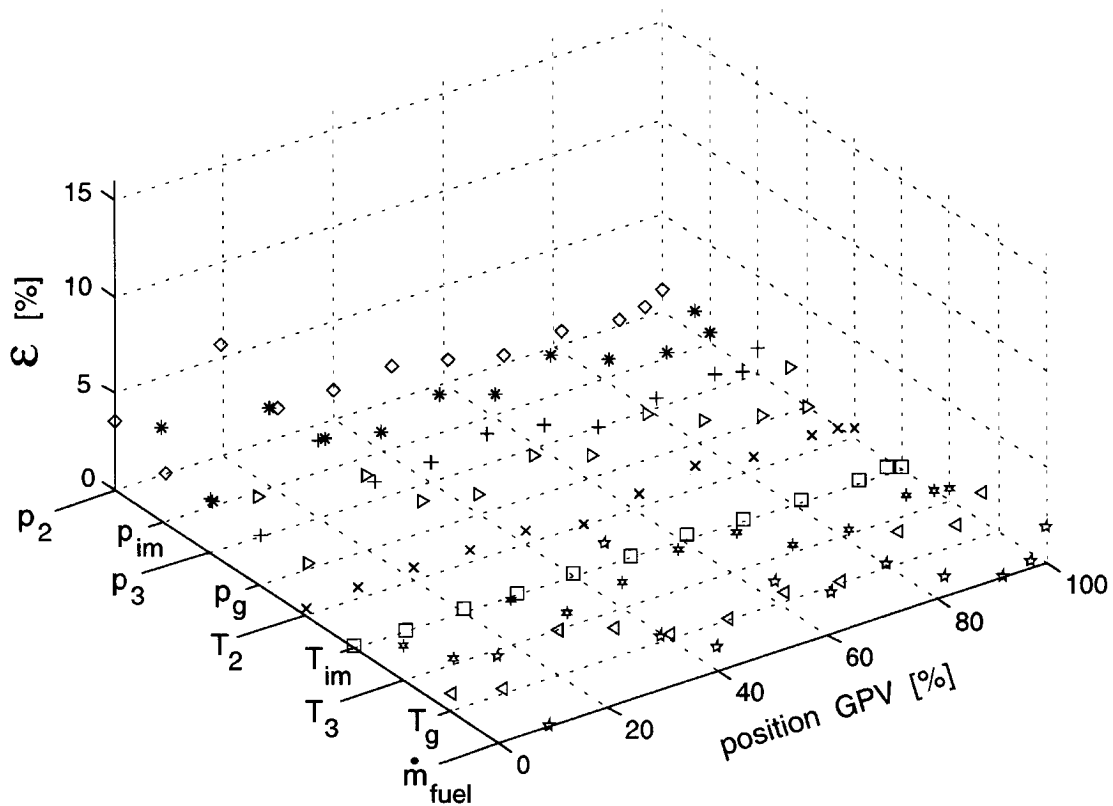
Figure 4.21: Relative errors of the states of the simulation tool *PWS Engine Model* which describe the high pressure loop of the system "PWS SI engine" and the scavenging process (influenced by p_g) for steady-state conditions

4.2.2   Static Behavior of the *PWS Engine Model*

For the static validation of the *PWS Engine Model* the states in the high pressure loop "PWS-manifold2-engine-manifold3-PWS" are of

interest because:

- The simulation of the closed loop "PWS-manifold2-engine-manifold3-PWS" can become unstable when the cumulative errors of each submodel become too high.

- The ratio between scavenging air and exhaust gases in channel 4 (λ_{ch4}) is measured during transients. Therefore, the steady-state error of this state as well has to be within the demanded range. This is easily achieved by adjusting the pressure losses in the submodel for the oxidation catalyst. As a result, this state is not observed for the steady-state validation. The state in the simulation tool which influences the scavenging process most is the gas pocket pressure. The gas pocket pressure is one state of the high pressure loop and therefore observed for the validation.

The relative error of the simulation tool for the states of interest in the high pressure loop is depicted in Fig. 4.21. The result shows that the identified volumetric efficiency λ_l and the identified GPV throttle coefficient (Appendix B) lead to a relative error for nine states on the order of 5% for steady-state conditions.

4.2.3   Dynamic Behavior of the *PWS Engine Model*

Measured States During Load Steps

During a transient only those states of a system can be measured that have sensors whose dynamics are faster than the observed dynamics of the state. Therefore, in the following subsection no simulated temperatures are compared with measured ones since the dynamics of the temperature sensors are too slow. The following states are measured during transients:

– pressures	:	p_2, p_{im}, p_3, p_g
– torque	:	T_{eng}
– rotational speeds	:	n_{eng}, n_{pws}
– air-to-fuel ratio	:	λ_{ch4}
– valve positions	:	pos_{th1}, pos_{th2}, pos_{GPV}

Inputs for the Simulation Tool During Load Steps

The measurements show that the following input variables can be assumed to be constant:

- rotational speeds   : n_{eng}, n_{pws}
- valve position   : pos_{th1}

As a result, the only input data of the simulation tool *PWS Engine Model* required to simulate transient phenomena are the measured states:

- Position of throttle no. 2 : $pos_{\text{th2}} = pos_{\text{th2}}(t)$

- Position of GPV : $pos_{\text{GPV}} = pos_{\text{GPV}}(t)$

In the following two subsections, the simulation tool is tested for two different load steps:

1. Load step **without** transient EGR: the throttle no. 2 is fully open, the GPV is closed from 50% to 100%.

2. Load step **with** transient EGR: the throttle no. 2 is opened from 25% to 100%, afterwards the GPV is closed from 0% to 100%.

1. Load Step Without Transient EGR

Measured and predicted state traces for closing the GPV from 50% to 100% are compared in Fig. 4.23 – 4.26 and discussed in the following list:

- **Input Data**: Before the load step, the system "PWS SI engine" operates in a stationary, slightly supercharged mode. At the time of the load step, the throttle no. 2 remains open, see Fig. 4.22, and the GPV is closed as fast as possible, i.e., the closing time is limited by the hardware rather than by the control parameters of the position controller.

- **Engine Torque Response**: The sudden rise of the engine torque indicates no transient EGR, see Fig. 4.23, due to the gas pocket pressure which remains sufficiently high even during the closing time of the GPV. In the case of zero EGR the simulated engine torque shows qualitatively the same behavior as the pressure in the intake manifold, because a rising p_{im} results in

an increasing fuel mass flow which again leads to a rising torque (see Eq. 3.124, Chap. 3).

- **Response of** λ_{ch4} : Due to the gas pocket pressure drop the value of λ_{ch4} decreases during the load step, see Fig. 4.24. The error of the simulated value of λ_{ch4} before and after the load step is on the order of 1% due to the small error of the simulated gas pocket pressure.

- **Pressure Response**: The simulated pressure traces describe the dynamics determined by the filling-emptying process of the manifolds (fast dynamics, τ_{rec}, Meisner and Sorenson (1986)) and the energy storage in the wall of the outlet system (slow dynamics, $\tau_{thermal\,mass}$) with satisfactory accuracy, see Fig. 4.25 and 4.26. The model assumes one zone for the heat storage in the walls of the outlet system (Baker and Assanis (1997), Liu et al. (1995)). During an acceleration, this mass has to be heated up until it is in balance with the fluid and the ambient temperatures. The states reach their equilibriums after approximately 6 ... 10 minutes.

- **Gas Pocket Pressure Dynamics**: The undershoot of the gas pocket pressure trace in Fig. 4.25 results from closing the GPV which is the valve upstream of p_g. The first period during the closing time, called *out*, is characterized by a deficit between in- and outflowing masses, see Fig. 4.27 and 4.28:

$$\dot{m}_{gpv} < \dot{m}_{chg} \quad : \text{part } out$$

Then, the second period, called *in*, starts, during which the gas pocket pressure rises due to the amount of inflowing mass:

$$\dot{m}_{gpv} > \dot{m}_{chg} \quad : \text{part } in$$

At the point where the values of the three pressures p_x, p_g, and p_y are approximately equal, backflow out of the cell wheel starts:

$$\left. \begin{array}{l} \dot{m}_{gpv} \equiv 0 \\ \dot{m}_{chg} > 0 \end{array} \right\} \quad \text{part } backflow$$

Backflow ends when the entire system "PWS SI engine" is at its thermal equilibrium. From the point of thermal equilibrium,

the gas pocket pressure p_g, the pressure p_x, and the pressure p_y are equal. Therefore, the waves $s4$, $(e4 - bf)$, $s5$, and $e4$ do not exist anymore:
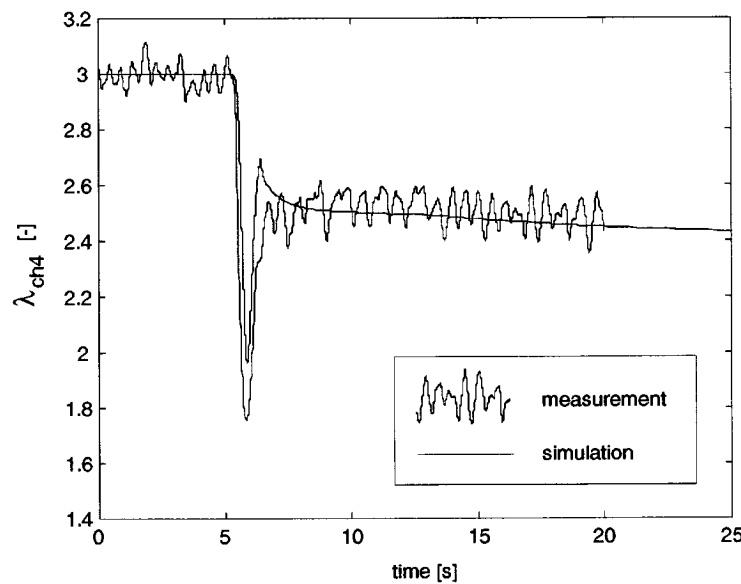
$$\left.\begin{array}{l} \text{GPV closed} \\ \text{Thermal equilibrium of "PWS SI engine"} \end{array}\right\} \Leftrightarrow p_g \equiv p_x \equiv p_y$$
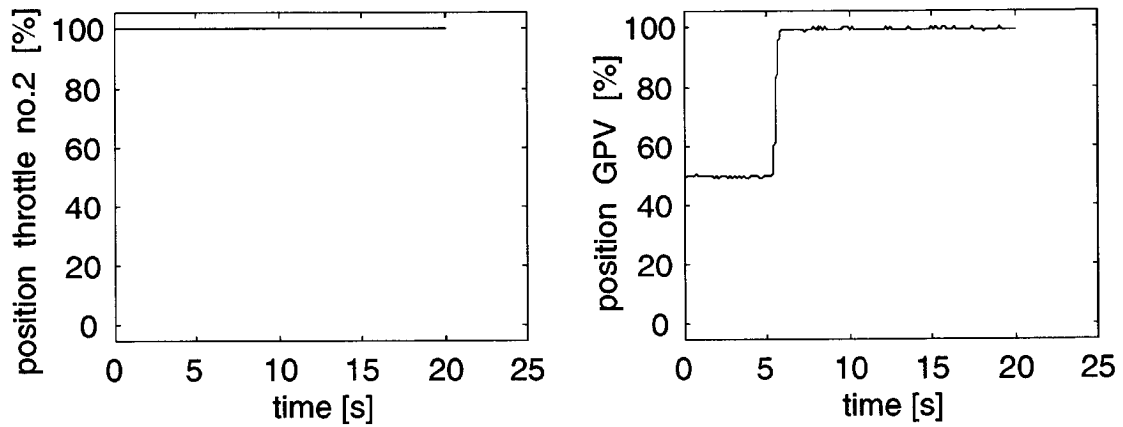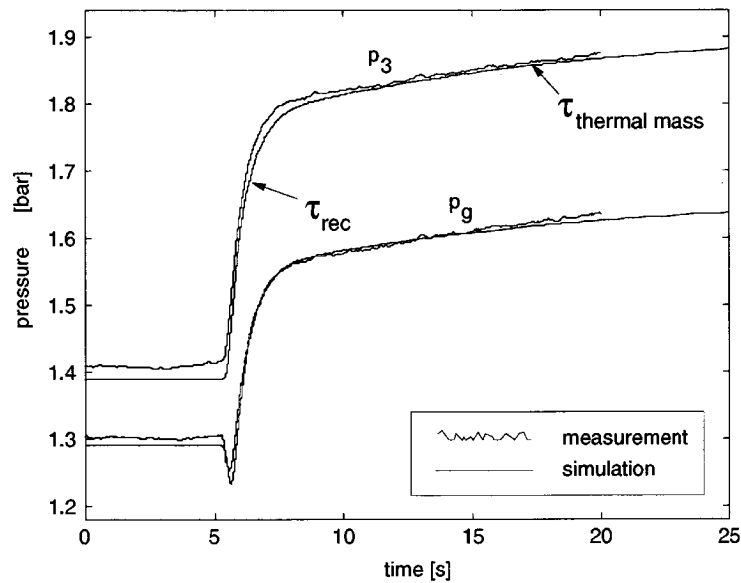

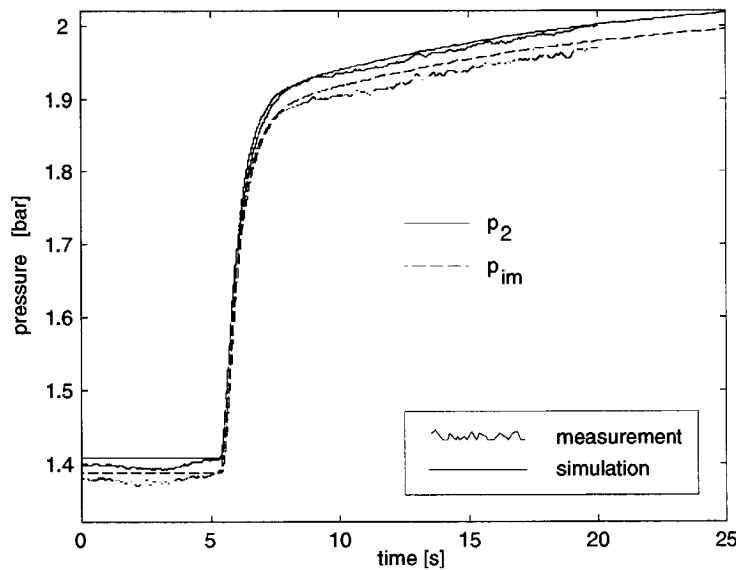**Figure 4.22:** Load step without transient EGR: measured positions of throttle no. 2 and of GPV
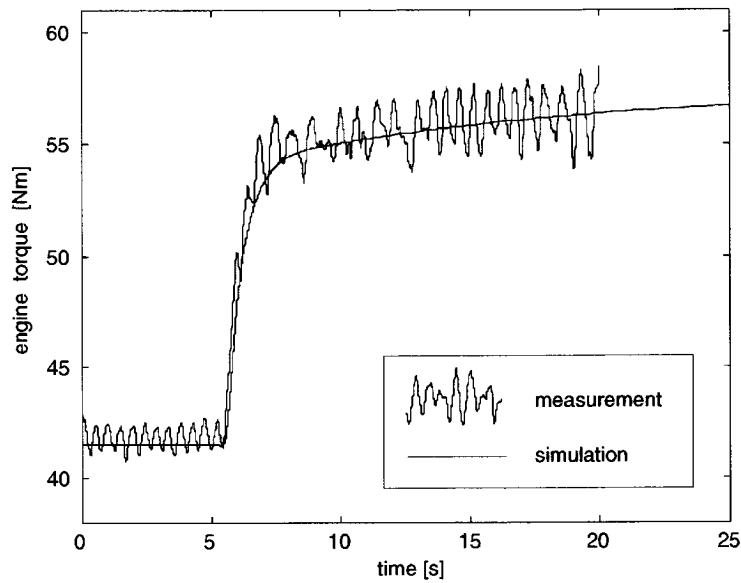
Figure 4.23: Load step without transient EGR: measured and simulated engine torques (measurement from 0 to 20 s, simulation from 0 to 25 s)
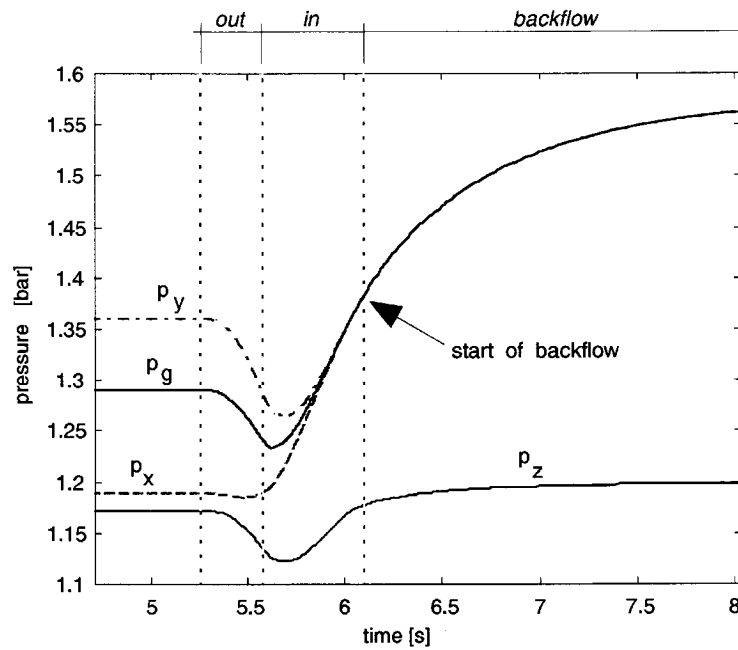

Figure 4.24: Load step without transient EGR: measured and simulated λ_{ch4} in channel 4 (measurement from 0 to 20 s, simulation from 0 to 25 s)
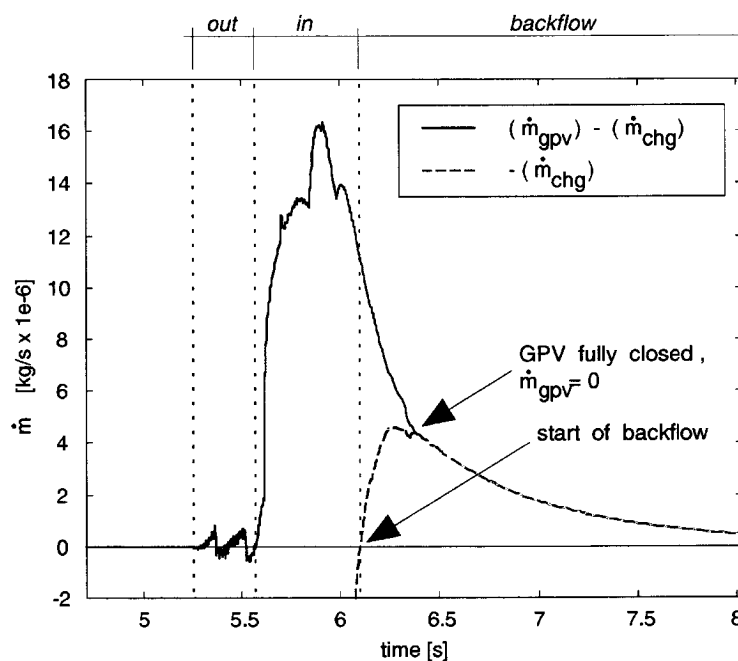
Figure 4.25: Load step without transient EGR: measured and simulated pressures in the gas pocket and in channel 3 (measurement from 0 to 20 s, simulation from 0 to 25 s)

Figure 4.26: Load step without transient EGR: measured and simulated pressures in channel 2 and in intake manifold (measurement from 0 to 20 s, simulation from 0 to 25 s)

Figure 4.27: Load step without transient EGR: simulated pressure in the gas pocket, simulated pressures in fields x, y, and z, time scale enlarged
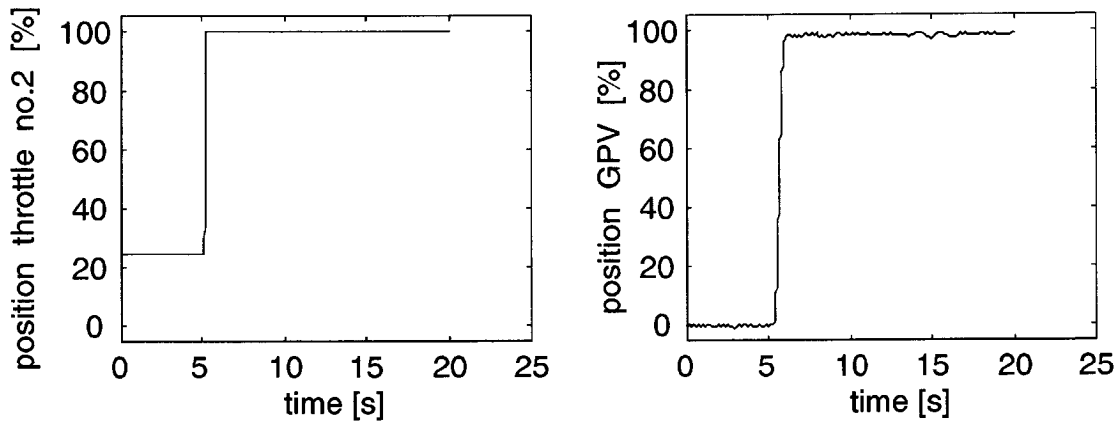

Figure 4.28: Load step without transient EGR: simulated mass balance in the gas pocket receiver, time scale enlarged
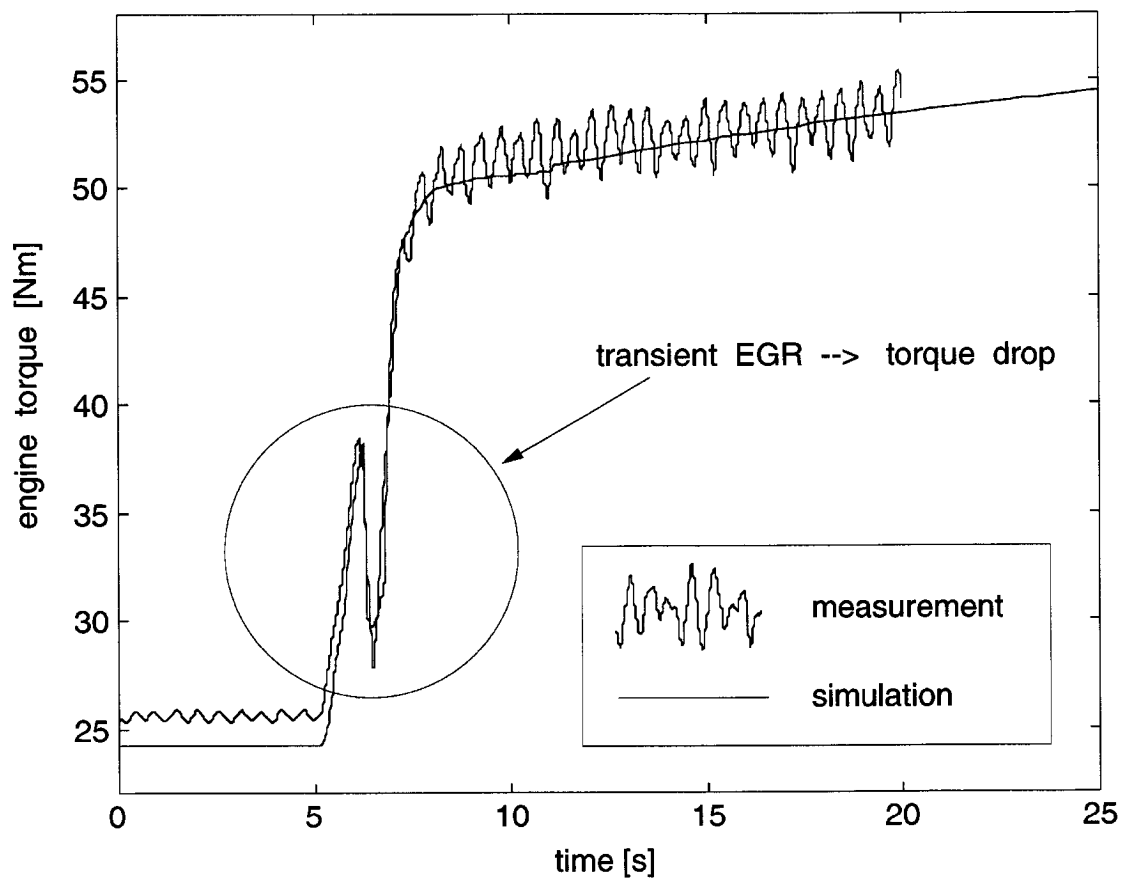
2. Load Step With Transient EGR

In order to force a transient EGR event, the load step has to be increased by starting from a slightly throttled engine operating point. The comparison between measured and predicted state traces for the enlarged load step is depicted in Fig. 4.30 – 4.33. The important effects are pointed out in the list below:

- **Input Data**: Before the load step, the system "PWS SI engine" operates in stationary surge mode (throttle no. 2 partially closed). At the time of the load step, the throttle no. 2 first is opened from 25% to 100%, afterwards, the GPV is closed from 0% to 100%, see Fig. 4.29.

- **Engine Torque Response**: Due to the larger load step, the pressure in the gas pocket drops lower than to the load step without transient EGR, see Fig. 4.25 and 4.32. Consequently, for a short time the scavenging energy is not sufficient for complete scavenging, which is indicated by the stronger decrease of λ_{ch4} compared to the case without transient EGR, see Fig. 4.31. Since the engine aspirates not only compressed fresh air, but also recirculated exhaust gases, the amount of free oxygen in the cylinder decreases. Less gasoline can oxidize, the engine torque drops. Thus, the measured torque drop proves that transient EGR occurs, see Fig. 4.30. The model predicts an EGR rate of approximately 25%, see Fig. 4.34, which causes the simulated torque drop. After the short time of insufficient scavenging energy, the EGR rate decreases almost to zero and the process of the entire high pressure loop recovers from the transient EGR event.

- **Response of** λ_{ch4}: The error of the simulated value of λ_{ch4} after the load step is due to the gas pocket pressure error on the order of 5%, see Fig. 4.32.

- **Pressure Response**: During this load step, not only the gas pocket pressure shows an undershoot, but also the pressure p_2, see Fig. 4.33. The pressure p_2 describes the pressure in the receiver upstream of the throttle no. 2, which is suddenly opened. Thus, the pressure first has to drop.
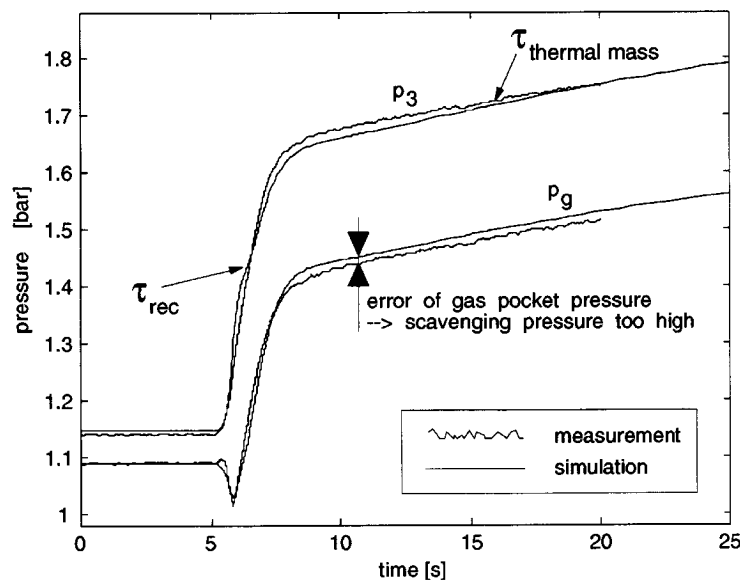
Figure 4.29: Load step with transient EGR: measured positions of throttle no. 2 and of GPV

Figure 4.30: Load step with transient EGR: measured and simulated engine torques (measurement from 0 to 20 s, simulation from 0 to 25 s)
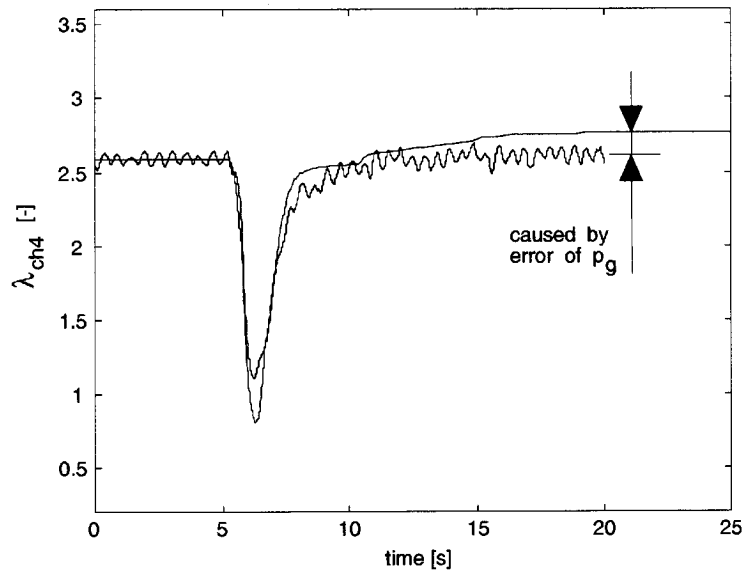
Figure 4.31: Load step with transient EGR: measured and simulated λ_{ch4} in channel 4 (measurement from 0 to 20 s, simulation from 0 to 25 s)

Figure 4.32: Load step with transient EGR: measured and simulated pressures in the gas pocket and in channel 3 (measurement from 0 to 20 s, simulation from 0 to 25 s)
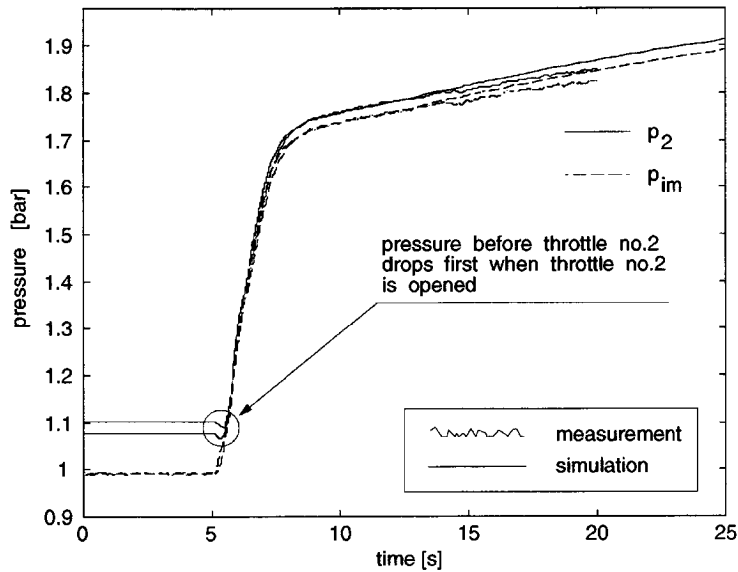
Figure 4.33: Load step with transient EGR: measured and simulated pressures in channel 2 and in intake manifold (measurement from 0 to 20 s, simulation from 0 to 25 s)
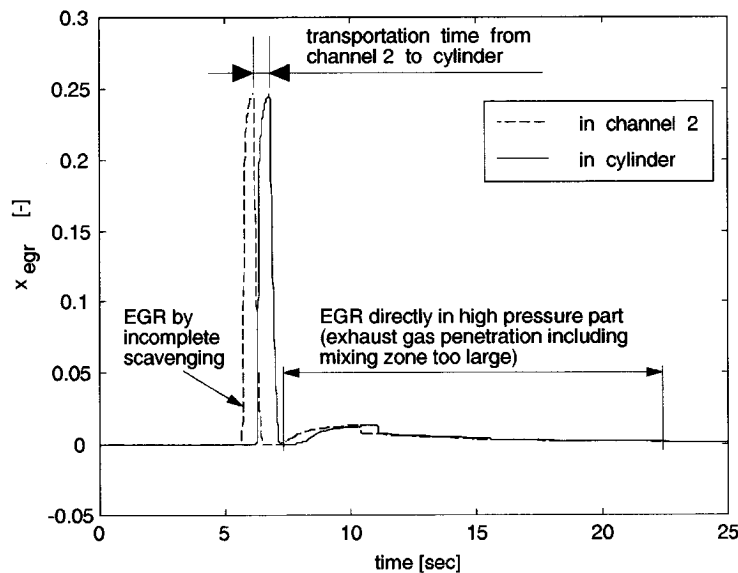
Figure 4.34: Load step with transient EGR: simulated EGR rates in channel 2 and in the cylinder (measurement from 0 to 20 s, simulation from 0 to 25 s)

4.3   Summary of Chapter 4

The Chapter 4 describes all the steps of model parameter identification necessary to obtain a simulation tool *PWS Engine Model* which allows to simulate state changes during load steps without and with transient EGR with a demanded accuracy. These steps are:

1. Identification of the model parameters

$$\eta_c, \quad \eta_r, \quad p_z, \quad \text{and } mz,$$

   of the static *PWS Model*.

2. Connecting the validated *PWS Model* as a submodel to the simulation tool *PWS Engine Model*.

3. Identification of the system parameters

$$\lambda_l \quad \text{and} \quad c_{GPV}$$

   of the dynamic *PWS Engine Model* in order to guarantee that the error of the static behavior of the simulation tool does not exceed 5%.

4. Identification of the system parameters

$$V_{rec-i} \quad \text{and} \quad m_{thermal\,mass}$$

   of the dynamic *PWS Engine Model* in order to validate its dynamic behavior.

The resulting simulation tool includes the *PWS Model*, whose typical error is on the order of 5%. It has been shown that the statically and dynamically validated simulation tool *PWS Engine Model* shows a static error over nine states which is smaller than 5% and an error during load steps that is smaller than 10%.

Chapter 5

Model Extrapolation

The previous chapter pointed out clearly why the gas pocket pressure has to drop for a short time when the gas pocket valve (GPV) is closed during a load step. Depending on the amount of the gas pocket pressure drop, the scavenging process is either only slightly deteriorated, i.e., scavenging air mass flow decreases, but transient exhaust gas recirculation (EGR) does not occur, or the scavenging of the cell wheel is incomplete and transient EGR results. As a result, the torque of the SI engine breaks down and rises again when due to the increasing pressure level of the system "PWS SI engine" the scavenging process is complete again. In order to guarantee good driveability transient EGR thus must be avoided. In the following two principles of avoiding transient EGR are investigated.

5.1 Avoiding Transient EGR

The first subsection formulates two ideas for avoiding transient EGR. The Subsections 5.1.2 and 5.1.3 investigate these two ideas by simulation. The Subsection 5.1.4 recapitulates the simulation results and defines how transient EGR can be avoided optimally.

5.1.1   Two Principles of Avoiding Transient EGR

The target is to ensure zero EGR either for stationary or transient engine operating conditions. As explained in Chapter. 3 steady-state EGR can be avoided by *i)* correctly dimensioning the PWS cell wheel to the expected exhaust gas volume flow and *ii)* adjusting the rotational speed of the PWS to the thermodynamic state in channel 3. If transient EGR during a load step has to be avoided, the scavenging energy

$$e_{\mathrm{sc}} \propto \frac{p_{\mathrm{z}}}{p_4 - p_1} \tag{5.1}$$

must be guaranteed to be as high as possible. Assuming that the hardware of the system remains the same, e.g., no additional pump is installed, the values of the pressures p_1 and p_4 are defined by the system. Thus, the scavenging energy can only be influenced by the pressure p_{z}. Since this state of the PWS cannot be influenced directly by an actuator, one has to find a solution of the problem of how p_{z} can be "controlled" indirectly.

According to Chap. 4, the scavenging pressure is defined via the pressure p_{y} by the pressure in the gas pocket p_{g}. Hence, the gas pocket pressure must be controlled in such a way that the scavenging energy is always sufficient for complete scavenging, i.e., a minimum value of the gas pocket pressure during a load step must be ensured.

Lowering the gas pocket pressure drop during load steps can be achieved by:

- Enlarging the gas pocket receiver volume.

- Increasing the minimum GPV closing time.

The impact of these two ideas on the scavenging process is investigated in the following two subsections, where the simulations are to be understood as a sensitivity analysis since the model is computed with extrapolated system parameters.

5.1.2 Influence of Gas Pocket Receiver Volume on Scavenging Process

The idea of avoiding transient EGR tested in this subsection is:

- Lower the gas pocket pressure drop during a load step by enlarging the gas pocket receiver.

This can be realized by placing the GPV nearer to the outlet valve of the SI engine. The resulting volume of the tube from the GPV to the channel g of the PWS then is increased approximately 33 times (case *big*). In order to extend the investigation of the influence of the receiver volume on the scavenging process, also the case for a smaller gas pocket receiver volume is computed (case *small*). The simulation results of these two cases are compared with the results for the actual receiver volume (case *nominal*).

Supposing a constant GPV closing time, the expected pressure drop of the gas pocket pressure with the enlarged receiver volume should be smaller than for the case *nominal* because in this model approach the state p_g describes a mean value of a system of first order, see Eq. 3.125, 3.126, and 3.127.

The simulation tool *PWS Engine Model* simulates the load step where the GPV is closed from 50% to 100%. Using the measured position of the GPV of this load step as the only input of the simulation tool, the following three cases are computed:

1. $V_{g-calc} = V_{g-meas}$: case *nominal*

2. $V_{g-calc} = V_{e-meas} + V_{3-meas} \approx 33 \cdot V_{g-meas}$: case *big*

3. $V_{g-calc} = 0.20 \cdot V_{g-meas}$: case *small*

Although the volume of the gas pocket receiver has been changed dramatically, the change of the gas pocket pressure drop is negligible, compare the simulated pressure traces in Fig. 5.1 for the three cases *nominal*, *big*, and *small*. This simulation result can be explained as follows:

- the time derivative of the perfect gas law is:

$$\frac{dp_g}{dt} = \left(\frac{dm_g}{dt} \cdot T_g + m_g \cdot \frac{dT_g}{dt}\right) \frac{R}{V_g} \qquad (5.2)$$

- the simulation for the measured GPV closing time shows (see Fig. 5.3):

$$\frac{dm_{\mathrm{g}}}{dt} >> \frac{dT_{\mathrm{g}}}{dt} \tag{5.3}$$

- which leads to the following approximation:

$$\frac{dp_{\mathrm{g}}}{dt} \sim \frac{dm_{\mathrm{g}}/dt}{V_{\mathrm{g}}} \tag{5.4}$$

As a result, the dynamics of the gas pocket pressure (dp_{g}/dt) in a first approximation are independent of the receiver volume because an increased volume also leads to a higher value of dm_{g}/dt. The rather long GPV closing time has the main influence on the gas pocket pressure dynamics.
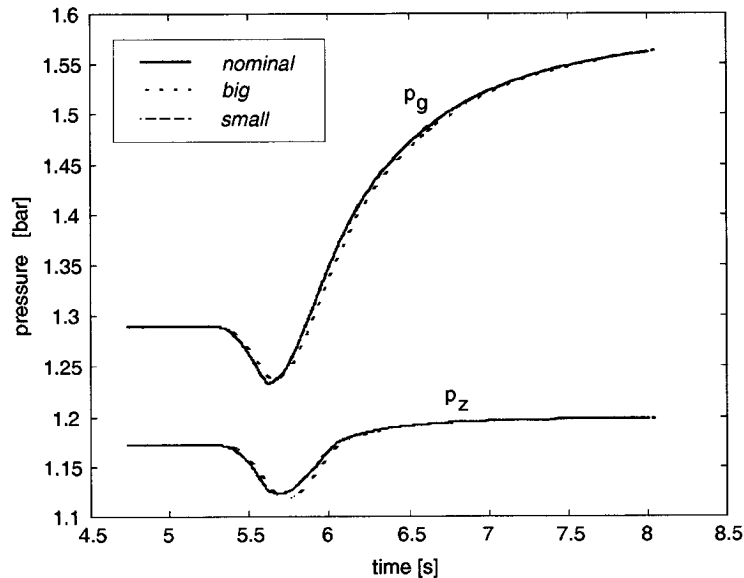
Figure 5.1: Simulated pressure in the gas pocket receiver and simulated scavenging pressure (p_{z}) for three different values of the gas pocket volume

The simulation of the variation of the receiver volume shows that placing the GPV nearer to the engine outlet valve cannot improve the scavenging condition during a load step.
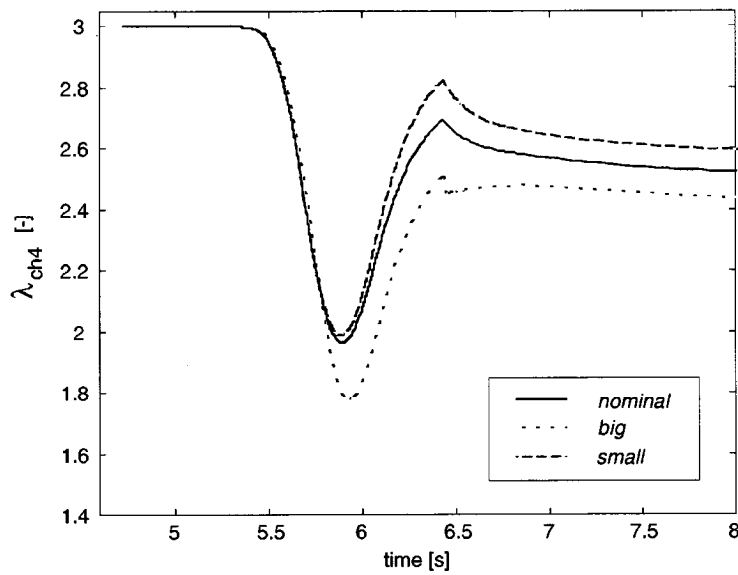
Figure 5.2: Simulated state λ_{ch4} for three different values of the gas pocket volume
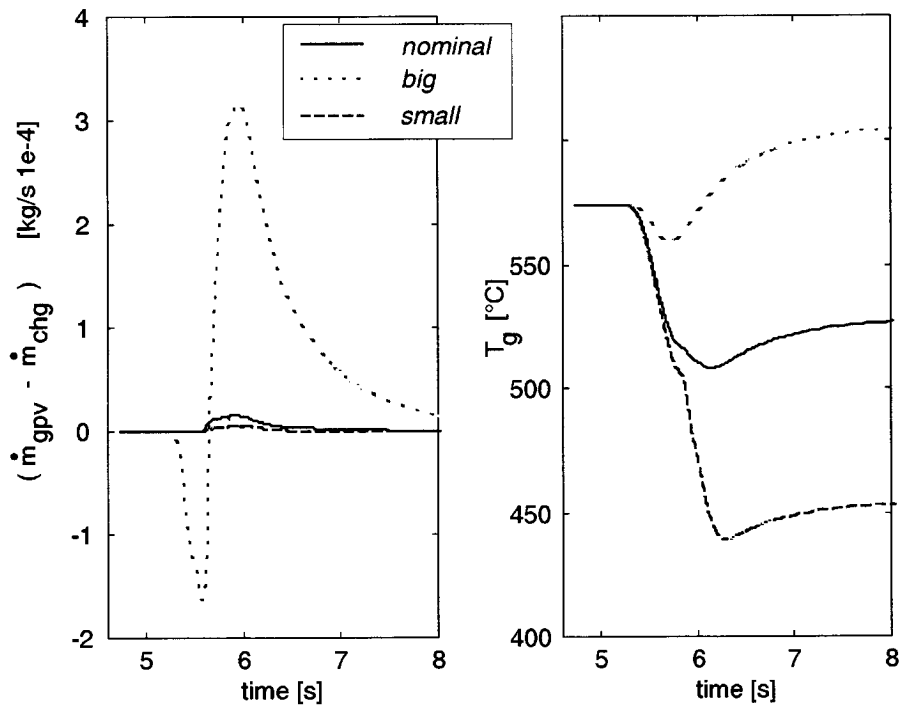
Figure 5.3: Left: simulated change of mass flow in the receiver g; Right: simulated change of temperature in the receiver g; both simulated states for three different values of the gas pocket volume

The slightly deteriorated scavenging process (Fig. 5.2) for the case *big* is the result of the increased time of the equalizing process of the two pressures p_g and p_x. Due to the sensitivity of the calculated state p_z on the calculated scavenging process, the change of λ_{ch4} in the case *big* is within the model error and therefore not relevant.

Due to the negligible influence of the gas pocket receiver volume on the scavenging process for the given GPV closing time this variant only has the drawback that it can only be realized by changing hardware.

5.1.3   Influence of GPV Closing Time on Scavenging Process

The idea of avoiding transient EGR tested in this subsection is:

- Limit the minimum closing time of the gas pocket valve (GPV).

When the GPV is closed more slowly (case *slow*) than measured (case *nominal*) the gas pocket pressure drop is expected to decrease for the following reason: During a load step the pressures in the high pressure loop "PWS–Engine–PWS" increase. The rising pressure p_3 as the pressure "upstream" of the GPV and the decreasing pressure p_g as the pressure "downstream" force the mass flow through the GVP. This mass flow equalizes the pressure difference over the GPV. When the GPV is closed slowly, the dynamics of the equalizing process are faster than the dynamics of the gas pocket valve position. Even during the closing time $(t_{cl}(GPV))$ the pressure ratio over the throttle GPV is close to its stationary value. In contrast, when the GPV is closed fast, the equalizing process is slow relative to the dynamics of the GPV position. The pressure ratio over the throttle GPV differs from its stationary value during the closing time. The gas pocket pressure drops lower than in the *nominal* case.

For these reasons the gas pocket pressure is expected not to drop as low when the minimum GPV closing time is higher. Additionally, the closing time is also decreased in order to simulate the influence of the faster GPV dynamics on the scavenging process (case *fast*).

The simulation tool *PWS Engine Model* simulates the load step where the GPV is closed from 50% to 100% for three different closing

times and always with the same constant volume of the gas pocket receiver:

1. $t_{\text{cl-calc}}(GPV) = t_{\text{cl-meas}}(GPV) + 0.0\,[s]$: case *nominal*

2. $t_{\text{cl-calc}}(GPV) = t_{\text{cl-meas}}(GPV) + 1.0\,[s]$: case *slow*

3. $t_{\text{cl-calc}}(GPV) = t_{\text{cl-meas}}(GPV) - 1.0\,[s]$: case *fast*
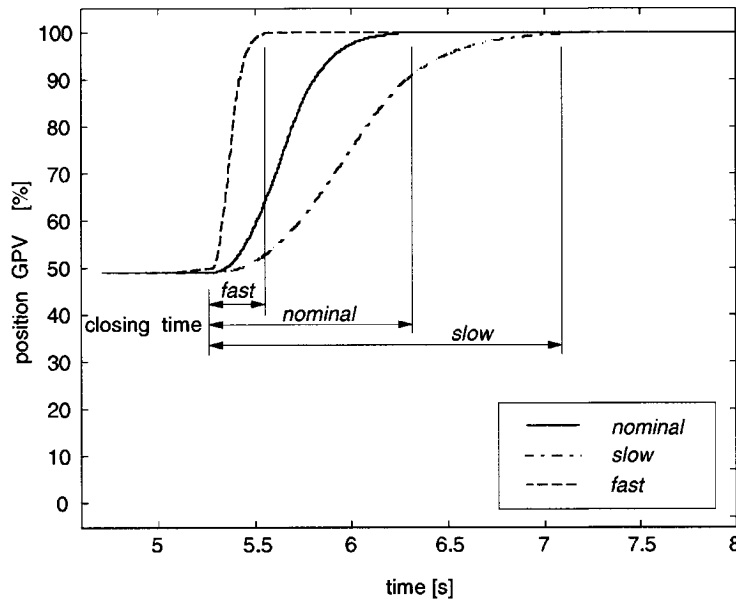
Figure 5.4: The position of the GPV as the input of the simulation tool *PWS Engine Model* for three different GPV closing times

The influence of the minimum GPV closing time on the simulated gas pocket pressure is depicted in Fig. 5.5. In contrast to the variant of changing the gas pocket receiver volume, the minimum GPV closing time has a strong influence on the gas pocket pressure drop and via the scavenging pressure p_z on the scavenging process, see Fig. 5.6.

When the GPV is closed fast (case *fast*), the pressures in the gas pocket and in the field z in the wave diagram drop lower than in the case *nominal* and thus force a decreasing scavenging air mass flow in channel 4. However, a value of λ_{ch4} which is higher than one does not indicate zero EGR due to the mixing zone in channel 4. The minimum value of λ_{ch4} where the natural EGR rate is in the tolerable
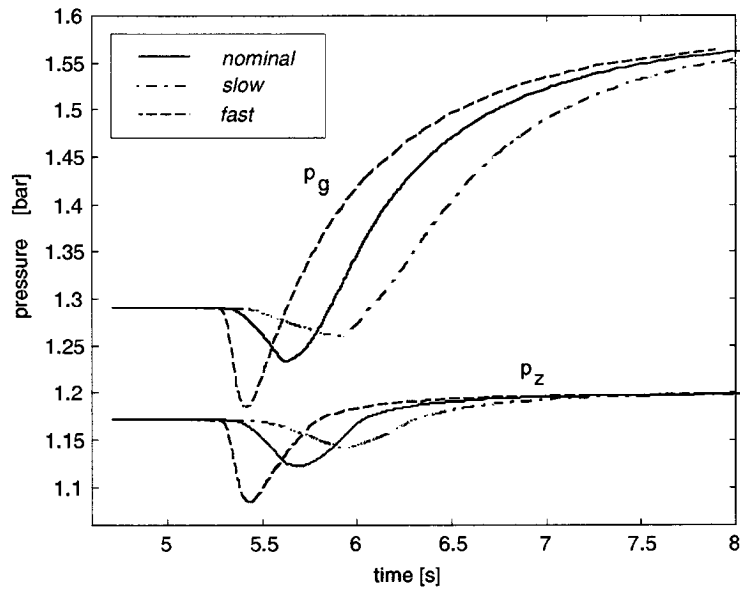
Figure 5.5: Simulated pressure in the gas pocket receiver and simulated scavenging pressure (p_z) for three different GPV closing times
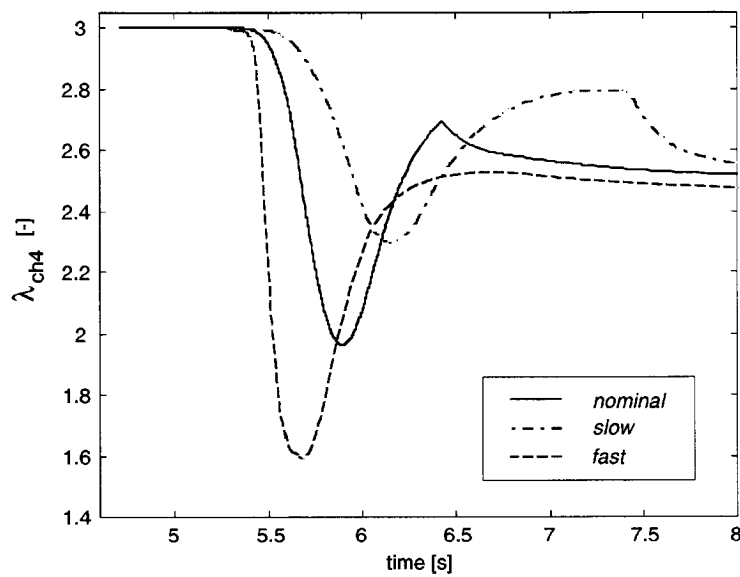
Figure 5.6: Simulated state λ_{ch4} in channel 4 for three different GPV closing times

range must be found by experiment. That is the reason why the model extrapolation does not predict an EGR rate for the simulated value of λ_{ch4}.

When the GPV is closed slowly (case *slow*), the pressures in the gas pocket and in the field z in the wave diagram drop not as deep as in the case *nominal* since the values of the pressure traces follow closer their steady-state values. As a result, the scavenging energy is fairly high also during the closing time, which is indicated by value of λ_{ch4}.

The simulation of the variation of the GPV closing time shows a possibility how the scavenging process during a load step can be influenced. A slower closing velocity leads to an improved scavenging process during the load step.

The benefits of this variant are its effectiveness – already a little change in the minimum closing time leads to a distinctively improved scavenging condition – and the fact that the closing time can be easily adjusted without changing any hardware. The drawback is the slower pressure rise in the high pressure loop PWS–Engine–PWS and therefore the slower torque increase of the SI engine.

5.1.4 Results of Model Extrapolation

In this section two variants of avoiding EGR during a load step were tested by model extrapolation. Since a low gas pocket pressure leads via a low scavenging pressure to a deteriorated or even incomplete scavenging of the cell the target of both variants is to increase the minimum value of the gas pocket pressure during the closing time of the GPV. Basically, this can be achieved by:

1. Enlarging the gas pocket receiver.

2. Limiting the minimum closing time of the gas pocket valve.

The results of the model extrapolation for both variants can be summarized as follows:

- **Variant 1**: The simulation of the first variant shows that the gas pocket receiver volume hardly influences the scavenging process when the GPV is closed as slow as measured. In this case the

dynamics of the GPV position determine the gas pocket pressure dynamics and therefore are predominate. Considering the measured GPV closing time is close to its maximum value, the first variant cannot improve the scavenging process. Moreover, it also has the additional drawback that it requires hardware to be changed.

- **Variant 2**: The simulation of the second variant demonstrates how important the closing time of the GPV on the scavenging process is. Closing the GPV faster than measured, the gas pocket pressure drops lower due to the deficit between in- and outflowing masses in the gas pocket during the first part of the closing time. The scavenging process then is deteriorated. On the contrary, a slower GPV closing velocity can improve the scavenging process since the gas pocket pressure does not drop as deep as in the measured case. Thus, adjusting the GPV closing time to the given system allows to guarantee complete scavenging also during load steps. In addition, this variant shows the benefit that it can be realized by changing only software.

In summary, in order to guarantee complete scavenging of the cell wheel during load steps, the closing time of the GPV has to be adjusted to the dynamics determined by the system "PWS SI engine". If engine torque increase is optimal when a torque demand is satisfied as fast as possible, the optimal value of the GPV closing time is the minimum time at which transient EGR does not occur.

Chapter 6

Conclusions

A simplified pressure wave process of a pressure wave supercharger has been modeled in order to develop a simulation tool which can predict the working behavior of a pressure wave supercharger with gas pocket valve together with a spark ignition (SI) engine in both steady-state and transient operating conditions.

The model of the pressure wave process is based on the relations of the linear one-dimensional gas dynamics. The thermodynamic states as pressures and temperatures in the tubes enclosing the pressure wave supercharger determine the actual pressure wave diagram. Since the dynamics of these thermodynamic states are approximately 100 times slower than the dynamics of building a new pressure wave diagram, the latter dynamics are neglected.

The model of the pressure wave supercharger is validated by the identification of the following physically motivated model parameters:

- compression efficiency

- reflection efficiency

- scavenging pressure

- length of mixing zone

In order to identify the length of the mixing zone, two exhaust gas fraction profiles – one linear profile and one described by exponential functions – were tested. Using the model approach of the linear

125

exhaust gas fraction profile, the identified values of the length of the mixing zone show the smaller standard deviation than the values identified with the exhaust gas fraction profile described by exponential functions. Therefore, the model describes the mixing zone by the linear profile approach. The errors of the outputs of the pressure wave supercharger model are on the order of 5% within the operating range investigated.

The identification of the four model parameters not only validates the pressure wave supercharger model, but also yields the two non-measurable, pressure wave supercharger typical states:

1. The leakage losses out of the cell wheel into the channels on the low pressure side.

2. The length of the mixing zone and its exhaust gas fraction profile.

The leakage losses are the reason for the fact that the scavenging pressure is always lower than the pressure of the exhaust gases on the high pressure side of the pressure wave supercharger. Thus, the leakage losses have to be fairly small in order to ensure complete scavenging of the cell wheel in steady-state conditions. The existence of a mixing zone explains why exhaust gas recirculation can occur together with scavenging air in channel 4. As a result, a value of an air-to-fuel ratio sensor in channel 4 which is in the range between 2.0 ... 1.0 indicates exhaust gas recirculation though the relation between the sensor signal and the exhaust gas recirculation rate depends on the mixing zone length.

In a second step, the validated model of the pressure wave supercharger was coupled to a mean-value model of an SI engine. The resulting engine system model allows to simulate, investigate, and optimize the transient working behavior of the pressure wave supercharged SI engine. For steady-state conditions, the engine system model shows a relative error on the order of 5%, and during transients a relative error smaller than 10%. The error is larger than the one of the pressure wave supercharger model since the errors of all submodels in the engine system model are cumulative. The identified time constants of the pressure wave supercharged SI engine are caused by the fast dynamics of the filling-emptying process of the receivers and by the slow dynamics of the wall temperature of the outlet system.

The engine system model is used in order to explain why the scavenging process must deteriorate or even break down during a load step. While closing the gas pocket valve, the gas pocket pressure drops as a result of a deficit between in- and outflowing masses in the gas pocket receiver. The scavenging pressure p_z as the pressure in the cell wheel just before channel 4 opens shows qualitatively the same undershoot as the gas pocket pressure p_g because it is the pressure "downstream" of the gas pocket. After the exhaust gases from the gas pocket entered the cell wheel, leakage lowers the pressure in the cell until channel 4 opens. As a result, the scavenging pressure is lower than the gas pocket pressure. Hence, already a small gas pocket pressure drop may result in a value of the scavenging pressure that is insufficient for complete scavenging, causing exhaust gas recirculation over the charger.

The absolute value of the gas pocket pressure drop depends on the closing velocity of the gas pocket valve. The faster the gas pocket valve is closed, the more the gas pocket pressure drops:

<div align="center">

increasing gas pocket valve closing velocity

$\Downarrow$

gas pocket pressure drops lower

$\Downarrow$

scavenging is worse

</div>

Furthermore, the model extrapolation demonstrates that the gas pocket pressure drop only slightly depends on the volume of the gas pocket receiver when the gas pocket valve is closed within a realistic closing time. Only for an unrealistically short closing time, the receiver volume of the gas pocket significantly influences the dynamics of the gas pocket pressure. An increased gas pocket volume would thus result in a smaller gas pocket pressure drop and therefore help the scavenging to be complete.

Therefore, in order to avoid transient exhaust gas recirculation, the minimum closing time of the gas pocket valve has to be limited. If an engine system operates optimally when the torque demand is satisfied as fast as possible, then the optimal closing velocity is the fastest velocity at which exhaust gas recirculation does not occur.

In a future step, the developed simulation tool may be used for further investigations and optimizations such as changing the volumes

of the tubes, connecting the tubes in a different way, etc. Besides these system parameter analysis, the tool mainly may be used for model based controller design.

Appendix A

Experimental Set-up

A.1   The Engine SAB360

Data of the engine SAB360:

PWS rotor length	:	l_{rot}	$= 0.064$	[m]
PWS rotor diameter	:	d_{rot}	$= 0.064$	[m]
limitation of				
intake manifold pressure	:	$\max(p_{\mathrm{im}})$	$= 2.10$	[bar]
engine stroke	:	H_{eng}	$= 0.045$	[m]
engine bore	:	D_{eng}	$= 0.065$	[m]
engine compression ratio	:	ϵ	$= 9$	[-]
number of cylinders	:	n_{cyl}	$= 2$	[-]

A.2 Measurement Data for Steady-state Conditions

The following states are known by steady-state measurements. The measurement point for each state is shown in Fig A.1:

measurement point a	:	p_a, T_a
measurement point $th1$	:	pos_{th1}
measurement point 1	:	p_1, T_1
measurement point $1s$	:	T_{1s}
measurement point $emot$	:	n_{pws}, P_{emot}
measurement point 2	:	p_2, T_2, c_{CO2}
measurement point $th2$	:	pos_{th2}
measurement point im	:	p_{im}, T_{im}
measurement point eng	:	n_{eng}, T_{eng}, $\dot{m}_{fuel}$
measurement point em	:	p_{em}, T_{em}, λ_v
measurement point 3	:	p_3, T_3
measurement point gpv	:	pos_{GPV}
measurement point g	:	p_g, T_g
measurement point 4	:	p_4, λ_{ch4}, T_{4-1}, T_{4-2}, T_{4-3}, T_{4-4}
measurement point oc	:	$T_{after-ocat}$

From these measurement data, the following variables can be derived:

- mass flow of fresh compressed air:

$$\dot{m}_{ch2-a} = \dot{m}_{fuel} \frac{\lambda_v}{k_{stoich}} \qquad (A.1)$$

- mass flow of recirculated exhaust gases:

$$\dot{m}_{egr} = \dot{m}_{ch2-a} \left(\frac{c_{CO2}/Max(c_{CO2})}{1 - c_{CO2}/Max(c_{CO2})} \right) \qquad (A.2)$$

- mass flow of scavenging air in channel 4:

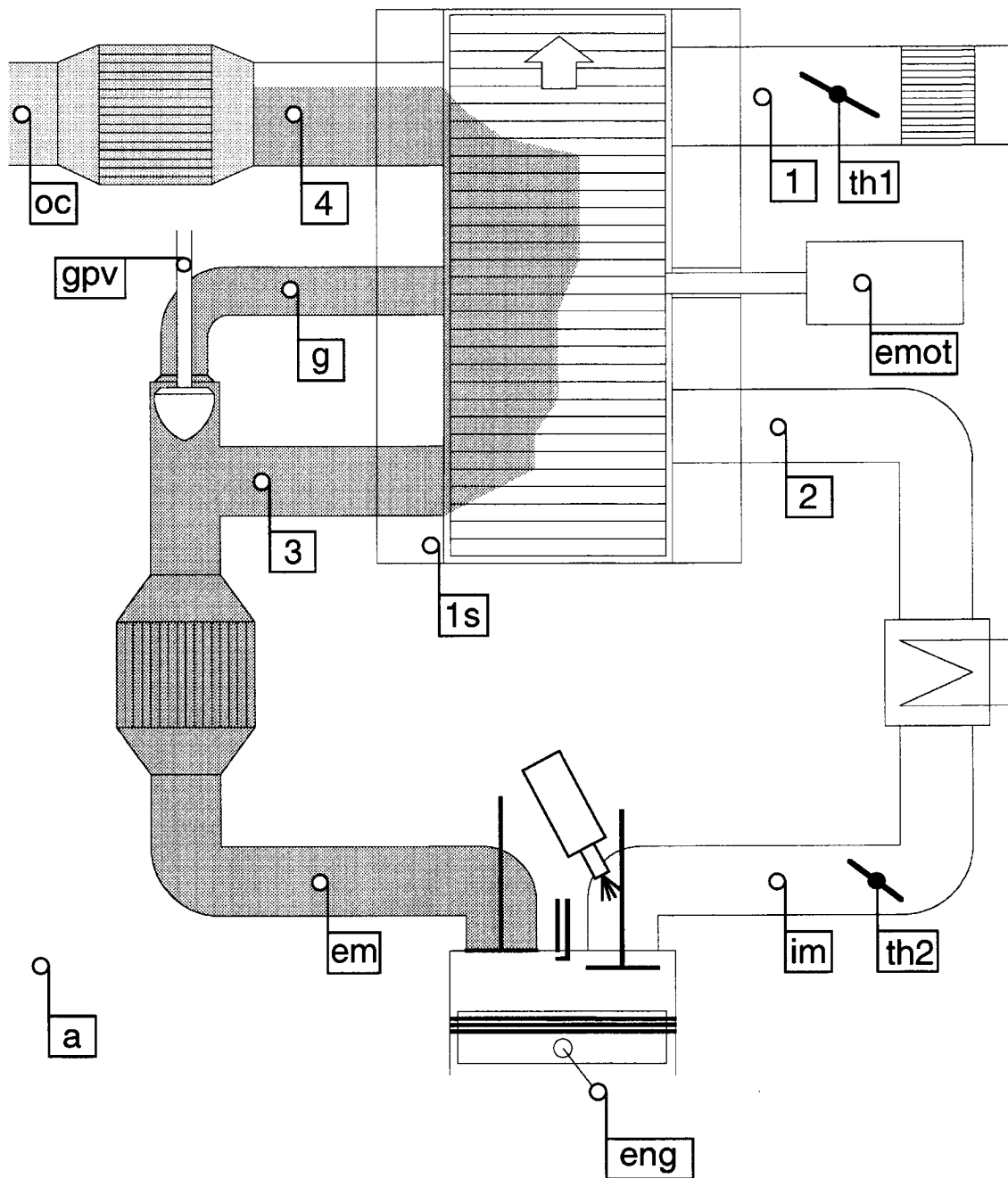$$\dot{m}_{ch4-a} = \dot{m}_{fuel} \left(\frac{\lambda_{ch4} - \lambda_v}{k_{stoich}} \right) \qquad (A.3)$$

Figure A.1: Instrumentation of the engine SAB360

- mass flow in channel 1, 2, 3, 4:

$$\dot{m}_{ch1} = \dot{m}_{ch2-a} + \dot{m}_{ch4-a} \tag{A.4}$$

$$\dot{m}_{ch2} = \dot{m}_{ch2-a} + \dot{m}_{egr} \tag{A.5}$$

$$(\dot{m}_{ch3} + \dot{m}_{chg}) = \dot{m}_{ch2} + \dot{m}_{fuel} \tag{A.6}$$

$$\dot{m}_{ch4} = (\dot{m}_{ch3} + \dot{m}_{chg}) - \dot{m}_{egr} + \dot{m}_{ch4-a} \tag{A.7}$$

- mean temperature in channel 4:

$$T_{ch4-mx} = \frac{T_{4-1} + T_{4-2} + T_{4-3} + T_{4-4}}{4} \tag{A.8}$$

- exhaust gas recirculation rate:

$$x_{egr} := \dot{m}_{egr}/\dot{m}_{ch2} \tag{A.9}$$

A.3   Measurement Data During Transients

The following states are measured during transients:

pressures	:	p_2, p_{im}, p_3, p_g
torque	:	T_{eng}
rotational speeds	:	n_{eng}, n_{pws}
air-to-fuel ratio	:	λ_{ch4}
valve positions	:	pos_{th1}, pos_{th2}, pos_{GPV}

Appendix B

Additional Simulation Results

B.1   Calculated Pressure Wave Diagram

This section shows a calculated pressure wave diagram at part-load condition, where the GPV is 60% closed. The diagram is calculated at the "euler radius":

$$r_{\text{euler}} := \sqrt{(r_{\text{i}}^2 + r_{\text{o}}^2)/2}$$

The thermodynamic boundary condition for this pressure wave diagram are:

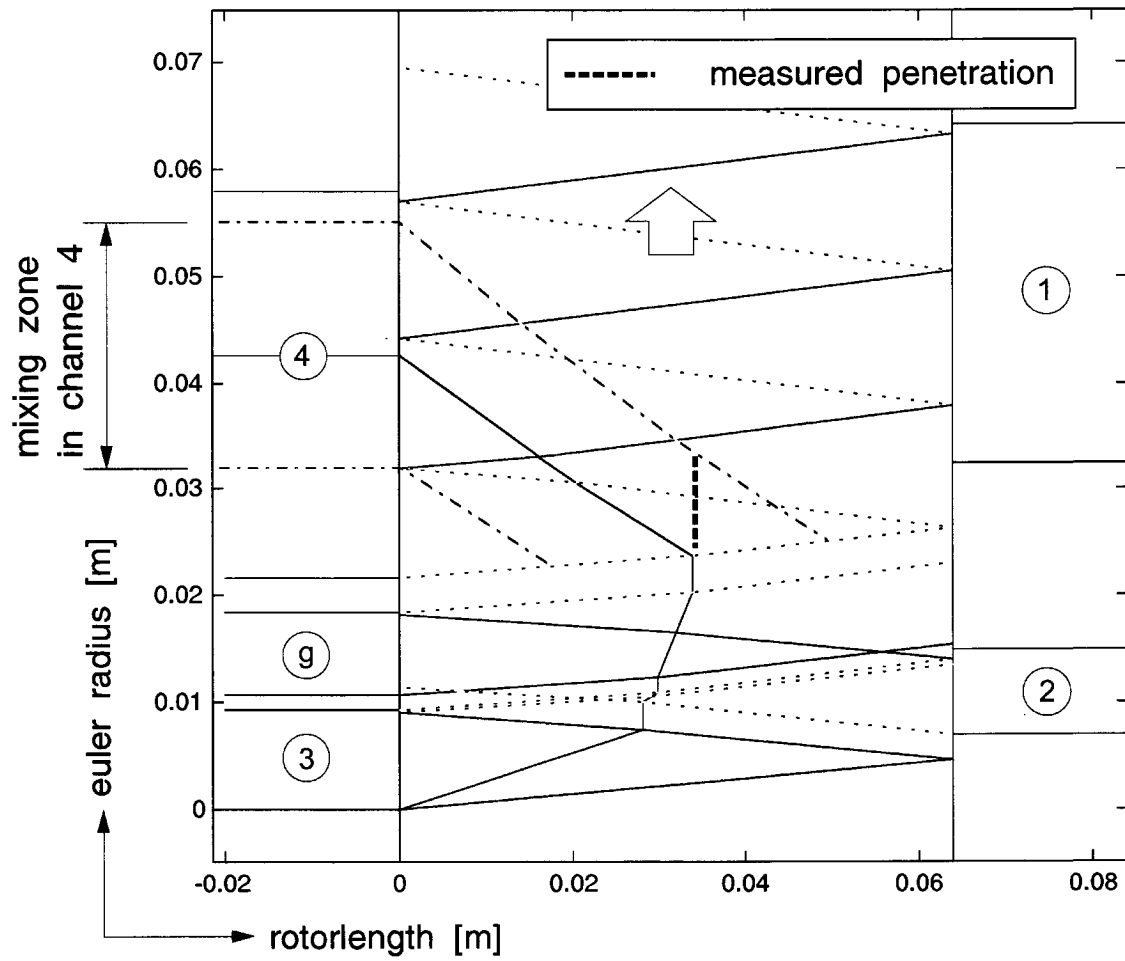|			
p_3	=	1.523	[bar]
T_3	=	738	[C]
p_2	=	1.583	[bar]
p_1	=	0.956	[bar]
T_1	=	23.3	[C]
p_4	=	0.978	[bar]
n_{pws}	=	13050	[rpm]

Figure B.1: Calculated pressure wave diagram for GPV = 60% closed

B.2 Identified GPV Throttle Coefficient

Due to the complex geometry of the gas pocket valve the fluid has to turn approximately 90 degrees in order to flow around the valve body. This fact might explain the fairly deep identified throttle coefficient of the GPV.
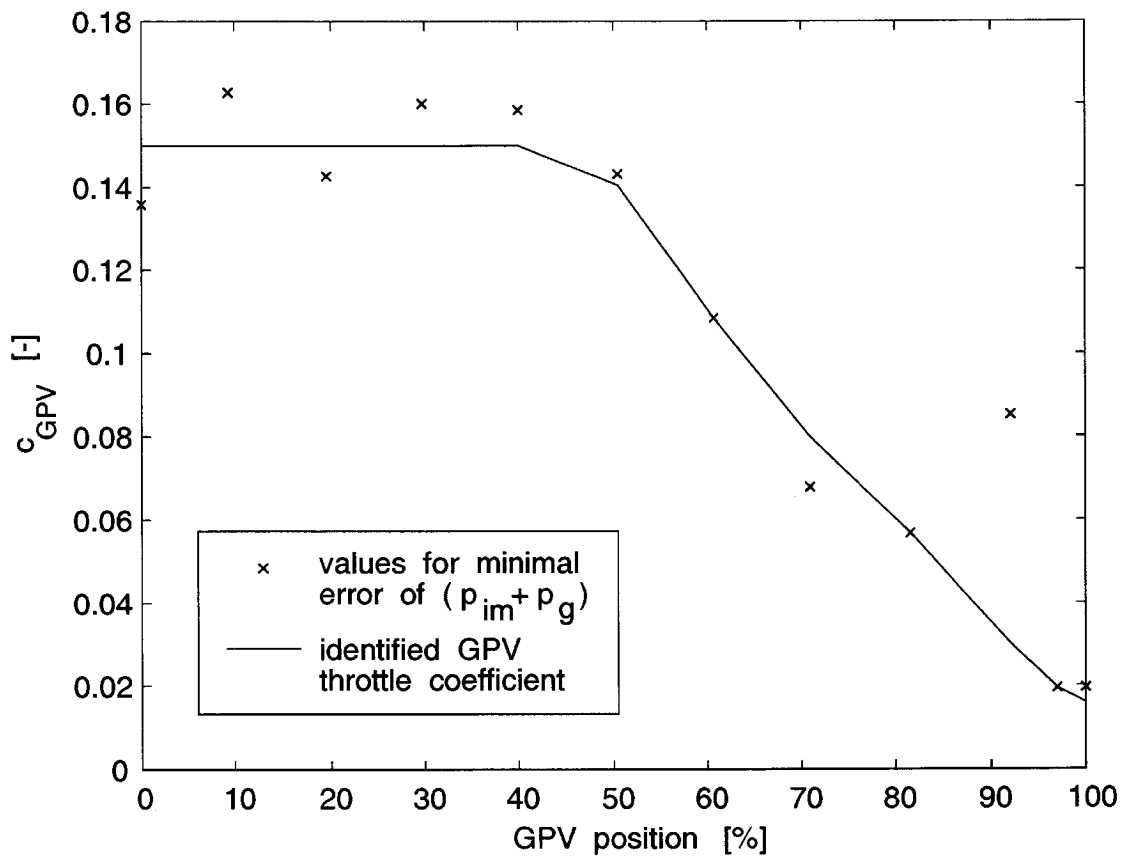

Figure B.2: Identified throttle coefficient of the GPV

Seite Leer /
Blank leaf

Bibliography

A. Amstutz. *Geregelte Abgasrückführung zur Senkung der Stickoxid-und Partikelemissionen beim Dieselmotor mit Comprex-Aufladung.* Diss. ETH, No. 9421, ETH Zürich, 1991.

H. D. Baehr. *Thermodynamik.* 8. Auflage, Springer Verlag, 1992.

D. M. Baker and D. N. Assanis. A Coupled Methodology for Modeling the Transient Thermal Response of SI Engines subject to Time-Varying Operating Conditions. Number 971859 in SAE Technical Paper, pages 733–748, 1997.

M. Berchtold. Druckwellenaufladung für kleine Fahrzeug-Dieselmotoren. *Schweizerische Bauzeitung 79, No. 46, pp. 801-808,* 1961.

K. Boulouchos. *Strömung, Gemischbildung und Verbrennung, Vorlesungsscript.* Institut für Energietechnik, Laboratorium für Verbrennungsmotoren und Verbrennungstechnik, 1994.

E. Cortona. *Engine Thermomanagement for Fuel Consumption Reduction.* Diss. ETH, No. 13862, ETH Zürich, Switzerland, 2000.

N. Croes. Die Wirkungsweise der Taschen des Druckwellenladers Comprex. *MTZ Motortechnische Zeitschrift, Vol. 40, No. 2, pp. 91-97,* 1979.

M. K. Eberle and H. U. Hörler. Das Ökomobil - eine mögliche Autozukunft. *Neue Zürcher Zeitung, 3.März 1988, S.99-100,* 1988.

H. Endres. *Comprex - Aufladung schnellaufender direkteinspritzender Dieselmotoren.* Diss. 1985, Aachen, Deutschland, 1985.

L. Guzzella. *Systemtechnik am Verbrennungsmotor, Vorlesungsscript.* Institut für Energietechnik, Laboratorium für Verbrennungsmotoren und Verbrennungstechnik, 1995.

L. Guzzella and R. Martin. Das SAVE-Motorkonzept. *MTZ Motortechnische Zeitschrift 59 (1998) 10*, 1998.

G. Gyarmathy. How does the COMPREX Pressure-Wave Supercharger Work? *SAE Technical Paper, 830234*, 1983.

J. Gygax and G. Schneider. Betriebserfahrungen mit dem Druckwellenlader Comprex im Opel Senator. *MTZ Motortechnische Zeitschrift 49 (1988) 9*, 1988.

E. Hendricks. Isothermal Vs. Adiabatic Mean Value SI Engine Models. 3rd *IFAC Workshop, Karlsruhe, Germany, March 28-30, 2001*, 2001.

J. B. Heywood. *Internal Combustion Engine Fundamentals.* Automotive Technology Series. McGraw-Hill International Editions, I. Title, II. Series, 1988.

H. U. Hörler. *Abschätzung der Verluste in Instationär-Gasdynamischen Kanal-Trommel-Drucktauschern.* Diss. ETH, No. 4402, ETH Zürich, Switzerland, 1969.

J. Inhelder. *Verbrauchs- und schadstoffoptimiertes Ottomotor-Aufladekonzept.* Diss. ETH, No. 11948, ETH Zürich, Switzerland, 1996.

E. Jenny. *Berechnungen und Modellversuche über Druckwellen grosser Amplituden in Auspuff-Leitungen.* Diss. ETH, No. 1793, ETH Zürich, Switzerland, 1949.

E. Jenny. Beschleunigungsverhalten von Diesel- und Otto-PKW-Motoren mit Turboladern fixer und variabler Geometrie, mechanischen Ladern und Comprex. *VDI Berichte, p.255-274*, 1991.

T. A. Kollbrunner. Comprex Supercharging for Passenger Diesel Car Engines. *1980 Society of Automotive Engineers, 800884*, 1980.

Z. Liu, A. L. Hoffmanner, J. F. Skowron, and M. J. Miller. Exhaust Transient Temperature Response. Number 950617 in SAE Technical Paper, pages 1–9, 1995.

K. Lösing and R. Lutz. Einhaltung zukünftiger Emissionsvorschriften durch gekühlte Abgasrückführung. *MTZ Motortechnische Zeitschrift 60 (1999) 7/8*, 1999.

E. Mattarelli and A. Valentini. On the Flow Modeling through the Valve Assembly in Engine Cycle Simulations. *SAE Technical Paper, 2000-01-0570*, 2000.

A. Mayer. Comprex-Supercharging eliminates Trade-off of Performance, Fuel Economy and Emissions. *SAE Technical Paper Series 881152, August 8-11*, 1988.

A. Mayer, I. El. Nashar, and J. Perewusnyk. Comprex with Gas Pocket Control. *Institution of Mechanical Engineers (Great Britain), C405/032*, 1990.

S. Meisner and S. C. Sorenson. Computer Simulation of Intake and Exhaust Manifold Flow and Heat Transfer. Number 860242 in SAE Technical Paper, pages 1–12, 1986.

E. Pauli and A. Amstutz. Regelstrategie des COMPREX-aufgeladenen Dieselmotors zur Emissionsminderung. *Sonderdruck MTZ, Motortechnische Zeitschrift, Juni, 1989), C405/032*, 1989.

R. Pfiffner. *Optimal Operation of CVT-Based Powertrains*. Diss. ETH, No. 14136, ETH Zürich, Switzerland, 2001.

R. Pfiffner, F. Weber, A. Amstutz, and L. Guzzella. Modeling and Modelbased Control of Supercharged SI-engines with Minimal Fuel Consumption. *Proc. 16th American Control Conference - ACC, Albuquerque, NM*, 1997.

C. Pianese and G. Rizzo. A Dynamic Model for Control Strategy Optimization in Spark Ignition Engines. *The American Society of Mechanical Engineers*, 1992.

J. Piechna. Numerical Simulation of the Comprex Type of Supercharger: Comparison of Two Models of Boundary Conditions. *The*

Archive of Mechanical Engineering, Vol. XLV, No. 3, pp. 233-250, 1998a.

J. Piechna. Numerical Simulation of the Pressure Wave Supercharger - Effect of Pockets on the Comprex Supercharger Characteristics. *The Archive of Mechanical Engineering, Vol. XLV, No. 4, pp. 305-323,* 1998b.

J. Piechna. A Two Dimensional Model of the Pressure Wave Supercharger. *The Archive of Mechanical Engineering, Vol. XLVI, No. 4, pp. 331-348,* 1999.

J. Piechna and P. Lisewski. Numerical Analysis of Unsteady Two-Dimensional Flow Effects in the Comprex Supercharger. *The Archive of Mechanical Engineering, Vol. XLV, No. 4, pp. 341-351,* 1998.

R. Pivec, T. Sams, and A. Wimmer. Wärmeübergang im Ein- und Auslasssystem. *MTZ Motortechnische Zeitschrift 59 (1998) 10,* 1998.

R. Sauer. *Einführung in die theoretische Gasdynamik.* Technische Hochschule München, dritte verbesserte Auflage, Springer-Verlag, Berlin/Göttingen/Heidelberg, 1960.

W. Selerowicz and J. Piechna. Comprex Type Supercharger as a Pressure-Wave Transformer Flow Characteristics. *The Archive of Mechanical Engineering, Vol. XLVI, No. 1, pp. 57-77,* 1999.

P. J. Shayler, D. J. Hayden, and T. Ma. Exhaust System Heat Transfer and Catalytic Converter Performance. volume SP-1455 of *SAE Technical Paper,* pages pp. 1-15, 1999.

P. Soltic. *Part-Load Optimized SI Engine Systems.* Diss. ETH, No. 13942, ETH Zürich, Switzerland, 2000.

F. W. Spinnler and F. A. Jaussi. The fully self-regulated pressure wave supercharger Comprex for passenger car diesel engines. *IMechE 1986, C124, p.171-178,* 1986.

W. Traupel. *Thermische Turbomaschinen, thermodynamische-strömungstechnische Berechnungen, Band 1.* Springer-Verlag, Berlin, Heidelberg, 1988.

F. J. Wallace and C. A. Aldis. Comprex supercharging versus turbocharging of large truck diesel engine.

F. Weber and L. Guzzella. Control Oriented Modeling of a Pressure Wave Supercharger. *SAE Technical Paper, 2000-01-0567*, 2000.

T. S. Wisniewski. Experimental Study of Heat Transfer on Exhaust Valves of 4c90 Diesel Engine. In *SAE Internation Congress and Exposition*, number 981040 in SAE Technical Paper, pages 1–7, March 1998.

G. Zehnder. Berechnungsaufgaben bei der Entwicklung des Comprex. *Schweizerische Bauzeitung, 88. Jahrgang, Heft 30, 23. Juli*, 1970.

G. Zehnder. Berechnung von Druckwellen in der Aufladetechnik. *Brown Boveri Mitteilung, 4/5*, 1971.

Y. Zhang, K. Phaneuf, R. Hansson, and N. Showalter. Computer Modeling on Exhaust System Heat Transfer. Number 920262 in SAE Technical Paper, pages 1–9, 1992.

J. Zierep. Vorlesung über theoretische Gasdynamik. *Technische Hochschule Karlsruhe, Verlag G. Braun*, 1963.

Seite Leer /
Blank leaf

Curriculum Vitae

Personal Data

Name: Felix Weber
Date of birth: 13. January 1970

Education

1977–1983	Primary school in Pfaffhausen ZH, Switzerland
1983–1989	Gymnasium in Zürich ZH, Switzerland
1989	Matura certificate, type B
1990	Military service
1990–1992	Studies in mechanical engineering, part I, Swiss Federal Institute of Technology (ETH) Zürich, Switzerland
1992–1993	Three month of practice in industry
1993	Military service
1993–1996	Studies in mechanical engineering, part II, Swiss Federal Institute of Technology (ETH) Zürich, Switzerland
	Major in thermodynamics of internal combustion engines
1996	Diploma as *Dipl. Masch.-Ing. ETH*
1996–2001	Doctoral student and research assistant at the Institute for Energy Technology, Swiss Federal Institute of Technology (ETH) Zürich, Switzerland; three months of language study in Cheltenham (GB), Certificate in Advanced English